

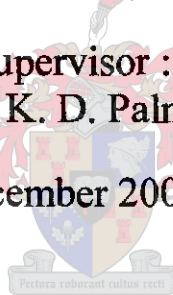
# *An Active Receiving Antenna for Borehole Pulsed Radar Applications*

M. D. van Wyk

( Thesis presented in partial fulfilment of the requirements for the degree of Master of  
Engineering at the University of Stellenbosch )

Supervisor :  
Prof. K. D. Palmer

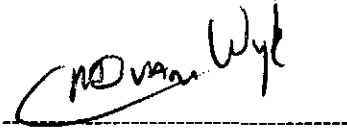
December 2002



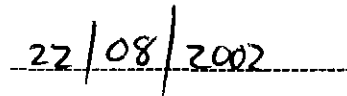
UNIVERSITEIT • STELLENBOSCH • UNIVERSITY  
jou kennisvenoot • your knowledge partner

## *Declaration*

I, the undersigned, hereby declare that this thesis and the work contained therein is my own original work, except where indicated.



M. D. van Wyk



Date

## *Abstract*

An efficient radiating structure was needed for borehole pulsed radar applications in the 10-100 MHz frequency band. Both resistively loaded and insulated wire antennas were investigated and an active antenna is proposed as a final solution.

The study proceeded from the characterization of the origin of radiation on a conductive dipole wire antenna when excited with a transient. Different radiation mechanisms were identified when the antenna was excited with a current or voltage source.

The wire antenna in insulated surroundings was modelled using transmission line theory to simulate the antenna in the borehole environment. The transmission line model proved to be useful for investigating conducting and resistively loaded antennas for the dimensions associated with borehole surveys.

From the modelling results, it became apparent that the asymmetric resistively loaded antenna might provide the best practical solution. This antenna displays reasonably stable input impedance and low far-field variations for different theta angles across the desired frequency band. Different percentage Wu-King resistive profiles were studied to show that a 50% reduction in the normal Wu-King resistor values will add only a little ringing but have better amplitude response than the 100% Wu-King loading.

The asymmetric resistively loaded antenna has better sensitivity to receiving transients when combined with a high impedance source load than when symmetrically loading the antenna. An active antenna incorporating the asymmetric resistively loaded antenna and a low noise current feedback front end amplifier was built and measured in an air environment. The results show that the active antenna has a flat transfer function and reacts as a wide band electric field probe with better resolution than in the conventional 50  $\Omega$  loaded case.

## *Opsomming*

'n Effektiewe stralingsstruktuur was benodig vir puls radar toepassings in die 10-100 MHz frekwensieband. 'n Aktiewe antenna is as oplossing voorgestel nadat beide weerstand-belaste en ge-insuleerde draadantennas ondersoek is.

Die studie is opgevolg deur die karakterisering van straling op 'n geleidende dipool antenna terwyl die antenna korstondig opgewek is. Verskeie stralingsmeganismes is geïdentifiseer wanneer die antenna deur 'n spannings- of stroombron opgewek is.

Die draadantenna is deur gewone transmissielysteorie in 'n ge-insuleerde omgewing gemodelleer, om die boorgat omgewing te simuleer. Die transmissielynmodel is bewys om 'n bruikbare model vir geleidende en weerstandbelaste antennes, vir die dimensies geassosieer met boorgatondersoek te wees.

Vanaf die gemodelleerde resultate het dit duidelik geword dat die asimmetriese weerstand-belaste antenna dalk die mees praktiese oplossing lewer. Die antenna het 'n redelike stabiele intree-impedansie met min ver veld variasies vir verskeie theta hoeke oor die verlangde frekwensieband vertoon. Verskillende persentasie Wu-King weerstandprofile was bestudeer met die gevolg dat 'n 50% vermindering in die Wu-King weerstandwaardes min lui en beter amplitude reaksie tot die antenna byvoeg as die 100% Wu-King profiel.

Die asimmetriese weerstand-belaste antenna beskik oor beter sensitiwiteit vir die ontvang van korstondige seine, wanneer dit met 'n hoë bron impedansie gekombineer word, bo die simmetriese weerstand belasting. 'n Aktiewe antenna met 'n asimmetriese weerstandbelaste antenna en lae-ruis stroom-terugvoer versterker is gebou en in 'n lugomgewing gemeet. Die resultate het gewys dat die aktiewe antenna 'n plat oordrag vertoon en reageer soos 'n wye-band elektriese veld sondeerder met beter resolusie as 'n konvensionele 50  $\Omega$  belading.

## *Acknowledgements*

First and foremost I thank God for his presence and guiding hand throughout my life and the opportunity of fulfilling my goals.

Secondly, thanks go out to my family and friends for their patience and support.

I am forever in debt to Prof. Palmer as the father figure who shaped me into becoming a competitive engineer, and who allowed me the opportunity to explore his knowledge and wisdom.

Special thanks to the team at SED (Wessel Croukamp, Ulrich Büttner, Asley Cupido) for their innovative solutions and quick responses.

I will never forget the friends in the radar group, especially Max Birch (Inter Max) and Paul Herselman (Bobbejaan). I also thank Paul for his assistance and input in realising the borehole radar measurements and Max for his computer skills.

I would also like to thank Defencetek of the CSIR for their financial support.

## *Table of Contents*

<b>Declaration.....</b>	<b>i</b>
<b>Abstract.....</b>	<b>ii</b>
<b>Opsomming.....</b>	<b>iii</b>
<b>Acknowledgements .....</b>	<b>iv</b>
<b>Table of Contents .....</b>	<b>v</b>
<b>List of Figures.....</b>	<b>ix</b>
<b>List of Tables .....</b>	<b>xviii</b>
<b>CHAPTER 1 : Introduction.....</b>	<b>1</b>
<b>1.1 Background .....</b>	<b>1</b>
<b>1.2 Current borehole radar system.....</b>	<b>2</b>
1.2.1 Transmitter .....	2
1.2.2 Receiver.....	3
1.2.3 Optical link.....	4
1.2.4 Data acquisition system.....	4
<b>1.3 Thesis outline .....</b>	<b>4</b>
<b>CHAPTER 2 : Verification of Electromagnetic Simulation Tools .....</b>	<b>6</b>
<b>2.1 Introduction .....</b>	<b>6</b>
<b>2.2 Experimental verification .....</b>	<b>7</b>
2.2.1 Conductive monopole.....	7
2.2.2 Resistive loaded monopole.....	9
2.2.3 Insulated monopole .....	11
<b>2.3 Conclusion .....</b>	<b>18</b>
<b>CHAPTER 3 : Investigating Time-Domain Radiation for Wire</b>	
<b>Antennas .....</b>	<b>20</b>
<b>3.1 Introduction .....</b>	<b>20</b>
<b>3.2 Investigating dipole radiation using travelling wave elements.....</b>	<b>20</b>

3.2.1	The basic travelling wave element .....	21
3.2.2	Constructing a dipole antenna using travelling wave elements.....	27
3.2.3	Comparing radiation results between a dipole constructed of travelling wave elements and a full FD-TD solution .....	29
<b>3.3</b>	<b>Charge behaviour on a dipole radiator .....</b>	<b>36</b>
3.3.1	Examination of electromagnetic radiation.....	37
3.3.2	Extracting time-dependent charge behaviour on a dipole antenna .....	38
<b>3.4</b>	<b>Conclusion .....</b>	<b>41</b>
<b>CHAPTER 4 : Theoretical and Numerical Modelling of Insulated Antennas .....</b>		<b>42</b>
<b>4.1</b>	<b>Introduction .....</b>	<b>42</b>
<b>4.2</b>	<b>King and Smith transmission line model ( <i>TLM</i> ).....</b>	<b>42</b>
<b>4.3</b>	<b>Application of the complete <i>TLM</i> on insulated antennas.....</b>	<b>50</b>
4.3.1	Asymmetric dipole .....	50
4.3.2	Symmetric dipole.....	53
<b>4.4</b>	<b>Comparison between FEKO ( MoM ) and <i>TLM</i>.....</b>	<b>54</b>
4.4.1	Insulated conducting dipole antenna .....	54
4.4.2	Insulated Wu-King antenna .....	55
<b>4.5</b>	<b>Comparing the insulated antenna with a bare antenna equivalent in a dielectric medium.....</b>	<b>56</b>
<b>4.6</b>	<b>Conclusion .....</b>	<b>58</b>
<b>CHAPTER 5 : Modelling of Radar Probes .....</b>		<b>59</b>
<b>5.1</b>	<b>Introduction .....</b>	<b>59</b>
<b>5.2</b>	<b>Conducting dipole.....</b>	<b>60</b>
5.2.1	Conducting dipole in air .....	60
5.2.2	Insulated dipole in a mine environment .....	61
5.2.3	Pulse transmitting characteristics of conducting dipole .....	65
5.2.4	Pulse receiving characteristics of conducting dipole.....	68
<b>5.3</b>	<b>Resistively loaded dipole antenna .....</b>	<b>70</b>
5.3.1	Resistively loaded dipole in air .....	70
5.3.2	Insulated resistively loaded dipole in mine environment .....	71
5.3.3	Pulse transmitting characteristics of resistive dipole.....	73
5.3.4	Pulse receiving characteristics of resistive dipole .....	76
<b>5.4</b>	<b>Asymmetric dipole antenna .....</b>	<b>78</b>
5.4.1	Asymmetric resistively loaded dipole in air .....	78

5.4.2	Insulated asymmetric dipole in a mine environment.....	79
5.4.3	Pulse transmitting characteristics of asymmetric dipole .....	81
5.4.4	Pulse receiving characteristics of asymmetric dipole.....	82
<b>5.5</b>	<b>Coupling between aligned transmitter and receiver .....</b>	<b>84</b>
<b>5.6</b>	<b>Conclusion .....</b>	<b>86</b>
<b>CHAPTER 6 : Active Receiving Antenna .....</b>		<b>87</b>
<b>6.1</b>	<b>Introduction .....</b>	<b>87</b>
<b>6.2</b>	<b>Active receiver .....</b>	<b>87</b>
6.2.1	Optic modulator.....	88
6.2.2	Optic demodulator.....	90
6.2.3	Optical link.....	90
6.2.4	Active pulse receiver .....	96
<b>6.3</b>	<b>Pulse transmitter .....</b>	<b>105</b>
<b>6.4</b>	<b>Measurements.....</b>	<b>106</b>
6.4.1	Measurement and test construction .....	106
6.4.2	Measurement results.....	108
<b>6.5</b>	<b>Conclusion.....</b>	<b>111</b>
<b>CHAPTER 7 : Conclusions.....</b>		<b>113</b>
<b>7.1</b>	<b>Conclusions .....</b>	<b>113</b>
7.1.1	Verification of simulation tools.....	113
7.1.2	Investigating time-domain radiation for wire antennas .....	113
7.1.3	Theoretical and numerical modelling of insulated antennas .....	114
7.1.4	Modelling of radar probes .....	114
7.1.5	Active receiving antenna .....	115
<b>7.2</b>	<b>Future work .....</b>	<b>115</b>
<b>CHAPTER 8 : References.....</b>		<b>117</b>
<b>Appendix A1 : The theoretical derivation of the Wu-King Profile .119</b>		
<b>Appendix A2 : Theory of an RC circuit for measurement of a dielectric specimen.....</b>		<b>122</b>
<b>Appendix A3 : Theory of resonating RLC circuit for measurement of a dielectric specimen.....</b>		<b>124</b>

<b>Appendix B1 : Charge per unit length on the basic travelling-wave element .....</b>	<b>127</b>
<b>Appendix B2 : Electromagnetic field of the basic travelling-wave element .....</b>	<b>128</b>
<b>Appendix B3 : The Discrete Fourier Transform for aperiodic finite-energy sequences .....</b>	<b>131</b>
<b>Appendix C1 : Derivation of the input impedance of a variable two section insulated dipole antenna.....</b>	<b>132</b>
<b>Appendix C2 : Extracting the input impedance of a symmetric insulated dipole antenna using ABCD parameters .....</b>	<b>134</b>
<b>Appendix D1 : Pulse receiving characteristic for different percentage Wu-King loadings .....</b>	<b>136</b>
<b>Appendix D2 : Input impedance of asymmetrical resistive dipole for different ambient properties .....</b>	<b>137</b>
<b>Appendix D3 : Pulse receiving characteristic for different percentage Wu-King loadings on the asymmetrical dipole.....</b>	<b>138</b>

## *List of Figures*

Figure 1.1 : Deployment of borehole radar in a incline borehole [1] .....	1
Figure 1.2 : Transmitter dimension and electronic operation block diagram .....	2
Figure 1.3 : Receiver dimension and electronic operation block diagram .....	3
Figure 2.1 : Physical dimension of conducting monopole. ....	8
Figure 2.2 : Magnitude (reflection coefficient) of conducting monopole of Figure 2.1.....	8
Figure 2.3 : Phase (reflection coefficient) of conducting monopole of Figure 2.1.....	8
Figure 2.4 : Input impedance of conducting monopole of Figure 2.1. ....	8
Figure 2.5 : Physical dimension of resistive monopole.....	10
Figure 2.6 : Magnitude (reflection coefficient) of resistive monopole of Figure 2.5. ....	10
Figure 2.7 : Phase (reflection coefficient) of resistive monopole of Figure 2.5. ....	10
Figure 2.8 : Input impedance of resistive monopole of Figure 2.5.....	10
Figure 2.9 : Polyurethane sample and Marconi test jig. ....	12
Figure 2.10 : Measuring setup and equivalent electric representation of the test jig and sample .....	13
Figure 2.11 : (a) Equivalent electric circuit of jig when the clamps are shorted, (b) and when open. ....	13
Figure 2.12 : Dielectric constant of polyurethane. ....	14
Figure 2.13 : Loss tangent of polyurethane. ....	14
Figure 2.14 : Physical dimension of insulated monopole. ....	16
Figure 2.15 : Magnitude (reflection coefficient) of insulated monopole of Figure 2.14. ....	16
Figure 2.16 : Phase (reflection coefficient) of insulated monopole of Figure 2.14.....	16
Figure 2.17 : Input impedance of insulated monopole of Figure 2.14. ....	16
Figure 2.18 : (a) Dielectric coating, (b) Centre dipole with dielectric coating and dielectric cylinder, (c) Off-centre dipole with dielectric coating and dielectric cylinder.....	17
Figure 2.19 : Magnitude (reflection coefficient) of insulated dipole with different formulation. .....	17
Figure 2.20 : Phase (reflection coefficient) of insulated dipole with different formulations. .	17
Figure 2.21 : Input impedance of insulated dipole with different formulations. ....	17
Figure 2.22 : Schematic of off-centre dipole in two dielectric cylinders. ....	18
Figure 2.23 : Magnitude (reflection coefficient) of insulated dipole with double dielectric cylinders. ....	18
Figure 2.24 : Input impedance of insulated dipole with double dielectric cylinders.....	18

Figure 2.25 : Phase (reflection coefficient) of insulated dipole with double dielectric cylinders. ....	18
Figure 3.1 : Geometry and coordinate system of basic travelling wave element [11]. ....	21
Figure 3.2 : Time trace of narrow and broad Gaussian input pulse as a function of distance in air.....	22
Figure 3.3 : (a)-(c) Magnitude of the electric field surrounding a single travelling wave element at three time “snapshots” , $t/\tau_a = 0.5$ ; $t/\tau_a = 1.5$ and $t/\tau_a = 2.5$ . (d) Time harmonic representation of the electric field surrounding a single travelling wave element where $\lambda = 0.5$ .....	23
Figure 3.4 : (a)-(d) Magnitude of the electric field surrounding a single travelling wave element at three time “snapshots” , $t/\tau_a = 0.5$ ; $t/\tau_a = 1.5$ , $t/\tau_a = 2.5$ and $t/\tau_a = 5$ . (d) Time harmonic representation of the electric field surrounding a single travelling wave element where $\lambda = 3\text{m}$ .....	24
Figure 3.5 : (a) Far-zone electric field of the travelling wave element excited by an electrically small pulse. (b) and (c) describe the time difference between the source and termination wave fronts at various positions in space [11]. ....	26
Figure 3.6 : (a) Standing wave dipole. (b) represented by four travelling wave elements .....	27
Figure 3.7 : (a)-(c) Magnitude of the electric field surrounding a standing wave dipole antenna at three time “snapshots” , $t/\tau_a = 0.5$ ; $t/\tau_a = 1.5$ and $t/\tau_a = 2.5$ . (d) Time harmonic representation of the electric field where $\lambda = 0.5\text{m}$ . ....	28
Figure 3.8 : Schematic of the geometrical setup of the dipole with electric field probe. ....	29
Figure 3.9 : Real Gaussian input signal of current source. ....	29
Figure 3.10 : Voltage at input terminal for a source impedance of $1\Omega$ . ....	30
Figure 3.11 : Current at input terminal for a source impedance of $1\Omega$ . ....	30
Figure 3.12 : Voltage at input for a source impedance of $10\text{k}\Omega$ . ....	30
Figure 3.13 : Current at input for a source impedance of $10\text{k}\Omega$ . ....	30
Figure 3.14 : Time trace of the electric field for FD-TD and travelling element dipole when excited by an current source. ....	31
Figure 3.15 : Time trace of the electric field for FDTD and travelling element dipole when excited by an voltage source.....	32
Figure 3.16 : Gaussian input voltage with different frequency contents for $R_s = 1\Omega$ .....	33
Figure 3.17 : Gaussian input current with different frequency contents for $R_s = 10\text{k}\Omega$ . ....	33
Figure 3.18 : Electric field for different Gaussian pulse widths - voltage source. ....	34
Figure 3.19 : Magnitude of electric field of different Gaussian pulse widths - a voltage source. ....	34
Figure 3.20 : Electric field for different Gaussian pulse widths - current source.....	35

Figure 3.21 : Magnitude of electric field of different Gaussian pulse widths - current source. .....	35
Figure 3.22 : Electric field (Theta component) at various angles for a Gaussian pulse with a frequency content of 0-150 MHz. ....	35
Figure 3.23 : Magnitude of the coupling of the electric field (Theta component) at various angles for a Gaussian pulse with a frequency content of 0-150 MHz. ....	35
Figure 3.24 : Discrete dipole used for extracting charge density. ....	38
Figure 3.25 : Normalized charge density of dipole antenna in air.....	39
Figure 3.26 : Top view of charge spread as a function of time and distance of dipole in air..	39
Figure 3.27 : Normalized charge density of dipole antenna in a borehole. ....	40
Figure 3.28 : Top view of charge spread as a function of time and distance of dipole in a borehole. ....	40
Figure 4.1 : The geometry of an infinite insulated antenna. ....	43
Figure 4.2 : The lumped element model for the insulated antenna based on transmission line theory. ....	45
Figure 4.3 : Series reactance per meter for insulated area. ....	46
Figure 4.4 : Shunt susceptance per meter for insulated area ....	46
Figure 4.5 : Radiation term.....	46
Figure 4.6 : Normalized complex wave number. ( $\sigma_2 = 0, \epsilon_2 = 1, \sigma_4 = 5e-3, \epsilon_4 = 3$ ).....	47
Figure 4.7 : Correction term. ....	48
Figure 4.8 : Crosscut view of insulated antenna ( left : physical view , right : mathematical approximation ) .....	49
Figure 4.9 : Transmission line model : Asymmetric insulated dipole with two sections .....	51
Figure 4.10 : Transmission line model : Asymmetric insulated dipole with N sections. ....	52
Figure 4.11 : Physical view of representing a dipole as an equivalent monopole. ....	53
Figure 4.12 : ABCD impedance representation of a lumped series impedance and transmission line. ....	53
Figure 4.13 : Input impedance of an insulated dipole in see-water, and a dipole in air. ( $h =$ $0.6m, a = 1.5mm, b = 10.5mm, \epsilon_2 = 1, \mu_2 = 1, \sigma_2 = 0, \epsilon_4 = 81, \mu_4 = 1, \sigma_4 = 4$ ).....	55
Figure 4.14 : Input impedance of insulated dipole. ( $h = 0.6m, a = 1.5mm, b = 10.5mm, \epsilon_2$ $= 1, \mu_2 = 1, \sigma_2 = 0, \epsilon_4 = 7, \mu_4 = 1, \sigma_4 = 0$ ).....	55
Figure 4.15 : Input impedance of insulated WK-antenna in see-water. ( $h = 1m, a = 1.5mm, b$ $= 10.5mm, \epsilon_2 = 1, \mu_2 = 1, \sigma_2 = 0, \epsilon_4 = 81, \mu_4 = 1, \sigma_4 = 4$ ) .....	56
Figure 4.16 : Input impedance of insulated WK-antenna ( $h = 0.6m, a = 1.5mm, b = 10.5mm$ $, \epsilon_2 = 1, \mu_2 = 1, \sigma_2 = 0, \epsilon_4 = 7, \mu_4 = 1, \sigma_4 = 0$ ).....	56

Figure 4.17 : Effective permittivity of mathematical approximated borehole. (a = 1.5 mm, b = 10.5 mm, 18.85mm) .....	57
Figure 4.18 : Permittivity extracted from the wave number. ( $\epsilon_4=7, \epsilon_2=1, b=10.5$ mm, a = 1.5 mm) .....	57
Figure 4.19 : Comparison between bare dipole in dielectric constant of 2.1 and insulated antenna.....	57
Figure 5.1 : (a) Conducting, (b) Resistive and (c) Asymmetric dipole .....	59
Figure 5.2 : Input impedance of conducting dipole.....	60
Figure 5.3 : Far-field gain of conducting dipole.....	60
Figure 5.4 : Cross sectional view of insulated dipole in an AXT borehole. ( dipole situated in the centre of the hole ).....	61
Figure 5.5 : Cross sectional view of insulated dipole in an AXT borehole. ( dipole situated off-centre ).....	61
Figure 5.6 : Input resistance of centre insulated conducting dipole ( $\epsilon_{in} = 1-9, \sigma_{in} = 0, \epsilon_{in} = 7, \sigma_{in} = 0$ ).....	62
Figure 5.7 : Input reactance of centre insulated conducting dipole ( $\epsilon_{in} = 1-9, \sigma_{in} = 0, \epsilon_{in} = 7, \sigma_{in} = 0$ ).....	62
Figure 5.8 : Input resistance of off-centre insulated conducting dipole ( $\epsilon_{in} = 1-9, \sigma_{in} = 0, \epsilon_{in} = 7, \sigma_{in} = 0$ ).....	62
Figure 5.9 : Input reactance of off-centre insulated conducting dipole ( $\epsilon_{in} = 1-9, \sigma_{in} = 0, \epsilon_{in} = 7, \sigma_{in} = 0$ ).....	62
Figure 5.10 : Far-field gain of off-centre dipole ( $\theta$ component at $\phi = 0^\circ$ ).....	63
Figure 5.11 : Far-field gain of off-centre dipole for different insulation permittivities and $\phi$ angles.....	63
Figure 5.12 : Input resistance of centre insulated conducting dipole ( $\epsilon_{in} = 3.7, \sigma_{in} = 0, \epsilon_{in} = 7, \sigma_{in} = 1;3;5;7;9, \sigma_{out} = 0$ ).....	64
Figure 5.13 : Input reactance of centre insulated conducting dipole ( $\epsilon_{in} = 3.7, \sigma_{in} = 0, \epsilon_{in} = 7, \sigma_{in} = 1;3;5;7;9, \sigma_{out} = 0$ ).....	64
Figure 5.14 : Input resistance of conducting insulated antenna with and without a ambient loss factor.....	65
Figure 5.15 : Input reactance of conducting insulated antenna with and without a ambient loss factor.....	65
Figure 5.16 : Simulation geometry for pulse transmitting investigations .....	65
Figure 5.17 : Cross sectional view of AXT borehole and insulated antenna in <i>CST™</i> with the field cells ( refer to Figure 5.4 for the dimensions). .....	65
Figure 5.18 : Broadside trace of electric field for different surroundings. ....	66

Figure 5.19 : Magnitude of broadside electric field trace for different surroundings. ....	66
Figure 5.20 : Electric field at $\theta = 45^\circ$ for different surroundings. ....	67
Figure 5.21 : Magnitude of electric field at $\theta = 45^\circ$ for different surroundings. ....	67
Figure 5.22 : Simulation configuration of plane wave incidence on a dipole antenna.....	68
Figure 5.23 : Electric field time trace probed at antenna location.....	68
Figure 5.24 : Voltage transient at source for conducting dipole. ( $0^\circ$ plane wave incidence )	68
Figure 5.25 : Frequency spectrum of voltage transient at source for conducting dipole. ( $0^\circ$ plane wave incidence ) .....	68
Figure 5.26 : Voltage transient at source for conducting dipole. ( $45^\circ$ plane wave incidence ) .....	69
Figure 5.27 : Frequency spectrum of voltage transient at source for conducting dipole. ( $45^\circ$ plane wave incidence ) .....	69
Figure 5.28 : Input impedance of 100% Wu-King antenna. ....	71
Figure 5.29 : Far-field gain of 100% Wu-King antenna.....	71
Figure 5.30 : Input resistance of centre insulated resistive dipole ( $\epsilon_{in} = 1-9, \sigma_{in} = 0, \epsilon_{in} = 7, \sigma_{in}$ $= 0$ ) .....	72
Figure 5.31 : Input reactance of centre insulated resistive dipole ( $\epsilon_{in} = 1-9, \sigma_{in} = 0, \epsilon_{in} = 7, \sigma_{in}$ $= 0$ ) .....	72
Figure 5.32 : Input resistance of centre insulated resistive dipole ( $\epsilon_{in} = 3.7, \sigma_{in} = 0, \epsilon_{in} = 7, \sigma_{in}$ $= 1;3;5;7;9, \sigma_{out} = 0$ ) .....	72
Figure 5.33 : Input reactance of centre insulated resistive dipole ( $\epsilon_{in} = 3.7, \sigma_{in} = 0, \epsilon_{in} = 7, \sigma_{in}$ $= 1;3;5;7;9, \sigma_{out} = 0$ ) .....	72
Figure 5.34 : Input resistance of resistive insulated antenna with and without a ambient loss factor.....	73
Figure 5.35 : Input reactance of resistive insulated antenna with and without a ambient loss factor.....	73
Figure 5.36 : a) Continues loading b) centre loading and c) source loading .....	73
Figure 5.37 : Broadside trace of electric field for different percentage Wu-King loadings. ...	74
Figure 5.38 : Magnitude of the broadside electric field for different percentage Wu-King loadings .....	74
Figure 5.39 : Broadside electric field trace for different centre loadings. ....	74
Figure 5.40 : Magnitude of broadside electric field trace for different centre loadings. ....	74
Figure 5.41 : Broadside electric field trace for different source loadings. ....	75
Figure 5.42 : Magnitude of broadside electric field trace for different source loadings. ....	75
Figure 5.43 : Voltage transient at source for 100% Wu-King dipole. ( $0^\circ$ plane wave incidence ).....	76

Figure 5.44 : Frequency spectrum of voltage transient at source for 100% Wu-King dipole. ( 0° plane wave incidence ) .....	76
Figure 5.45 : Voltage transient at source for 50% Wu-King dipole. ( 0° plane wave incidence ) .....	77
Figure 5.46 : Frequency spectrum of voltage transient at source for 50% Wu-King dipole. ( 0° plane wave incidence ) .....	77
Figure 5.47 : Voltage transient at source for 100% Wu-King dipole. ( 45° plane wave incidence ).....	77
Figure 5.48 : Frequency spectrum of voltage transient at source for 100% Wu-King dipole. ( 45° plane wave incidence ) .....	77
Figure 5.49 : Input impedance of asymmetric dipole. ....	78
Figure 5.50 : Far-field gain of asymmetric dipole.....	78
Figure 5.51 : Input resistance of centre insulated asymmetric dipole ( $\epsilon_{in} = 1.9, \sigma_{in} = 0, \epsilon_{in} = 7, \sigma_{in} = 0$ ).....	79
Figure 5.52 : Input reactance of centre insulated asymmetric dipole ( $\epsilon_{in} = 1.9, \sigma_{in} = 0, \epsilon_{in} = 7, \sigma_{in} = 0$ ).....	79
Figure 5.53 : Far-field gain of asymmetric dipole (Theta component at $\theta = 0^\circ$ ).....	80
Figure 5.54 : Far-field gain of asymmetric dipole (Theta component at $\theta = 44^\circ$ ).....	80
Figure 5.55 : Far-field gain of asymmetric dipole ( Theta component at $\theta = 134^\circ$ ) .....	80
Figure 5.56 : Broadside trace of electric field for different percentage Wu-King loadings for the asymmetric dipole. ( $\theta = 0^\circ$ ) .....	81
Figure 5.57 : Magnitude of the broadside electric field for different percentage Wu-King loadings for the asymmetric dipole. ( $\theta = 0^\circ$ ) .....	81
Figure 5.58 : Broadside trace of electric field for different percentage Wu-King loadings for the asymmetric dipole. ( $\theta = 45^\circ$ ) .....	82
Figure 5.59 : Magnitude of the broadside electric field for different percentage Wu-King loadings for the asymmetric dipole. ( $\theta = 45^\circ$ ) .....	82
Figure 5.60 : Broadside trace of electric field for different percentage Wu-King loadings for the asymmetric dipole. ( $\theta = 135^\circ$ ) .....	82
Figure 5.61 : Magnitude of the broadside electric field for different percentage Wu-King loadings for the asymmetric dipole. ( $\theta = 135^\circ$ ) .....	82
Figure 5.62 : Voltage transient at source for 100% Wu-King asymmetric antenna. ( 0° plane wave incidence ).....	83
Figure 5.63 : Frequency spectrum of voltage transient at source for 100% Wu-King asymmetric dipole. ( 0° plane wave incidence ) .....	83
Figure 5.64 : Voltage transient at source for 100% Wu-King asymmetric antenna. ( 45° plane wave incidence ) .....	83

Figure 5.65 : Frequency spectrum of voltage transient at source for 100% Wu-King asymmetric dipole. ( 45° plane wave incidence ) .....	83
Figure 5.66 : Voltage transient at source for 100% Wu-King asymmetric antenna. ( -45° plane wave incidence ) .....	84
Figure 5.67 : Frequency spectrum of voltage transient at source for 100% Wu-King asymmetric dipole. ( -45° plane wave incidence ) .....	84
Figure 5.68 : Different aligned transmitter and receiver orientations in a borehole.....	85
Figure 5.69 : Voltage at receiver for setup shown in Figure 5.68 (a).....	85
Figure 5.70 : Voltage at receiver for setup shown in Figure 5.68 (b).....	85
Figure 5.71 : Voltage at receiver for setup shown in Figure 5.68 (c).....	86
Figure 5.72 : Voltage at receiver for setup shown in Figure 5.68 (a).....	86
Figure 6.1 : Extracting input impedance of optic modulator diode.....	88
Figure 6.2 : Forward voltage and current characteristics of HFBR 1404 [20] .....	88
Figure 6.3 : Input resistance of optic modulator diode.....	89
Figure 6.4 : Input reactance of optic modulator diode. ....	89
Figure 6.5 : DC bias circuit of optic modulator.....	89
Figure 6.6 : Input impedance of bias inductor.....	89
Figure 6.7 : Optic demodulator with external decoupling capacitor and shunted resistor. ....	90
Figure 6.8 : Schematic of dynamic measurement test for optical link. ....	91
Figure 6.9 : Dynamic range of optical link.....	92
Figure 6.10 : 15 MHz traces measured on digitised scope for various output loads on the optical link.....	93
Figure 6.11 : MAX 4200 transfer function.....	94
Figure 6.12 : BUF 601 transfer function .....	94
Figure 6.13 : Schematic of buffered optical link. ....	94
Figure 6.14 : Transfer function of buffered optical link ( $R_{in} = 50 \Omega$ , $R_s = 0$ ).....	95
Figure 6.15 : Transfer function of optical link for variable resistor values. ....	95
Figure 6.16 : Schematic of simulated transfer between transmitter and receiver ( $h_1 = h_2 = 1m$ (resistive arms), $h_2 = 300 mm$ (ground arm), $h_4 = 420 mm$ (ground arm) ). ....	97
Figure 6.17 : Time trace coupling between transmitter and receiver. ....	98
Figure 6.18 : Test bias circuit for MAR amplifiers .....	100
Figure 6.19 : Transfer function of MAR-6SM. ....	100
Figure 6.20 : Reverse isolation and impedances of MAR-6SM.....	100
Figure 6.21 : Transfer function of MAR-4SM. ....	100
Figure 6.22 : Reverse isolation and impedances of MAR-4SM.....	100
Figure 6.23 : Schematic of complete receiver. ....	101
Figure 6.24 : Transfer function of complete receiver.....	102

Figure 6.25 : To view of receiver. ....	102
Figure 6.26 : Bottom view of receiver.....	102
Figure 6.27 : Receiver fitting into copper pipe and 100% Wu-King antenna. ....	103
Figure 6.28 : Copper housing and LEMO connector. ....	103
Figure 6.29 : Final assembly of receiver into PVC pipe. ....	104
Figure 6.30 : Impulse response to input pulse of 5.3 mV <sub>p</sub> . ....	105
Figure 6.31 : Impulse response to input pulse of 17 mV <sub>p</sub> . ....	105
Figure 6.32 : Impulse response to input pulse of 50 mV <sub>p</sub> . ....	105
Figure 6.33 : Impulse response to input pulse of 170 mV <sub>p</sub> . ....	105
Figure 6.34 : Pulse transmitter used for the measurement of the active antenna. ....	106
Figure 6.35 : Structural image of probe test site.....	107
Figure 6.36 : Schematic of the implemented measurement testing radar probes. ....	107
Figure 6.37 : Initialising trace storage equipment. ....	108
Figure 6.38 : External FM noise measured by receiver.....	109
Figure 6.39 : Receiver time trace. ....	110
Figure 6.40 : Frequency response of received pulse. ....	110
Figure 6.41 : Frequency response of 6 order butterworth filter.....	110
Figure 6.42 : Original and filtered measured time trace of high impedance receiver. ....	111
Figure 6.43 : Frequency response of original and filtered time trace of high impedance receiver. ....	111
Figure A2-1 : Current voltage relationship in ideal capacitor.....	122
Figure A2-2 : Capacitor containing dielectric with loss.....	123
Figure A3-1: Equivalent circuit diagram of Marconi magnification meter.....	124
Figure A3-2 : Resonance curve. ....	125
Figure C2-1: Transmission line model : Symmetric insulated dipole with multiple sections. ....	134
Figure D1-1 : Voltage transient at source for 50% Wu-King dipole. ( 45° plane wave incidence ) .....	136
Figure D1-2 : Frequency spectrum of voltage transient at source for 50% Wu-King dipole. ( 45° plane wave incidence ) .....	136
Figure D1-3 : Voltage transient at source for 25% Wu-King dipole. ( 0° plane wave incidence ).....	136

Figure D1-4 : Frequency spectrum of voltage transient at source for 25% Wu-King dipole. ( 0° plane wave incidence ) .....	136
Figure D2-1 : Input resistance of centre insulated asymmetric resistive dipole ( $\epsilon_{in} = 3.7, \sigma_{in} = 0, \epsilon_{in} = 7, \sigma_{in} = 1;3;5;7;9, \sigma_{out} = 0$ ) .....	137
Figure D2-2 : Input reactance of centre insulated asymmetric resistive dipole ( $\epsilon_{in} = 3.7, \sigma_{in} = 0, \epsilon_{in} = 7, \sigma_{in} = 1;3;5;7;9, \sigma_{out} = 0$ ) .....	137
Figure D2-3 : Input resistance of resistive insulated asymmetric antenna with and without a ambient loss factor.....	137
Figure D2-4 : Input reactance of resistive insulated asymmetric antenna with and without a ambient loss factor.....	137
Figure D3-1 : Voltage transient at source for 50% asymmetric Wu-King dipole. ( 0° plane wave incidence ) .....	138
Figure D3-2 : Frequency spectrum of voltage transient at source for 50% asymmetric Wu-King dipole. ( 0° plane wave incidence ) .....	138
Figure D3-3 : Voltage transient at source for 50% asymmetric Wu-King dipole. ( 45° plane wave incidence ) .....	138
Figure D3-4 : Frequency spectrum of voltage transient at source for 50% asymmetric Wu-King dipole. ( 45° plane wave incidence ) .....	138
Figure D3-5 : Voltage transient at source for 50% asymmetric Wu-King dipole. ( -45° plane wave incidence ) .....	139
Figure D3-6 : Frequency spectrum of voltage transient at source for 50% asymmetric Wu-King dipole. ( -45° plane wave incidence ) .....	139
Figure D3-7 : Voltage transient at source for 25% asymmetric Wu-King dipole. ( 0° plane wave incidence ) .....	139
Figure D3-8 : Frequency spectrum of voltage transient at source for 25% asymmetric Wu-King dipole. ( 0° plane wave incidence ) .....	139

## Chapter 1

### **INTRODUCTION**

#### **1.1 Background**

The word radar is derived from *radio detection and ranging*, thus conveying the two purposes of detection and locating. Radio waves are transmitted from an arbitrary position, which are scattered from targets encountered and some of the energy is scattered back to a radio receiver, which is usually, but not always, located near the transmitter.

Radar has many uses ranging from military target detection, probing planets across the solar system, mapping landscapes, etc. Ground-penetrating radar focuses on the exploration of subsurface areas to gain information about the structural composition in order to aid geological understanding. In essence, radar functions as the eyes of a human being in a medium that cannot sustain life or mobility. Deployment of a radar system for ground probing purposes consists of surface penetration where the radar is situated on the interface between two mediums (air and ground) or by situating the radar directly in the medium (ground) of interest by drilling boreholes into the ground (Figure 1.1).

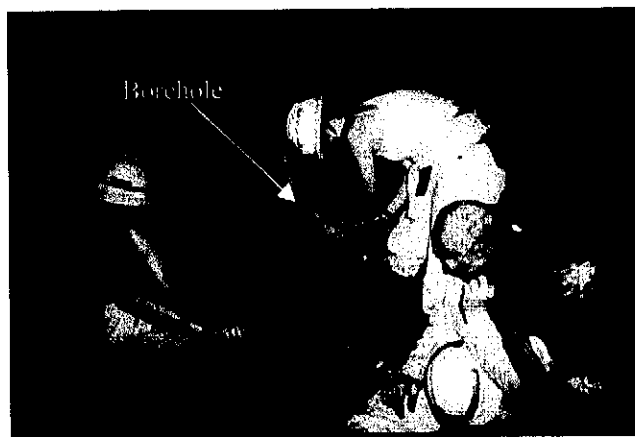


Figure 1.1 : Deployment of borehole radar in an incline borehole [1]

## *List of Tables*

Table 2.1 : Resistor values representing a Wu-King profile with $f_{\text{design}}=500$ MHz. ....	11
Table 4.1 : 100% Wu-King resistor values along a 1m length of dipole arm. ....	55
Table 5.1 : Resistor values representing a Wu-King profile with $f_{\text{design}}=75$ MHz. ....	70
Table 6.1 : Receiver amplification calculations. ....	98
Table 6.2 : Amplifier specifications. ....	99

## Chapter 1

### INTRODUCTION

#### 1.1 Background

The word radar is derived from *radio detection and ranging*, thus conveying the two purposes of detection and locating. Radio waves are transmitted from an arbitrary position, which are scattered from targets encountered and some of the energy is scattered back to a radio receiver, which is usually, but not always, located near the transmitter.

Radar has many uses ranging from military target detection, probing planets across the solar system, mapping landscapes, etc. Ground-penetrating radar focuses on the exploration of subsurface areas to gain information about the structural composition in order to aid geological understanding. In essence, radar functions as the eyes of a human being in a medium that cannot sustain life or mobility. Deployment of a radar system for ground probing purposes consists of surface penetration where the radar is situated on the interface between two mediums (air and ground) or by situating the radar directly in the medium (ground) of interest by drilling boreholes into the ground (Figure 1.1).

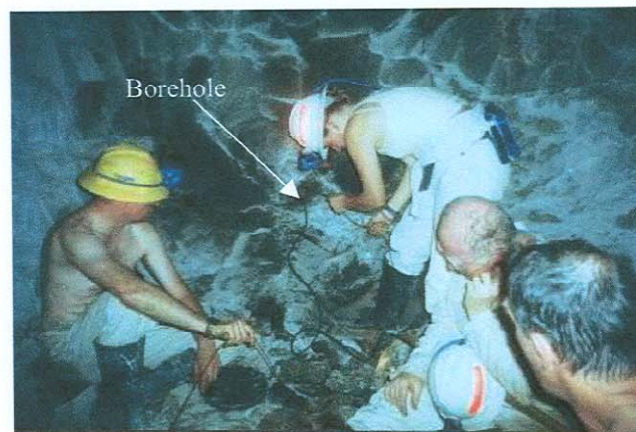


Figure 1.1 : Deployment of borehole radar in an incline borehole [1]

The first functional borehole radar, developed by J. Hargreaves [2] and D. M. Claassen [3], showed that using radio waves as a non-destructive method of surveying the mine environment proves to be beneficial for the geologist in gathering extra information about ore behaviour. Radar may be the key to safety in an unforgiving mine environment and unnecessary life threatening accidents may be prevented by investigating the unseen.

## 1.2 Current borehole radar system

The backdrop for this thesis is a discussion of the J. Hargreaves [2] and D. M. Claassen [3] borehole radar technology that is currently being deployed in the South African mining industry. The currently used radar technology involves impulse radar with a frequency content of 20-80 MHz for exploring rock environments. Sections 1.2.1-1.2.4 discuss the basic operation of the system and will be referred to as the current radar technology throughout this work. Due to the nature of the mine environment, radar instruments should be low-cost in case the probes are lost in the boreholes.

### 1.2.1 Transmitter

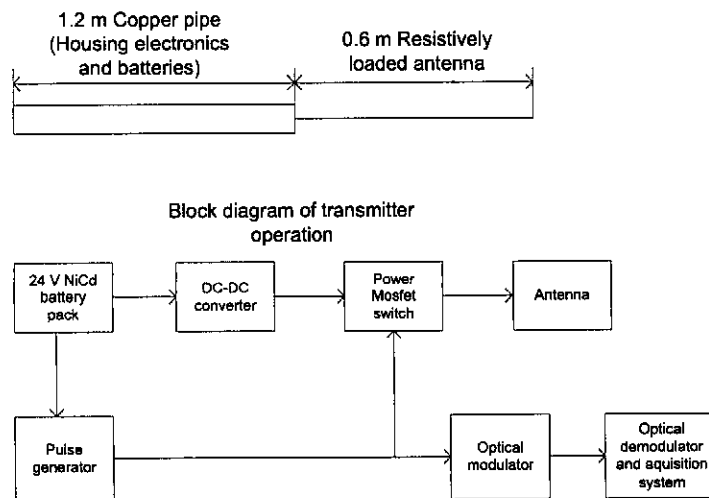


Figure 1.2 : Transmitter dimension and electronic operation block diagram

The transmitter consists of a 0.6m resistively loaded copper wire antenna driven against a 1.2m ground arm (Figure 1.2). The structure is asymmetric due to there being no plane of electrical symmetry. The transmitter is capable of transmitting a pulse with adequate spectral density up to 80 MHz. The antenna is constantly charged to a potential of a 1000 V. The pulse is generated by the sudden discharge of the antenna through a power Mosfet. The transmitter also provides for a trigger or reference signal in order to predict the propagation distances of targets and to permit stacking of time traces to improve the dynamic range of the system.

### 1.2.2 Receiver

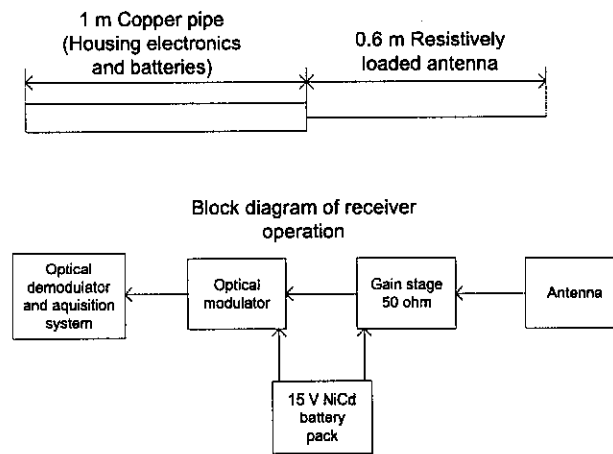


Figure 1.3 : Receiver dimensions and electronic operation block diagram

The receiver consists of a 1m ground arm and 0.6m resistively loaded wire antenna. A amplifier stage with a low noise front end provides sufficient dynamic range and amplification of the received signal. The receiver is a 50  $\Omega$  receiver chain and no matching was applied to the antenna. The amplified signal is fed to an analogue optic link system to the data acquisition system for sampling and storage.

### 1.2.3 Optical link

The optical link provides electrical isolation between the transmitter and receiver and guides the reference and received signal from the transmitter and receiver to the data storage system. Since a borehole survey may range to more than 300m, the optical link is a practical solution to cable losses, weight and ease of handling above long coaxial cables. Using coaxial or conducting cables as signal path along the borehole would influence the radiation characteristics of the system.

### 1.2.4 Data acquisition system

The optical signal as provided by the optical link is demodulated to an electrical trace for sampling through an analogue-to-digital converter. A general computer is used for controlling and storage of the digitised traces.

## 1.3 Thesis outline

This work primarily focuses on the electromagnetic characterization of borehole probes in the frequency range 10-100 MHz.

*Chapter 2* verifies the two different numerical solutions (*MoM*, *FD-TD*) for simulating electromagnetic behaviour of conductive and non-conductive structures. Section 2.2.2 shows that the different commercial codes are suitable for modelling resistively loaded antennas necessary for pulsed radar applications. Since the antennas will be insulated in order to protect the probes in the borehole, it was essential to determine whether the solutions are accurate for dielectric insulated antennas (Section 2.2.3).

General radiation aspects of a simple conductive dipole antenna are discussed in *Chapter 3*. A travelling wave element (Section 3.2.1) was proposed and used to explain and graphically illustrate transient behaviour on the antenna (Section 3.2.2). Section 3.3 discusses the dynamic charge behaviour of narrow pulses on a dipole antenna. This chapter helps the engineer to develop a feel for the dynamic behaviour of radiating wire antennas excited by limited signals.

D. M. Claassen [3] used a transmission line model to simulate the behaviour of the current radar probes. Due to the simplicity of the model it was implemented and is discussed in *Chapter 4* and verified by comparison with a commercial electromagnetic code (Section 4.4). The radar antenna is described in terms of known engineering parameters to aid the further understanding of the performance of probes in a frequency domain sense.

A conductive (Section 5.2), resistive (Section 5.3) and asymmetrical (Section 5.4) antenna with and without insulation with fixed dimensions are presented and investigated in *Chapter 5*. A time and frequency domain analysis using the verified simulation packages of *Chapter 2* was conducted in order to combine both domains to produce a useful solution for a borehole probe. The simulations showed that an active antenna might provide a possible solution when used as a receiver antenna.

*Chapter 6* introduces the active antenna (Section 6.2) as a possible solution by substituting the 50  $\Omega$  receiver system with a high impedance system. The optical link is re-examined in Section 6.2 and possible improvements to reduce the component requirement of the driver circuit are proposed, constituting in a flatter transfer function. Section 6.2.3.2 examines the current feedback amplifier used to produce the high impedance node at the receiver input. The amplification chain is presented and discussed in Section 6.2.4.2, which also deviates from the components used in the current radar applications. The impulse response of the receiving electronics of the active antenna is presented in Section 6.2.4.5, and open air measurements of the full receiver are compared with the conventional 50  $\Omega$  system in Section 6.4.

## Chapter 2

# **VERIFICATION OF ELECTROMAGNETIC SIMULATION TOOLS**

### **2.1 Introduction**

Normally the validation of simulation results is presented in a report as the results are generated. In this work the validation will be presented first in this chapter, as it is also intended to acquaint the reader with both the basic electromagnetic properties of the antennas used and their environment.

Two numerical software packages, namely FEKO™ and CST MICROWAVE STUDIO™ were used as modelling tools for different configurations of wire antennas. FEKO™ and CST™ are able to model cylindrical layers with different electrical properties that simulate the physical environment of the radar antennas. Numerical modelling provides more freedom for testing and analysing electromagnetic structures, especially in the difficult borehole environment, than constructing expensive prototypes does.

The FEKO™ program is based on the *Method of Moments (MoM)*. Here electromagnetic fields are obtained by first calculating the electric surface currents on conducting surfaces and equivalent electrical and magnetic surface currents on the surface of a dielectric solid. The currents are calculated using a linear combination of basis functions, where the coefficients are obtained by solving a system of linear equations. Once the current distribution is known, further parameters can be obtained, e.g. the near field, the far field, radar cross sections, directivity or the input impedance of antennas.

CST™ is based on a *Finite Difference Time Domain* formulation (*FD-TD*). The program also provides a widely validated time-dependent thin-wire electric-field equation that is used to model the wire antennas.

## 2.2 Experimental verification

The input impedance of three wire antennas consisting of a conducting, a resistive and an insulated monopole was measured with an 8510 vector network analyser. The antennas were constructed on a 0.6m×0.6m ground plane. This work mainly concentrates on wire antennas in the frequency band between 10-100 MHz, however the measured monopoles were scaled in dimension by a factor of 10 increasing the frequency band to 0.1-1 GHz.

It is difficult to verify antennas at low frequencies due to the absorption materials needed to construct an enclosed anechoic chamber to reduce reflections from the surrounding environment. These wall reflections induce currents on the antenna that will affect the results. The input impedance will be used to validate results since it is an accurate and quick method for verifying wire antenna operation. The far-field is a less sensitive validation parameter since it is the integration of the current distribution on the wire which is inherently described at a specific point by the input impedance.

The simulations were performed for dipole structures to eliminate any unnecessary ground planes, which will cause an increase in simulation time. A plane of electrical symmetry at the source point is common practice for symmetrical antennas. From image theory it can be shown that the measured input impedance of the monopole antennas, is multiplied by two, in order to represent the impedance of a dipole structure. Measurements were made using a monopole structure rather than a dipole as this eliminates the need for a balun to suppress the common mode currents on the outside sleeve of the unbalanced coaxial feed.

### 2.2.1 Conductive monopole

The simplest example for validation uses a monopole antenna, as shown in Figure 2.1, and this will be used as a basic starting point to validate resistive and insulated wire antennas.

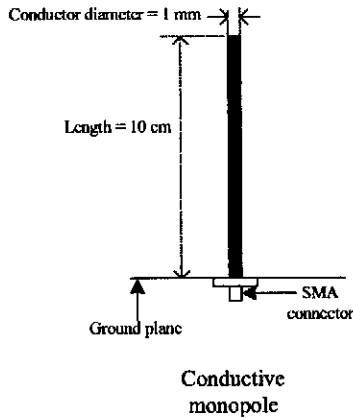


Figure 2.1 : Physical dimension of conducting monopole

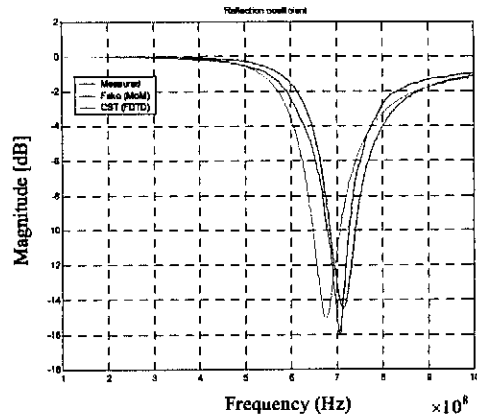


Figure 2.2 : Magnitude (reflection coefficient) of conducting monopole of Figure 2.1

The resonance frequency deviates less than 5% between the measured and simulated results (Figures 2.2 and 2.3). The measured and simulated resonance frequencies seems correct if the  $\lambda/4$  is taken as the resonance frequency in air (750 MHz). Bear in mind that there will be some spread capacitance at the monopole end, effectively increasing the electrical length of the monopole. Stutzman and Thiele ([4], p172) discuss the percentage shortening required for a specific length-to-diameter ratio dipole to produce the correct resonance frequency.

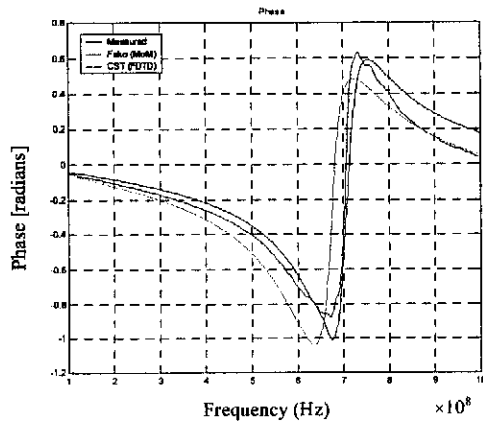


Figure 2.3 : Phase (reflection coefficient) of conducting monopole of Figure 2.1

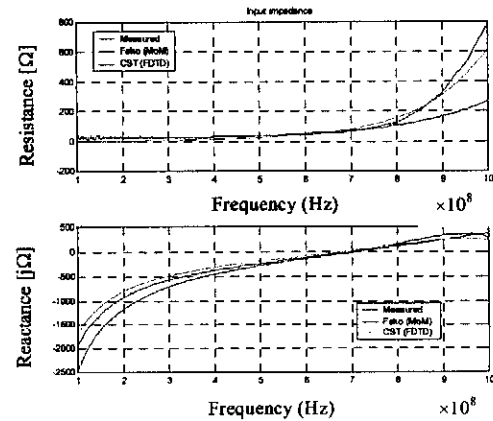


Figure 2.4 : Input impedance of conducting monopole of Figure 2.1

The resonance frequency can be approximated by,

$$f_{res} = v \frac{2c_a}{\lambda_{free}} \quad [Hz] \quad (2.1)$$

For a length-to-radius ratio of 100,  $v \approx 0.475$  and  $f_{res} = 712$  MHz. The first anti-resonance starts to appear at 1 GHz (Figure 2.4). The large difference in the resistance (Figure 2.4) starting at 800 MHz is expected, as it is difficult to accurately determine the input impedance at the anti-resonance, because the source point becomes a high impedance. The *FD-TD* code gives a better comparison at the anti-resonance, probably because it is a transient solver. At 10 MHz the antenna resembles a capacitor and the antenna can be modelled as a short transmission line.

### 2.2.2 Resistively loaded monopole

In many applications, an antenna must operate effectively over a wide range of frequencies. Many broadband antennas are currently used e.g. the spiral antenna, horn antenna or bow-tie antenna. These antennas are effective, but are not used at relatively low frequencies due to their physical dimensions. The spiral antenna will not be an adequate radiator for pulsed radar applications due to frequency dispersion.

Travelling wave wire antennas also display broadband qualities but seem to be more appealing to pulsed radar due to their ability to suppress dispersion, and their physical structure is more suitable for borehole applications. Resistive loading on a wire antenna can be used to reduce end reflections on a short antenna, making it operate as a travelling wave antenna. The main disadvantage of resistively loaded antennas is that their efficiency is usually less than 50% (the term travelling wave antenna refers to the notion that the reflected wave is not strongly present on the antenna).

The impedance profile was based on a paper introduced by T. T. Wu and R. W. P. King [5] and will be referred to as the Wu-King profile. This impedance profile is a function of the axial coordinate  $z$  situated along the antenna arm and is given by,

$$Z_{Wu-King}(z) = \frac{60\Psi}{h - |z|} \quad [\Omega/m] \quad (2.2)$$

where  $h$  is the length of one antenna arm and  $\psi$  is the complex expansion parameter. This equation is derived and discussed in *Appendix A.1*. The efficiency of their non-reflecting antennas

has been calculated to be below 10% for low frequencies, where  $h/\lambda \leq 1/4$  and above 10% for  $h/\lambda > 1/4$ , but does not exceed 45%.

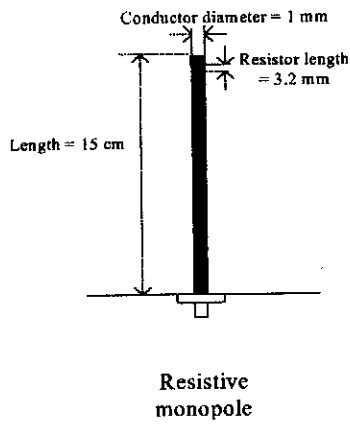


Figure 2.5 : Physical dimension of resistive monopole

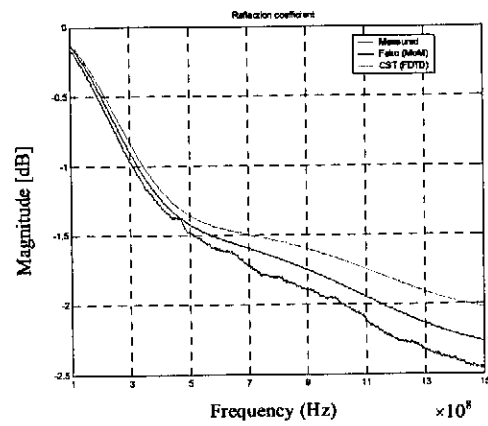


Figure 2.6 : Magnitude (reflection coefficient) of resistive monopole of Figure 2.5

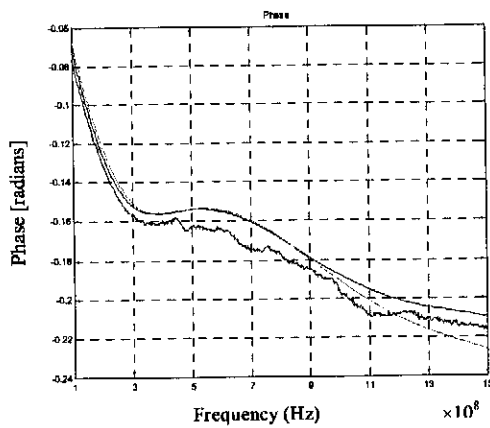


Figure 2.7 : Phase (reflection coefficient) of resistive monopole of Figure 2.5

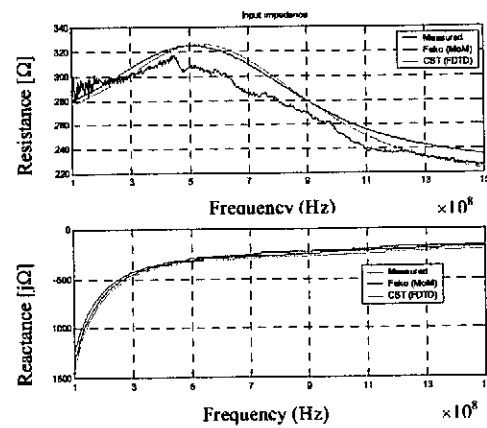


Figure 2.8 : Input impedance of resistive monopole of Figure 2.5

The resistively loaded monopole was constructed as a conducting strip on a dielectric (thickness = 0.5 mm, permittivity ( $\epsilon_r$ ) = 2.3) and no cylindrical wire was used. The strip was used due to the ease with which the surface-mounted resistors can be attached. The equivalent strip width for a cylindrical antenna of radius  $r_{cyl}$  was calculated by C. M. Butler [6] to be,

$$w_{equ} = 4r_{cyl} \quad (2.3)$$

where  $w_{\text{equ}}$  is the equivalent strip width. A wire radius  $r_{\text{cyl}} = 1.5 \text{ mm}$  ( $w_{\text{equ}} = 6 \text{ mm}$ ) was used. Only the real part of the Wu-King profile,  $\Psi$ , has been approximated by a step-function profile introduced by discrete resistors. The imaginary part of  $\Psi$  is very small compared to the real part for lower design frequencies and is therefore often omitted. The length of the resistive monopole was scaled by a ratio 1:15 for construction and measurement. This was done to fit a sufficient number of surface mount resistors along the length of the antenna, and to preserve the point element approximation of the resistors. The Wu-King expansion parameter was numerically integrated and a design frequency of 500 MHz was chosen that represents the resonant length when the antenna is conducting. A parametrical study conducted by S. Keller [7] showed that more than 3 resistors are needed per  $\lambda/4$  of the highest frequency in the band. For fewer resistors the travelling wave behaviour vanishes and interim resonance occurs between resistors. To meet criteria, the resistive monopole contained 9 discrete resistors (Table 2.1).

Resistor position (mm)	8.3	25	41	58	75	91	108	125	141
Resistor value ( $\Omega$ )	25	54	62	73	87	110	147	223	481

Table 2.1 : Resistor values representing a Wu-King profile with  $f_{\text{design}}=500 \text{ MHz}$

The 100% Wu-King antenna described above (Figure 2.5) was built and measured, as was the conducting monopole. The simulations compared well with the measured results. The magnitude of the reflection coefficient seemed very poor when matched to  $50 \Omega$  (Figure 2.6). From Figure 2.8 it is evident that the resistively loaded antenna is not compatible with a typical  $50 \Omega$  system without impedance matching. The antenna appears to be very capacitive up to 300 MHz and the phase (Figure 2.7) is linear, as with a transmission line. At 500 MHz (the resonant frequency when the antenna was conducting) the resistance rises steeply. After 500 MHz the resistance falls gradually, while the reactance stays stable. The phase does not change rapidly at any frequency, but instead follows a relatively linear drop except in the region of 500 MHz.

### 2.2.3 Insulated monopole

Current radar probes are insulated with a polyurethane epoxy. The epoxy is a dark grey, two-part, flexible encapsulant designed to provide environmental protection without causing component stress by shrinkage during cure. The data sheets state that the product has a dielectric constant of

4 and a dissipation factor of 0.04. The polyurethane was used as insulation for verification purposes.

### 2.2.3.1 Measuring dielectric properties of materials

A study aimed at measuring dielectric properties was conducted to verify the electrical properties of polyurethane over the frequency band of interest. Two methods involving an RC circuit and a resonating RCL circuit were used. The RC circuit method will be discussed in this section. For mathematical detail, refer to *Appendix A.2* on the RC circuit and *Appendix A.3* for the Marconi Instruments™ resonating RCL dielectric meter.

Figure 2.9 shows the polyurethane sample and the Marconi test jig used in conjunction with a HP 4285A RLC meter. For the purposes of this measurement the jig can be seen as simply a single, parallel plate capacitor. The RLC meter can measure impedances (phase and magnitude) up to 30 MHz. Figure 2.10 gives the full equivalent circuit representation for the test jig when loaded with a dielectric sample, as well as the measuring setup. Three measurements were conducted to

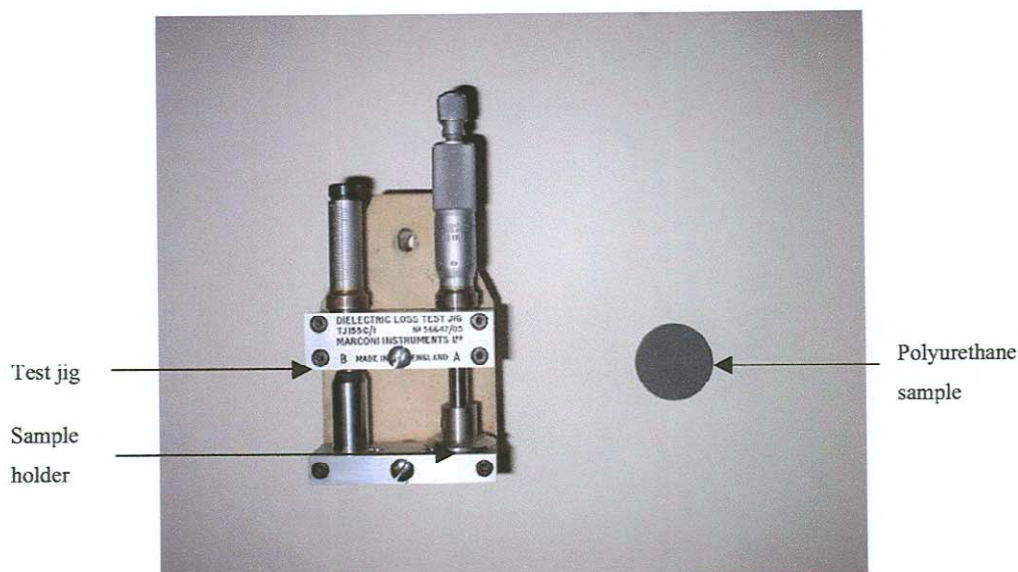


Figure 2.9 : Polyurethane sample and Marconi test jig

extract all the parameters of the circuit. First the sample holder is shorted to produce the series inductance ( $L_{series}$ ) and resistance ( $R_{series}$ ) of the leads and jig (Figure 2.11(a)). Secondly the sample is added to produce the input impedance  $Z_{sample}$ . A third measurement (Figure 2.11(b)) was made with the sample removed without adjusting the width of the sample clamps on the jig. The permittivity and loss tangent can be determined as follows,

$$Z_s = Z_{sample} - Z_{short} \quad (2.4)$$

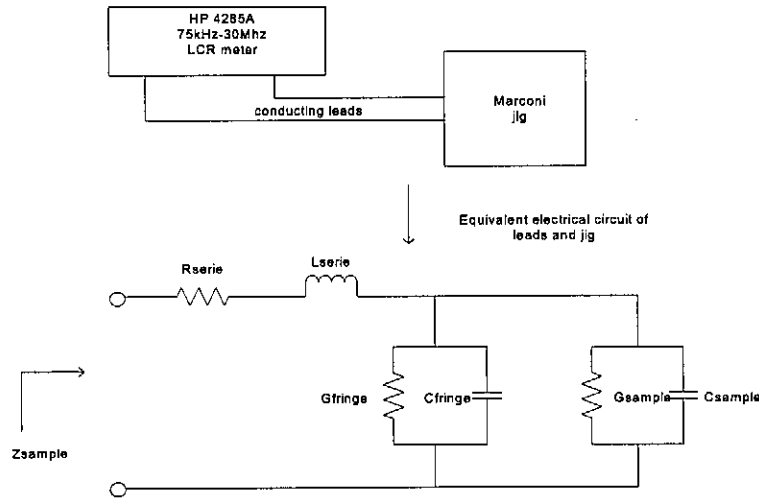


Figure 2.10 : Measuring setup and equivalent electric representation of the test jig and sample

$$Z_o = Z_{open} - Z_{short} \quad (2.5)$$

$$Y_s = \frac{1}{Z_s} = G_s + j\omega C_s \quad (2.6)$$

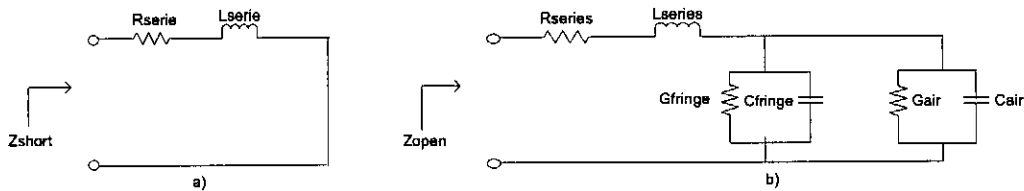


Figure 2.11 : (a) Equivalent electric circuit of jig when the clamps are shorted, (b) and when open

$$Y_o = \frac{1}{Z_o} = G_o + j\omega C_o \quad (2.7)$$

$$C_s = C_{sample} + C_{fringe} \quad (2.8)$$

$$C_o = C_{air} + C_{fringe} \quad (2.9)$$

$$C_s - C_o = \frac{A\epsilon_o}{d} (\epsilon_r - 1) \quad (2.10)$$

where  $C_{fringe}$  = Capacitance associated with the fringing fields around the jig clamps

A = Area of the clamp

d = Thickness of sample

$\epsilon_o = 8.854 \times 10^{-12}$  [F/m]

The dielectric constant can be obtained from equation (2.11). The loss tangent can be obtained as follows,

$$C_{air} = \frac{A\epsilon_o}{d} \quad \text{and} \quad G_{air} = 0 \quad (2.11)$$

No loss is associated with an air core.

$$\tan \delta = \frac{1}{\omega R_{sample} C_{sample}} \quad (2.12)$$

The polyurethane sample was measured using both techniques described above. The dielectric constant that was used for the simulations was 3.7 @ 45 MHz (Figure 2.12) and the dissipation factor was 0.02. The dissipation factor inherently describes the frequency response of the polyurethane. As expected, the loss tangent (Figure 2.13) increases rapidly at the lower frequencies as the polyurethane starts to become an isolator (typical high pass response expected for an capacitor). The two measuring techniques compared reasonably well with each other.

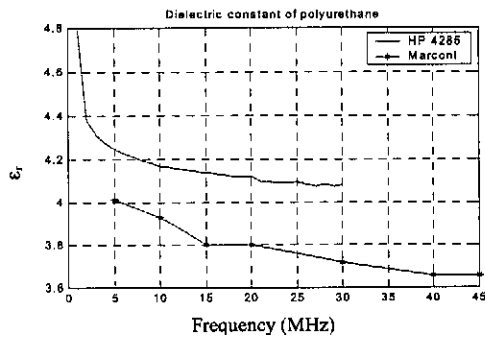


Figure 2.12 : Dielectric constant of polyurethane

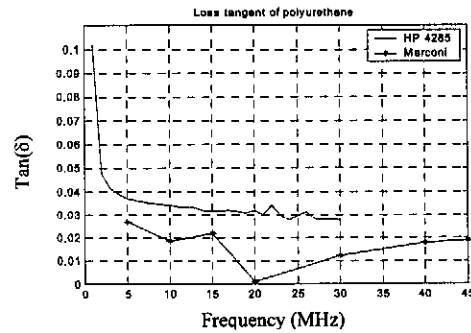


Figure 2.13 : Loss tangent of polyurethane

### 2.2.3.2 Measured and simulated results of insulated antenna

A cylindrical monopole with the same dimensions and scale as constructed in Section 1.2.1 was insulated with 6mm of polyurethane (Figure 2.14). The insulated antenna was measured and the input impedance was compared with simulated FEKO™ and CST™ results.

Various FEKO™ formulations were used to model the insulation and these will be discussed throughout this section. The insulation had a significant effect on the resonating frequency, scaling it down by 200 MHz compared to the conducting monopole (Figures 2.15, 2.16). In FEKO™ the insulation was added by using the DI card that represents the dielectric properties of the region enclosed or excluded (depending on the orientation of the normal vector) by equivalent dielectric current surfaces. Figure 2.17 shows that the anti-resonance is difficult to calculate with the simulation tools as discussed in Section 2.2.2. In the region of resonance both, FEKO™ and CST™ provide good agreement with the measured result.

FEKO™ provides two formulations for managing dielectric or magnetic coated wires. The advantage of using the dielectric coating rather than the dielectric surface currents is that it requires less processing power and reduces the simulation time considerably. The first formulation is a technique presented by B. D. Popovic [8] that transfers the coating into a distributed inductance along the wire, and the change in capacitance is taken into account by adjusting the radius of the wire. The only drawback is that if the loss tangent of the wire coating and ambient medium differ the new wire radius is complex, which has no physical meaning.

The second technique involves the volume equivalence principle (VEP) that introduces volume polarization current densities. This formulation can support problems where the loss tangent of the dielectric coating and surrounding medium differ.

Figure 2.18 (a) shows the insulated antenna, where the dielectric surfaces (SIE method) were replaced by a dielectric coating using the VEP. The volume equivalence principle were used due to the different loss tangent for air and the insulation. Figures 2.18 (b) and (c) make use of both the dielectric coating and the DI card.

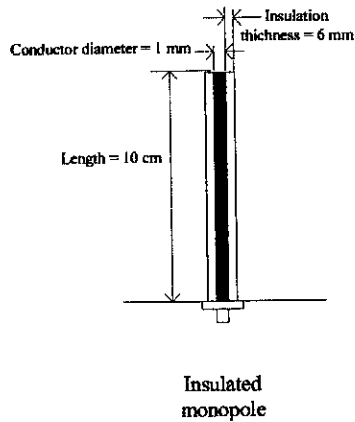


Figure 2.14 : Physical dimension of insulated monopole

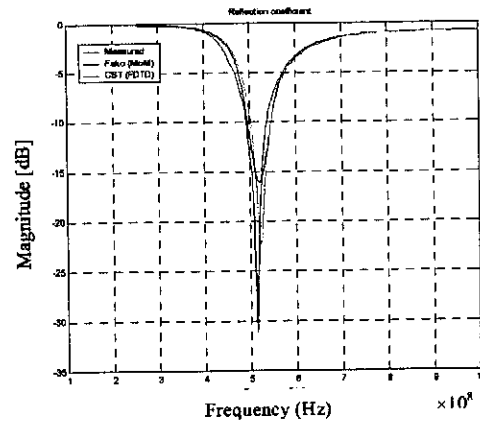


Figure 2.15 : Magnitude (reflection coefficient) of insulated monopole of Figure 2.14

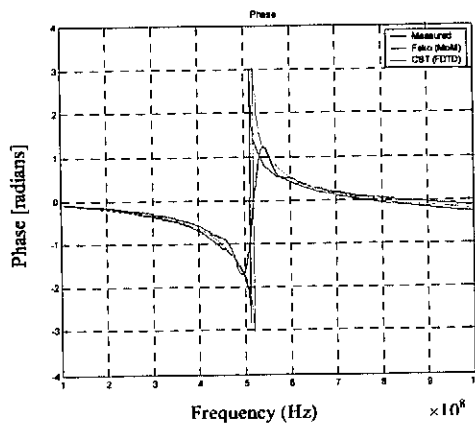


Figure 2.16 : Phase (reflection coefficient) of insulated monopole of Figure 2.14

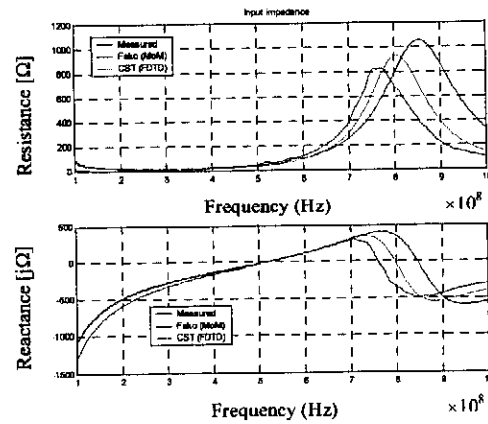


Figure 2.17 : Input impedance of insulated monopole of Figure 2.14

The dielectric coating represented the insulation while the DI card and surrounding ambient were set to the electrical properties associated with air or a vacuum. This was done to test the formulation and the results should not differ as, in principle, no electrical change has been made to the problem. Using the DI card in association with the dielectric coating provides a way of constructing any borehole environment while minimizing the computer processing time of the problem. Figure 2.18(c) shows the antenna being shifted off-centre to simulate the real problem of a radar lying in the borehole.

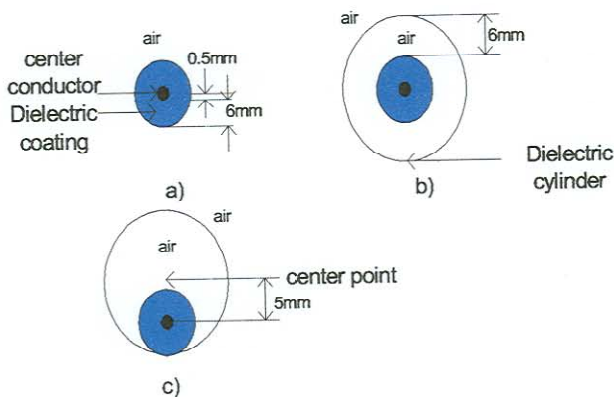


Figure 2.18 : (a) Dielectric coating, (b) Centre dipole with dielectric coating and dielectric cylinder, (c) Off-centre dipole with dielectric coating and dielectric cylinder

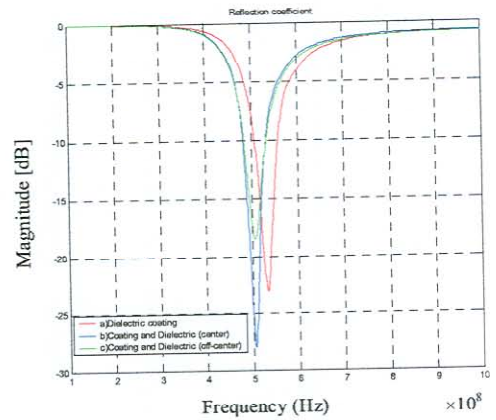


Figure 2.19 : Magnitude (reflection coefficient) of insulated dipole with different formulation

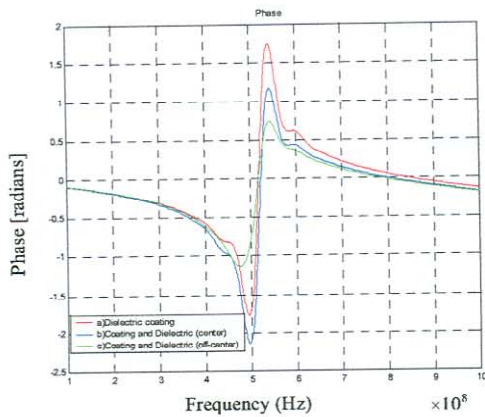


Figure 2.20 : Phase (reflection coefficient) of insulated dipole with different formulations

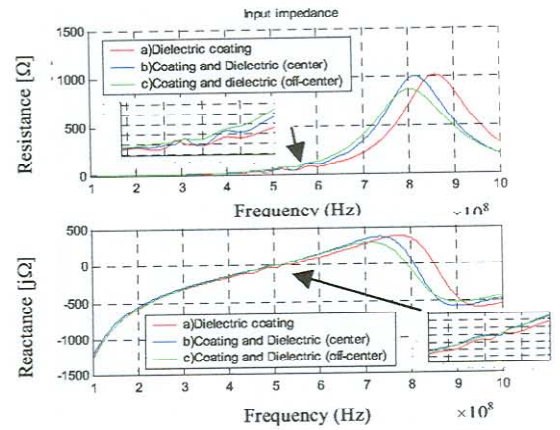


Figure 2.21 : Input impedance of insulated dipole with different formulations

The resonating frequency stayed the same, compared to previous results (Figures 2.19, 2.20). The input impedance (Figure 2.21) displays a strange ripple in both the reactance and resistance. This ripple is only visible around the resonating frequency. The ripple is more severe when the dielectric cylinder is added, but is already visible when only the coating is added. The coating formulation may pose some trouble when the radius of the coating is too thick, which it may be for this case. Figures 2.22 to 2.24 show that replacing the dielectric coating with a second dielectric surface as shown in Figure 2.25 provides adequate results, even when the centre dielectric cylinder is off-centre. A small ripple near resonance is again present.

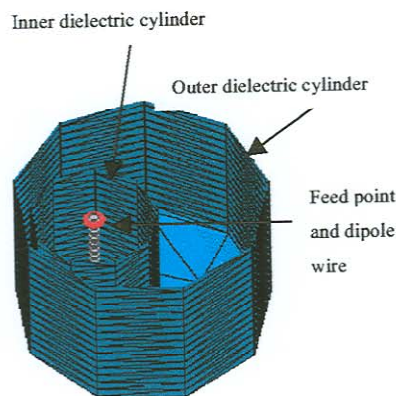


Figure 2.22 : Schematic representation of off-centre dipole in two dielectric cylinders

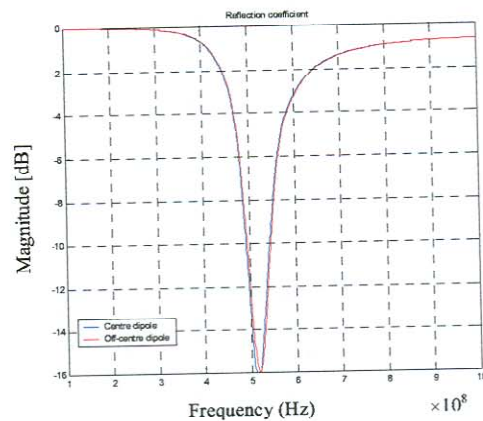


Figure 2.23 : Magnitude (reflection coefficient) of insulated dipole with double dielectric cylinders

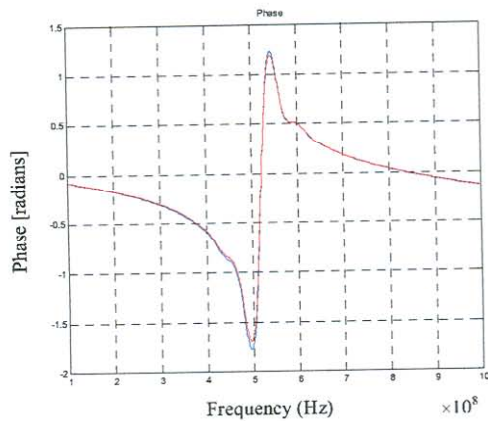


Figure 2.24 : Input impedance of insulated dipole with double dielectric cylinders

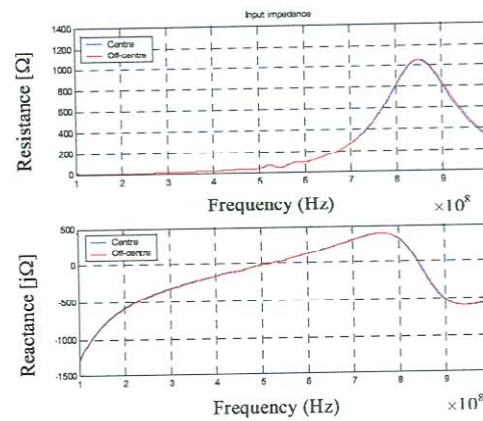


Figure 2.25 : Phase (reflection coefficient) of insulated dipole with double dielectric cylinders

### 2.3 Conclusion

The goal of this chapter was to introduce the basic properties of the antennas to be studied and their environment, and to introduce and validate two electromagnetic simulation programmes as a feasible means of investigating conducting, resistively loaded and dielectric loaded antennas. The transient solver, CST™ plays an important role in investigating time traces, which is important to any pulse radar system.

Both CST™ and FEKO™ generated results that proved to be an accurate means of investigating wire antennas in the borehole environment without resorting to physical measurement techniques.

## Chapter 3

# ***INVESTIGATING TIME DOMAIN RADIATION FOR WIRE ANTENNAS***

### **3.1 Introduction**

A broadband antenna for pulse applications cannot be regarded as broadband if it is evaluated only by its stable input impedance over a wide range of frequencies, because time constants effecting the pulse duration may cause some stretching of the received pulse which is not always visible in the phase of an electrically small radiator. The function of an antenna is the efficient radiation of the energy content of the feed. This chapter investigates general radiation aspects of a wire radiator (conducting dipole) in the time domain for limited energy input signals.

Section 3.2 illustrates and discusses dipole radiation with a general excitation, e.g. a pulse in time by using approximations no worse than those used for analysing and teaching time-harmonic excitation, viz. an assumed current distribution. This analysis in the time domain provides physical understanding not readily available from the time-harmonic analysis. Section 3.2.1 introduces a mathematical travelling wave element that was used as a building block for constructing a conducting dipole (Section 3.2.2). Section 3.2.3 compares the results obtained from the travelling wave element antenna with *FD-TD* and shows that the approximation does not include secondary effects, e.g. attenuation and dispersion along the dipole. Charge behaviour along a dipole arm is visually illustrated and discussed in Section 3.3.

### **3.2 Investigating dipole radiation using travelling wave elements**

G. S. Smith [11] showed that an analogy could be drawn between the radiation caused by antennas excited by a short pulse of current and the radiation from a moving point charge. The radiation from a fictitious travelling wave element (Section 3.2.1) was derived and used as a building block for a dipole antenna (Section 3.2.2). The theoretical model was compared with an

*FD-TD* integral solution in order to establish its limitations on different excitation sources and on current behaviour on the wire (Section 3.2.1).

### 3.2.1 The basic travelling wave element

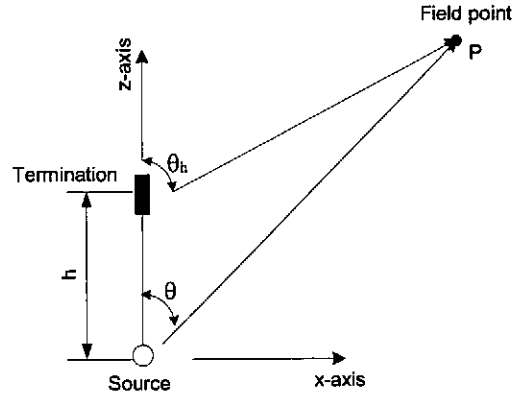


Figure 3.1 : The geometry and coordinate system of the basic travelling wave element [11].

Figure 3.1 shows the geometry of the travelling wave element and the coordinates associated with the derivation of the radiating fields. The element consists of a current source  $I_s(t)$  at one end and a perfect termination at the other end. The source will consist of a uniform pulse that will travel at the speed of light along the length of the element without attenuation. The termination will absorb the pulse. The current described above can be mathematically presented by;

$$I(z, t) = I_s\left(t - \frac{z}{c}\right)[U(z) - U(z - h)] \quad (3.1)$$

and the charge per unit length on the element, as obtained in *Appendix B1*, is,

$$Q(z, t) = Q_s\left(t - \frac{z}{c}\right)[U(z) - U(z - h)] + q_0(t)\delta(z) + q_h(t)\delta(z - h) \quad (3.2)$$

where

$$\begin{aligned} Q_s(t) &= I_s(t) / c \\ q_0(t) &= - \int_{t'=-\infty}^t I_s(t') dt' \\ q_h(t) &= \int_{t'=-\infty}^t I_s\left(t' - \frac{h}{c}\right) dt' \end{aligned} \quad (3.3)$$

and  $\delta$  is the Dirac delta function.

Equation 3.2 describes the behaviour of a wave with a positive surface charge on the element. As the positive charge  $Q_s$  leaves the source and travels at the speed of light along the element, a negative charge accumulates at the source. The element remains electrically neutral and obeys the law of charge conservation. As the positive charge leaves the element from the perfect termination, a positive charge build-up occurs at the upper end and the element enters a state of electro-quasi statics. The electromagnetic field describing this motion of charge/current as derived by G. S. Smith in *Appendix B2* is given as;

$$E(r, t) = \frac{1}{4\pi\epsilon_0} \left[ \frac{q_o(t - \frac{r}{c})}{r^2} \hat{r} + \frac{q_h(t - \frac{r_h}{c})}{r_h^2} \hat{r}_h + \frac{\cot(\frac{\theta}{2})I_s(t - \frac{r}{c})}{cr} \hat{\theta} - \frac{\cot(\frac{\theta_h}{2})I_s(t - \frac{h}{c} - \frac{r_h}{c})}{cr_h} \hat{\theta}_h \right] \quad (3.4)$$

$$B(r, t) = \frac{\mu_0}{4\pi} \left[ \frac{\cot(\frac{\theta}{2})I_s(t - \frac{r}{c})}{r} - \frac{\cot(\frac{\theta_h}{2})I_s(t - \frac{h}{c} - \frac{r_h}{c})}{r_h} \right] \hat{\phi} \quad (3.5)$$

In the limit as  $r \rightarrow \infty$ , the above field equations are simplified to represent the radiated far field of the element.

$$E^{radiated}(r, t) = \frac{\mu_0 c \sin(\theta)}{4\pi r (1 - \cos(\theta))} \left[ I_s(t - \frac{r}{c}) - I_s(t - \frac{r}{c}) - \frac{h}{c} (1 - \cos(\theta)) \right] \hat{\theta} \quad (3.6)$$

$$B^{radiated}(r, t) = \frac{1}{c} \hat{r} \times E^{radiated}(r, t) \quad (3.7)$$

The source current in the following examples will be represented by a Gaussian pulse of the form

$$I_s(t) = I_0 e^{-t^2/\tau^2} \quad (3.8)$$

where  $\tau$  is the characteristic time. The time it takes for a pulse of charge to travel at the speed of light along the element is  $\tau_a = h/c$ .

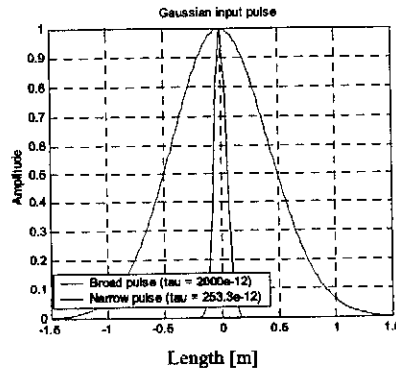


Figure 3.2 : Time trace of narrow and broad Gaussian input pulse as a function of distance in air

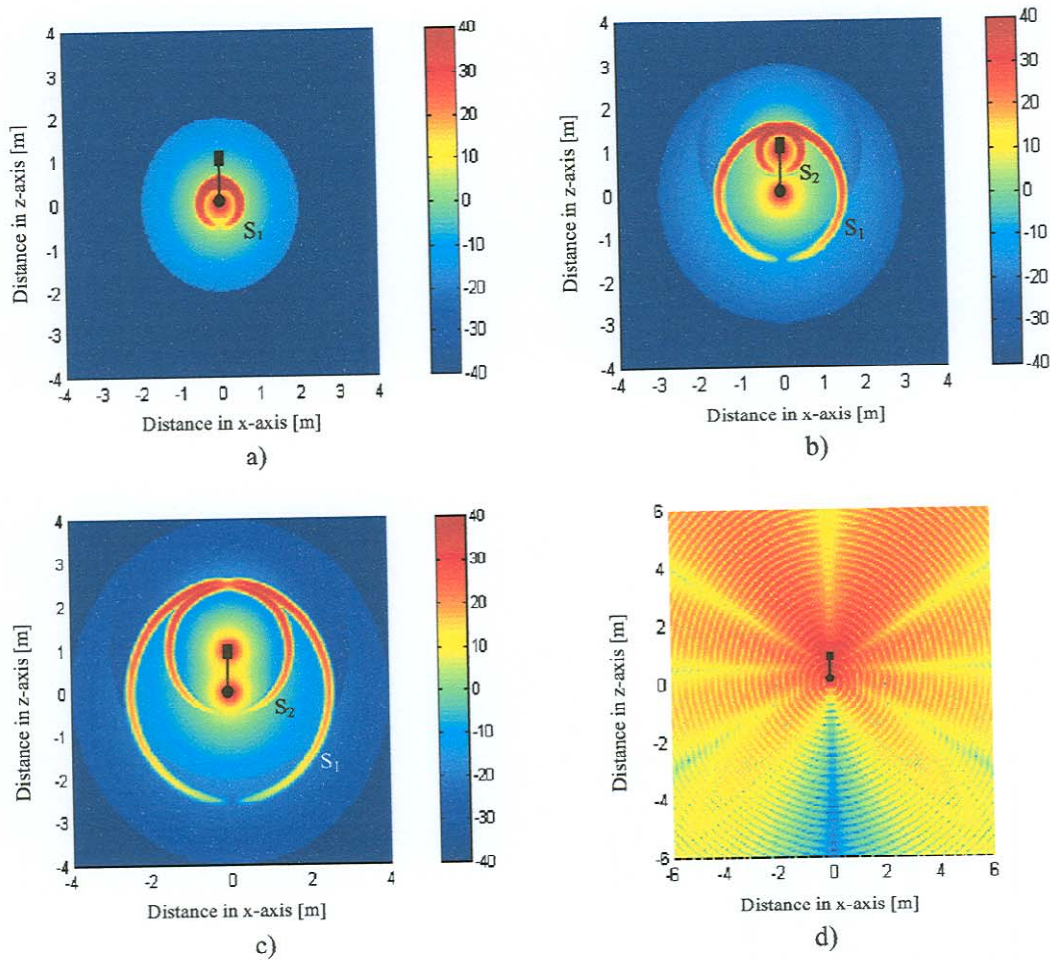


Figure 3.3 : (a)-(c) Magnitude of the electric field surrounding a single travelling wave element at three time “snapshots” ,  $t/\tau_a = 0.5$ ;  $t/\tau_a = 1.5$  and  $t/\tau_a = 2.5$ . (d) Time harmonic representation of the electric field surrounding a single travelling wave element where  $\lambda = 0.5$

For purposes comparison, the length of the element will be taken as 1m in all the examples that follow. The width of the pulse in time will be chosen so that it will be approximately one-fourth of the length ( $\tau/\tau_a = 0.076$ ) of the element. The pulse is electrically small, compared to the travelling wave element.

The behaviour of the element when excited by a broad pulse  $\tau/\tau_a = 0.6$  was also examined. Figure 3.2 represents the time traces of the Gaussian pulses under consideration. Figure 3.3 (a)-(c) shows the logarithm of the magnitude of the electric field  $|E|$  for three “snapshots” in time:  $t/\tau_a = 0.5$ ,  $1.5$ , and  $2.5$ . The electric field at the element is infinity and for purposes of clarity the field is

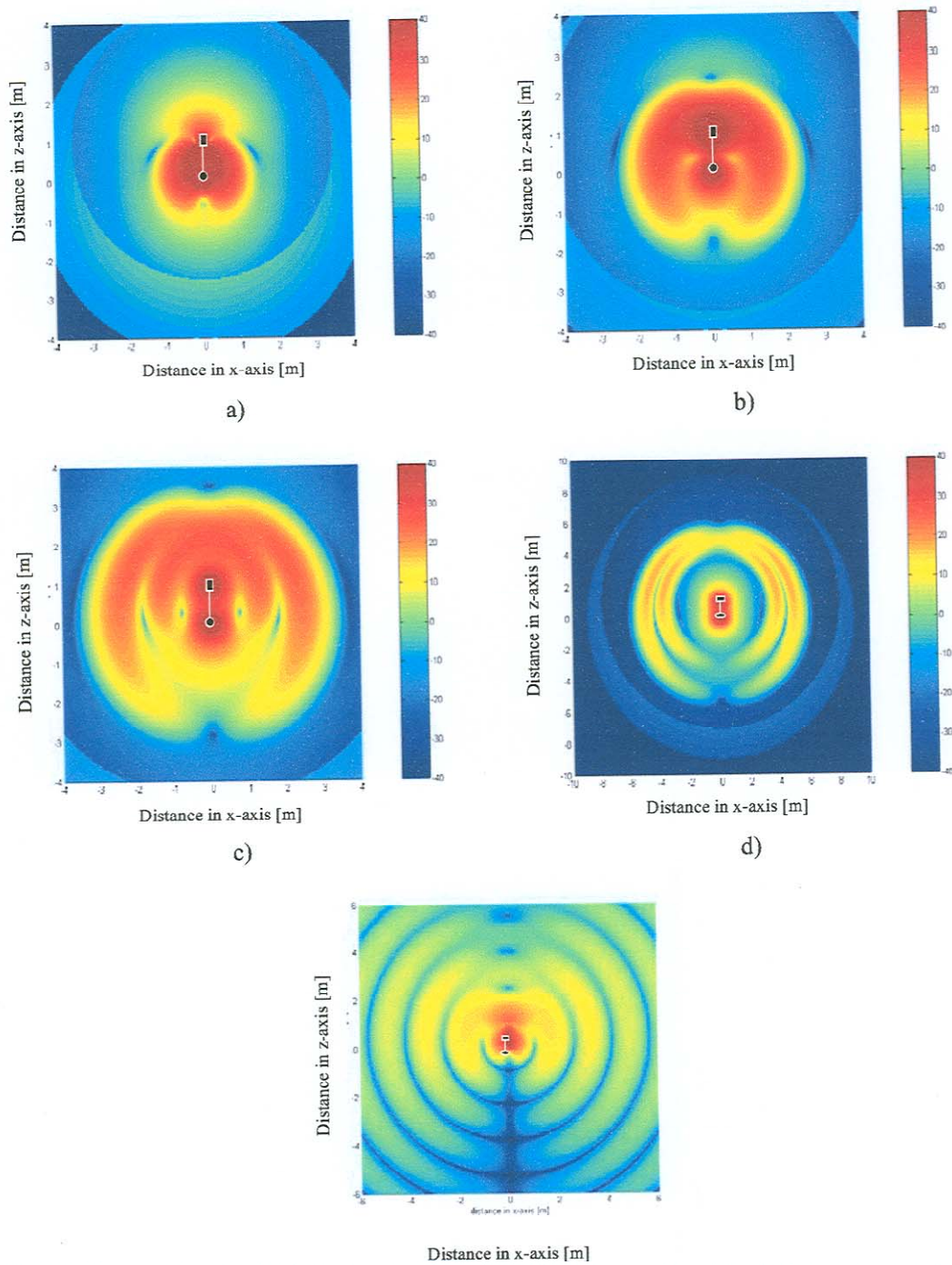


Figure 3.4 : (a)-(d) Magnitude of the electric field surrounding a single travelling wave element at three time “snapshots”,  $t/\tau_a = 0.5$ ;  $t/\tau_a = 1.5$ ,  $t/\tau_a = 2.5$  and  $t/\tau_a = 5$ . (d) Time-harmonic representation of the electric field surrounding a single travelling wave element where  $\lambda = 3\text{m}$

clipped between  $-40$  and  $40$  dB. The radiation characteristics over time can be described by two spherical wave fronts. Initially, a wave front  $S_1$  is produced with the origin located at the source ( $z = 0$ ). A second wave front  $S_2$  ( $z = h$ ) that is retarded in time by  $h/c$  is produced at the termination as the travelling charge leaves the element. The two wave fronts travel outward radially at the speed of light. The concentration of the electric field around the element after the pulse has left the element is due to the accumulation of the negative charge at the source and positive charge at the termination. As previously stated, these charge deposits enforce the neutrality of the element and gives rise to a static electric field. Notice that the static field has no  $1/r^3$  component associated with a displaced positive and negative charge in space when the current excitation in equation ( 3.6 ) is substituted with a time harmonic current of the form

$$I_s(t) = \text{Re}(I_s e^{j\omega t}) \quad (3.9)$$

with the phasor,

$$I_s = -\frac{j e^{jk_o h} I_o}{2 \sin(k_o h)} \quad (3.10)$$

The electric field can be examined as a function of frequency. Figure 3.3 (d) shows the time harmonic excitation of the travelling wave element. For this case  $\lambda_o = 0.5\text{m}$  is chosen so that four half-cycles of a cosine harmonic can fit along the length of the element.

The time-harmonic representation clearly shows radial lines at different angles of theta at which the magnitude of the electric field is at a maximum or minimum. The element can be seen as an array consisting of two sources with a phase delay of  $h/c$  relative to one another. Destructive and constructive interference between the wave fronts  $S_1$  and  $S_2$  cause the radial lines of maximums and minima in the field. Figure 3.4 (a)-(d) shows the magnitude of the electric field  $|E|$  for four “snapshots” in time:  $t/\tau_d = 0.5, 1.5, 2.5$  and  $5$ .

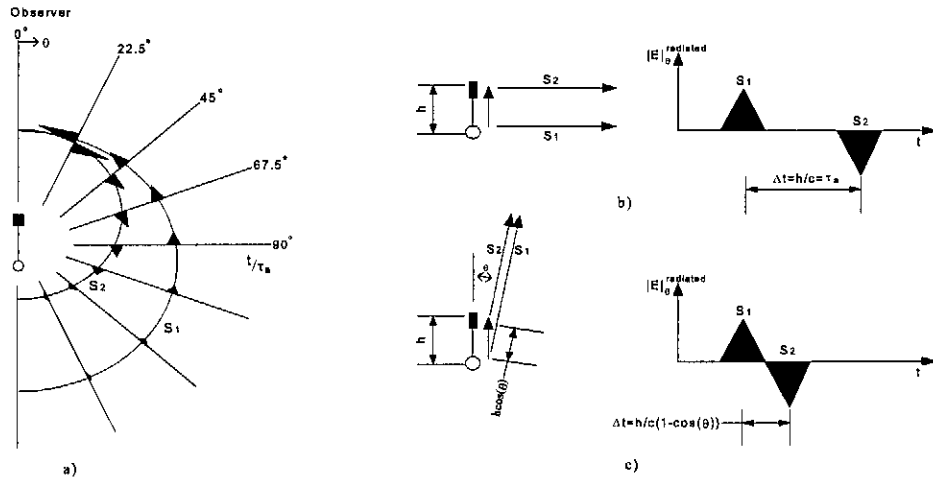


Figure 3.5 : (a) Far-zone electric field of the travelling wave element excited by an electrically small pulse, (b) and (c) describe the time difference between the source and termination wave fronts at various positions in space [11]

For this case the travelling wave element appears electrically small compared to the width of the pulse. The pulse cannot be distinguished from the early time “snapshots”. The magnitude of the electric field seems to decrease as the physical element becomes small compared to the pulse duration. Figure 3.4 (e) gives the time harmonic representation with  $\lambda_0 = 3$  m. The maximum and minimum radial lines of the electric field seem to decrease.

To explain the phenomena, the time separation between the wave fronts  $S_1$  and  $S_2$  at various positions of theta have to be considered. Figure 3.5 (a) represents the theta component of the electric far field, recorded at various angles  $\theta = 0^\circ; 22.5^\circ; 45^\circ \dots$ . Figures 3.5 (b) and (c) explain the time difference between the wave fronts as seen by an observer situated firstly at broadside ( $\theta = 90^\circ$ ) and then at various angles of theta. At first sight it seems as if the observer will see a shift in the frequency content at small angles of theta. The pulse is deformed to represent a narrow monocycle. If this is true distortion in the time-harmonic representation in Figure 3.4 (e), varying theta will be visible. At  $\theta = 0^\circ$  the time difference between the two wave fronts is zero, causing the null in the electric field due to destructive interference.

Each pulse contains the same frequency spectrum. As previously stated, the pulse propagates without attenuation or distortion along the element. The magnitude of the different frequencies

describing the pulse generated at the source and at the termination will thus be the same. The frequency components of the pulse generated at the termination is  $180^\circ$  out of phase with the source pulse. If there is no phase variation between the pulses at a specific point in space, they will cancel. At small angles of theta the phase contents add destructively and cancels, and the low frequency components will be affected more severely than the high frequency components. The relative phase variation between the low frequency components is less than for the high frequency components. To the observer it seems as if the pulse has been passed through a high pass filter. The electric field can be represented by the derivative of the current.

### 3.2.2 Constructing a dipole antenna using travelling wave elements

The electromagnetic field of the dipole antenna is the superposition of the electromagnetic fields of the four travelling wave elements:

$$\begin{aligned} E(r, t) &= \sum_{i=1}^4 E_i(r, t), \\ B(r, t) &= \sum_{i=1}^4 B_i(r, t) \end{aligned} \quad (3.11)$$

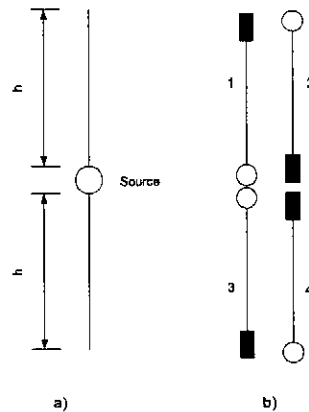


Figure 3.6 : (a) Standing wave dipole, (b) represented by four travelling wave elements

From Figure 3.6 a pulse of positive charge propagates along element 1. At the same time a pulse of negative charge propagates along element 3, to keep the plane of electric symmetry at the source normal to the dipole arms. The two pulses enter the terminations at  $t = h/c$  and are totally reflected. The reflected pulses continue to propagate along elements 2 and 4, and at  $t = 2h/c$  they

are absorbed at the source of the dipole. The four elements describe only one return path propagation of the pulse along the dipole. In reality the pulse can reflect from the source again until fully attenuated along the line.

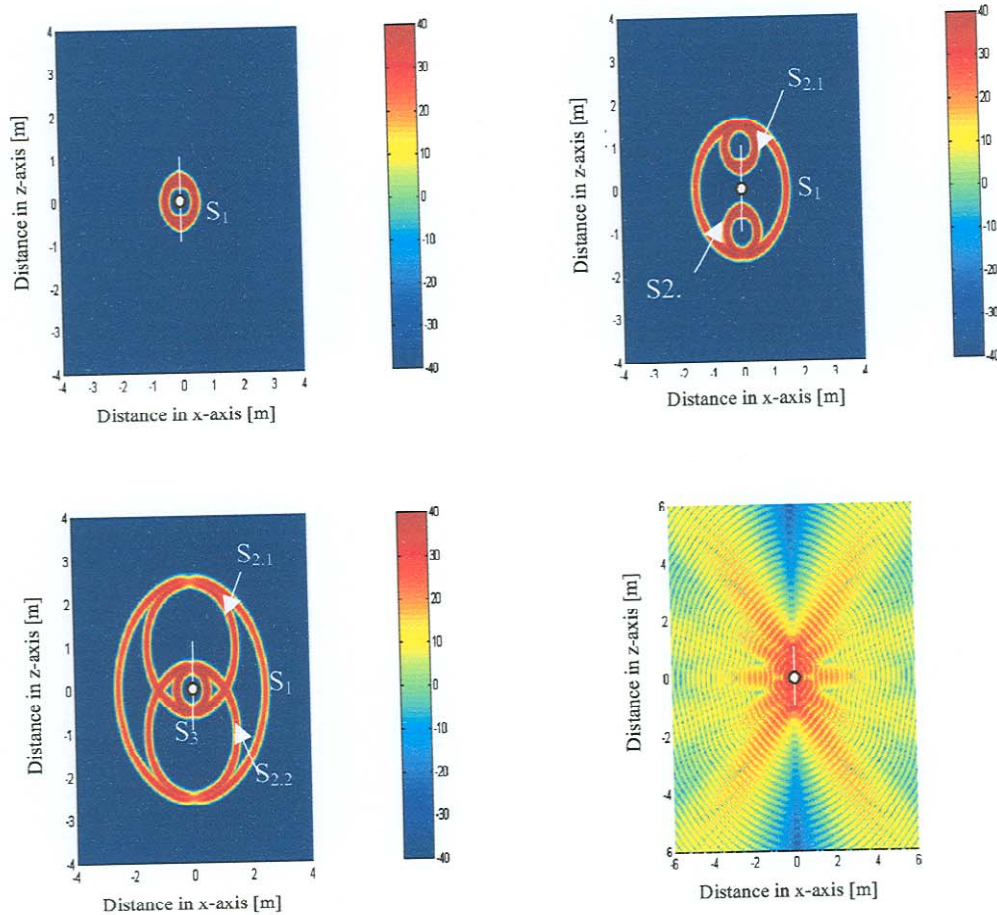


Figure 3.7 : (a)-(c) Magnitude of the electric field surrounding a standing wave dipole antenna at three time “snapshots” ,  $t/\tau_a = 0.5$ ;  $t/\tau_a = 1.5$  and  $t/\tau_a = 2.5$ . (d) Time harmonic representation of the electric field where  $\lambda = 0.5\text{m}$

Figure 3.7 describes four spherical wave fronts. These pulses are generated whenever the pulses of charge/current encounter the source or the open ends (terminations) of the dipole:  $S_1$  is centered at  $z = 0$  when the pulse leaves the source;  $S_{2,1}$  is centered at  $z = h_1$  and  $S_{2,2}$  is centered at  $z = h_2$ .  $S_3$  is centered at  $z = 0$  after a time of  $2h/c$  has passed and represents the second source radiation.

### 3.2.3 Comparing radiation results of a dipole constructed of travelling wave elements and a full FD-TD solution

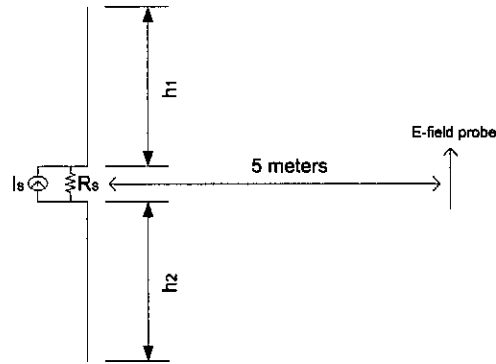


Figure 3.8 : Schematic of the geometrical setup of the dipole with electric field probe

In the previous section on the travelling element dipole, only the radiation aspects of the antenna were considered, and the input impedance limiting the input power was not addressed. Secondary current behaviour on the dipole arm was assumed to consist only of a total reflection at the ends of the dipole arms with no attenuation.

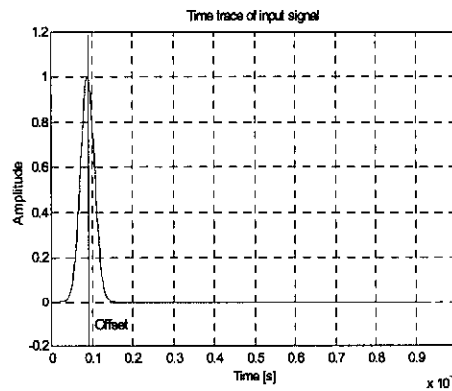


Figure 3.9 : Real Gaussian input signal of current source

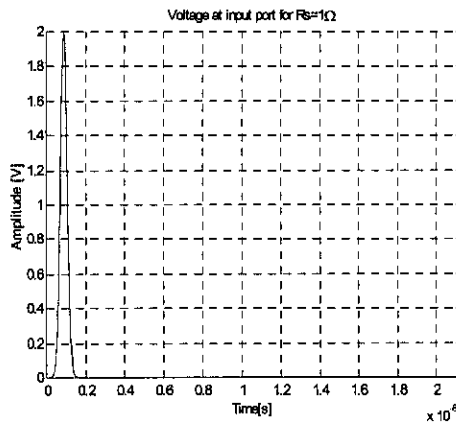


Figure 3.10 : Voltage at input terminal for a source impedance of  $1 \Omega$

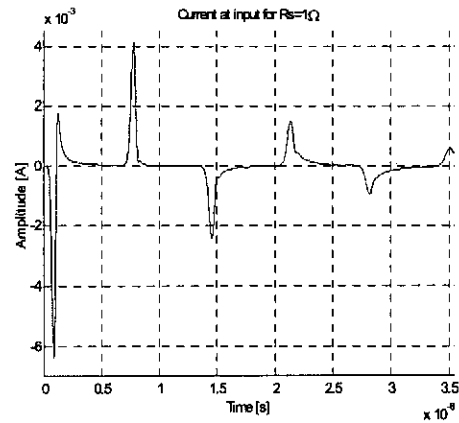


Figure 3.11 : Current at input terminal for a source impedance of  $1 \Omega$

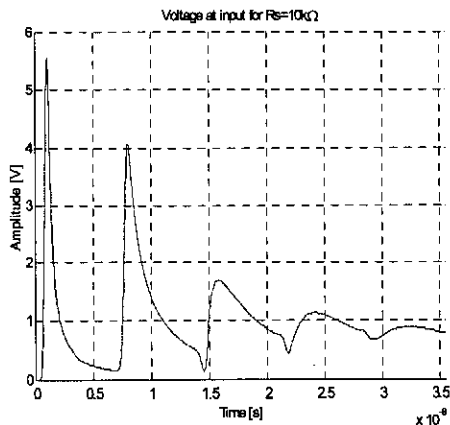


Figure 3.12 : Voltage at input for a source impedance of  $10 \text{ k}\Omega$

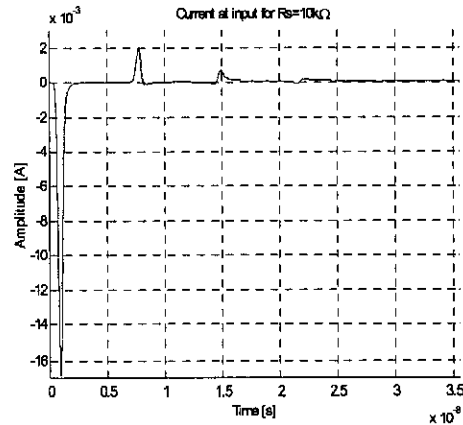


Figure 3.13 : Current at input for a source impedance of  $10 \text{ k}\Omega$

The assumption that radiation only occurs at the source and the open ends of the travelling wave dipole should be verified to justify whether the approximation holds true. Figure 3.8 shows the simulated setup used for comparison between an *FD-TD* code and results obtained from the simple travelling element dipole.

The excitation of the *FD-TD* code consists of a discrete port that represents a current source with a parallel source resistance. Maximum power transfer between the dipole input impedance and pulse excitation source is not possible (dipole impedance varies considerably over the wide

frequency band). Figure 3.9 shows the excitation signal that consists of an offset of 894 ps and a frequency spectrum from 0–2 GHz. The source was first modelled as a current source by

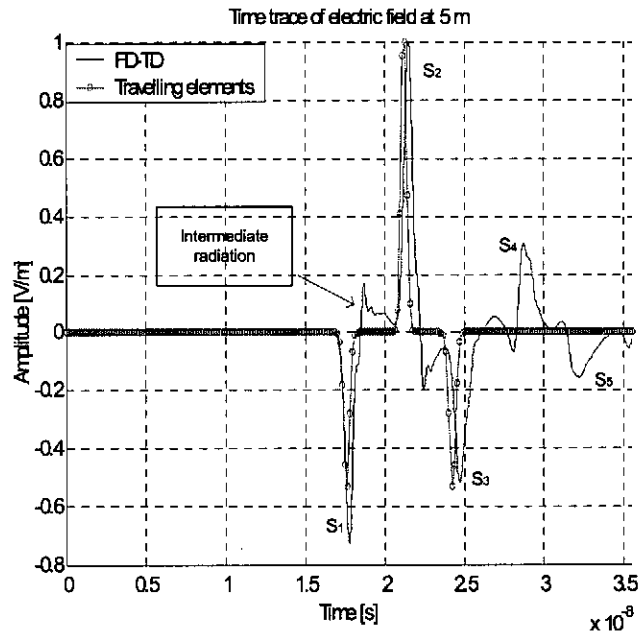


Figure 3.14 : Time trace of the electric field for *FD-TD* and travelling element dipole when excited by an current source

choosing  $R_s = 10 \text{ k}\Omega$  (the input impedance of the antenna is much lower than the source resistance) and secondly as a voltage source with  $R_s = 1 \Omega$  (the input impedance of the antenna is much higher than the source resistance). Figure 3.10-3.13 gives the input voltage and current for a source impedance of  $10 \text{ k}\Omega$  and  $1 \Omega$ . An electric field probe was placed 5 meters away from the dipole, situated at broadside ( $\theta = 90^\circ$ ). Both arms ( $h_1$  and  $h_2$ ) are 1 meter long.

The wave fronts  $S_1$  (source),  $S_2$  (open end) and  $S_3$  (source) in Figure 3.14 represent the source and end reflections as illustrated in Figure 3.7. Both arms  $h_1$  and  $h_2$  are the same length. The open end wave front  $S_2$  consists of the superpositioning of two wave-fronts at either end of the dipole. The time traces for the travelling element dipole and *FD-TD* simulation in Figures 3.14, 3.15 were amplitude-normalized for purposes of comparison. The arrival times of the source and end reflections correlate well.

These results show that the main contribution to the dipole radiation occurs at the source and open ends. The difference between the amplitude of  $S_1$  and  $S_3$  for the *FD-TD* simulation indicates that the current pulse attenuates along the line. There are no ohmic losses along the line because the dipole arms were simulated as perfect electric conductors. If there is attenuation along the line, the amplitude of  $S_2$  can only be described as the superpositioning of the wave fronts originating from the end reflections, because the amplitude rises above the first source reflection. Peaks  $S_4$  and  $S_5$  show that the antenna continues to “ring” until the current pulse is fully attenuated. The travelling element dipole only represents one round trip from source to end and back. In reality this phenomena can continue for some time until all the energy is dissipated on the line.

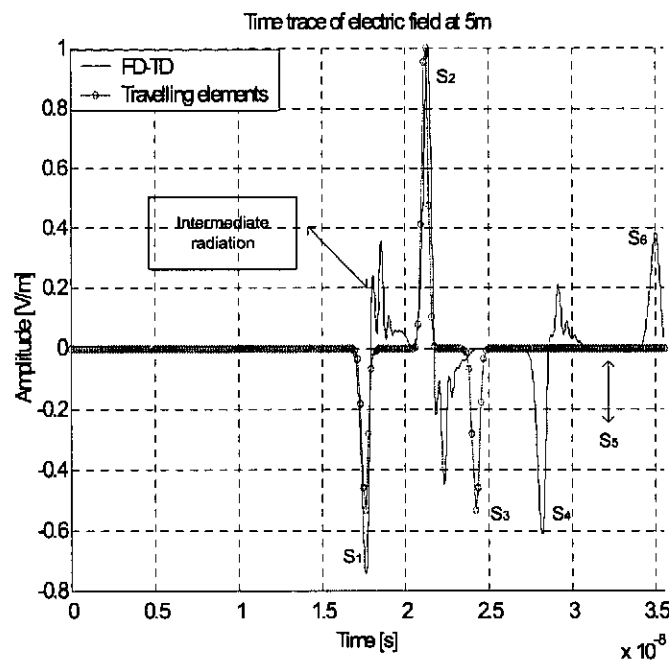


Figure 3.15 : Time trace of the electric field for FDTD and travelling element dipole when excited by an voltage source

From the input port current it is clear that the polarity of the dipole arms does not change for a current source. The deformed section of the electric field following each pulse will be assigned to intermediate radiation [12] as the pulse moves along the line. The radiation from a voltage source

shown in Figure 3.15 is surprisingly different from the radiation from a current source excited dipole.  $S_1$  and  $S_2$ , represents the radiation occurring at the source just after excitation and from the end point.  $S_3$  and  $S_4$  which represent wave fronts generated at  $z = 0$  retarded in time, are non-existent for the voltage source excitation. The travelling element dipole case coincides with dipole radiation excited by a current source. The excitation definition of a travelling wave element makes it clear that a current pulse was used. The dipole excitation can be approximately described as a pulse of positive charge moving along the one arm and a pulse of negative charge along the opposite arm. For a current source excitation, the source resistance is high, which causes the charge to move up and down the arm with an apparent open circuit at both the open end and source end.

The analogy drawn from the travelling wave element is that the charge causes radiation due to the reflection and associated acceleration it undergoes at each end. The radiation wave-front  $S_4$  results from this reflection at the open ends. If there is no reflection at the source at time  $2h/c$  it suggests that the pulses change arms due to the short circuit at the feed point. The polarity change in the current at the input port shows that the dipole arm currents change charge polarity at the source as expected from a low source impedance. This explains the change in polarity of the second ( $S_4$ ) end reflection. Because there is no radiation from the low impedance source point after excitation, less power is dissipated through radiation over time. The wave front  $S_6$  is not visible for the current source. Voltage source excitation causes the antenna to ring longer, due to the diminished radiation. More spikes are visible in the intermediate section.

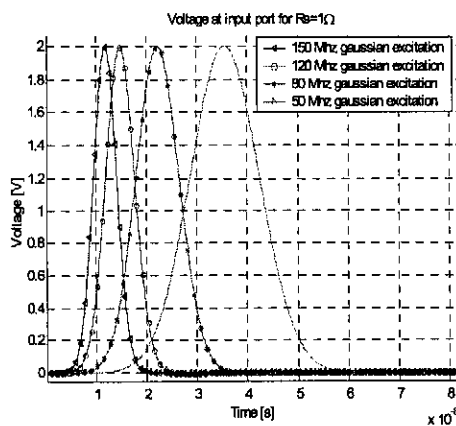


Figure 3.16 : Gaussian input voltage with different frequency contents for  $R_s = 1 \Omega$

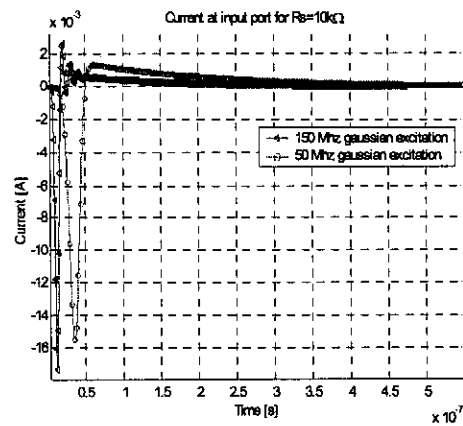


Figure 3.17 : Gaussian input current with different frequency contents for  $R_s = 10 \text{ k}\Omega$

Figures 3.18-3.21 represent the electric field and its *Discrete Fourier Transform* for the Gaussian pulses of Figures 3.16, 3.17, with different frequency contents. The same dipole length as before was used and the electric field was probed at 10 meters broadside from the dipole. The transient traces resemble signals with finite energy over a certain period of time with a low frequency content, to introduce the transient properties of electrically small antennas resembling the borehole antennas. *Appendix B3* gives the number of samples and repetition period that was used throughout this investigation. *Appendix B3* also explains the deficiency of the energy density spectrum and the difficulty of establishing real signal levels by investigating only the frequency domain of transients. Figure 3.19 shows the *Discrete Fourier Transform* of both the electric field trace and the voltage at the excitation port ( $R_s = 1 \Omega$ ). The difference between the excitation magnitude and the electric field trace resembles a transfer function between the input voltage and electric field. This was done so that the frequency information can be related to the time dependent traces, which is not possible if only the spectrum of the coupling is investigated. The *Discrete Fourier Transform* of the electric field incorporates the transfer function of the system. The transfer function for a current source ( $R_s = 10 \text{ k}\Omega$ ) was established between the current and the electric field.

The input pulses have a frequency content of maximum 150 MHz and the resonant frequency of the dipole is around 75 MHz. The tail of the electric field transients of the voltage source all have the same period except for the 0-50 MHz pulse excitation. The magnitude displays a peak that will be called the natural frequency and is directly related to the period of the time trace. For the

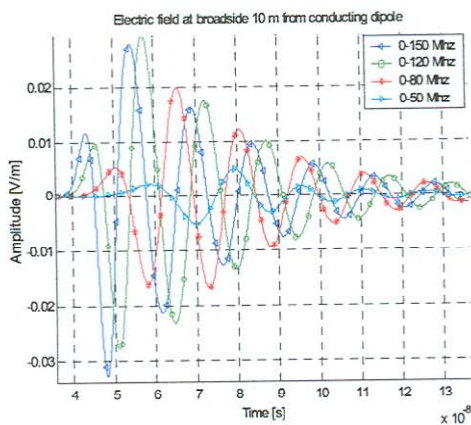


Figure 3.18 : Electric field for different Gaussian pulse widths - voltage source

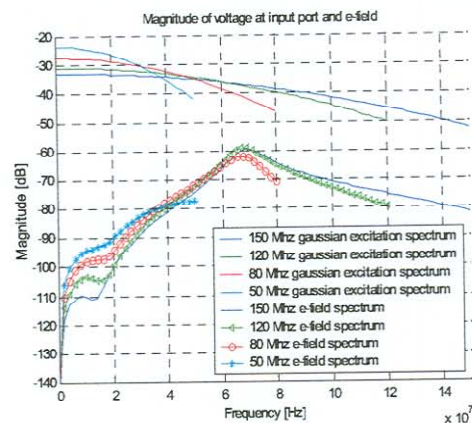


Figure 3.19 : Magnitude of electric field of different Gaussian pulse widths - voltage source

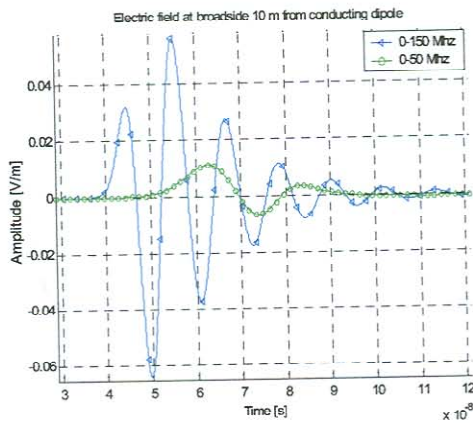


Figure 3.20 : Electric field for different Gaussian pulse widths - current source

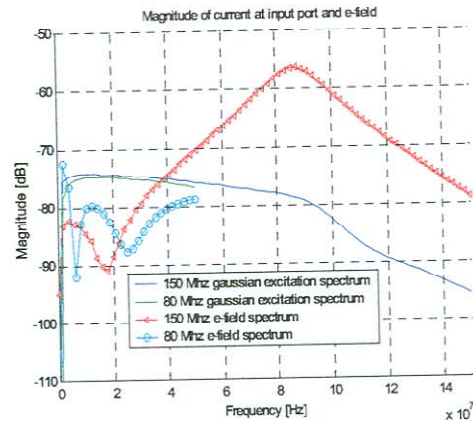


Figure 3.21 : Magnitude of electric field of different Gaussian pulse widths - current source

0-50 MHz, pulse the period relates to the maximum frequency input. The natural frequency stays the same (pulses with frequency content above the natural frequency) and the only observable difference in the time trace for higher frequency pulse is the rise time and amplitude of the first absolute peak values of the transients. Thus the start section and peak edges indicate the amount of high frequency information. The natural frequency differs for the current source and voltage source excitations. This difference can be attributed to the different mechanisms of radiation

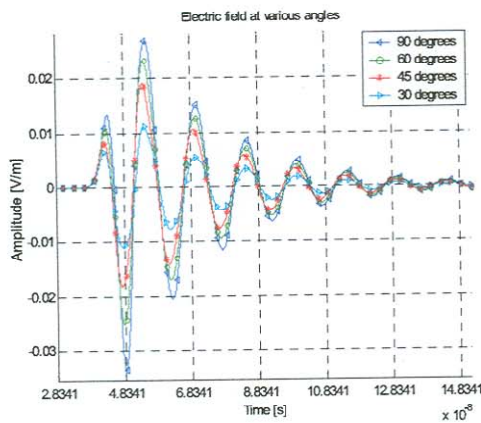


Figure 3.22 : Electric field (Theta component) at various angles for a Gaussian pulse with a frequency content of 0-150 MHz

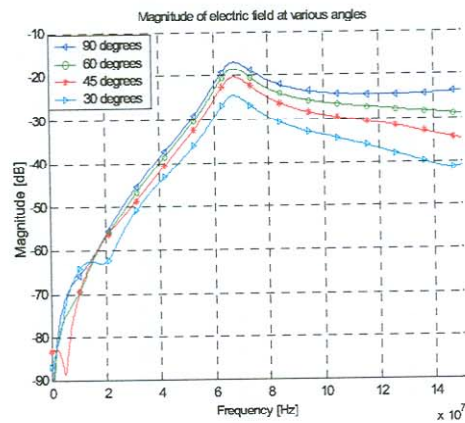


Figure 3.23 : Magnitude of the coupling of the electric field (Theta component) at various angles for a Gaussian pulse with a frequency content of 0-150 MHz

concerning the two configurations. As for the 0-2 GHz pulses, the voltage source only radiates once at the source during excitation and only at the dipole arm ends making the time difference between the transmitted pulses longer for the tail (of the transient) section than for the current source. The natural frequency can thus be related to the radiation mechanism and structure length. It is very difficult to determine the influence of the intermediate radiation for electrically small structures because the transmitted pulse appears as a superposition of multiple radiated pulses.

The natural frequency stays the same for the time varying electric field (Figures 3.20, 3.21) at various positions from the dipole  $\theta = 30^\circ, 45^\circ, 60^\circ,$  and  $90^\circ$  due to the small phase variation of the theta angles on the low frequency pulses. The magnitude of the electric field trace shows that there is a degradation of the higher frequencies for small values of theta where the phase variation would be more severe. The peaks in the time trace become attenuated as well as broader as an indication of the reduction in high frequency information. The broadening of the pulse peak widths thus is also an indication of the high frequency content in the trace while the natural frequency dominates the period.

### **3.3 Charge behaviour on a dipole radiator**

In the previous sections, an analogy was drawn between the radiation from an antenna excited by a pulse of current, and the radiation from a moving point charge. The discussion that follows is a case study of contemporary views on the radiation of a dipole antenna. These views will help with the understanding of resistively loaded antennas.

Where radiation arises from a straight thin-wire antenna has been a source of controversial discussion in the electromagnetic community and whether it is possible to understand or establish the origin of radiation on a thin-wire dipole remains debatable. However, some interpretation needs to be developed to fully understand the wide band characteristics of a resistively loaded dipole primary used for pulsed radar applications.

### 3.3.1 Examination of electromagnetic radiation

E. K. Miller [12] presented three perspectives of electromagnetic radiation, which consisted of the electric field kink model, FARS (Far-field Analysis of Radiation Sources) and TWTD (Thin-Wire Time Domain) model. Only the kink model will be discussed as this model demonstrates that the propagation speed of electromagnetic fields is finite, electric field lines in a source-free region are continuous, and radiation occurs as a result of a charge acceleration, or a “kink” in the electric-field lines of a charge. The kink model reveals radiation characteristics of a moving charge, but does not apply to the boundary conditions applicable to a perfect electrical conductor (PEC). Charges in a real material medium cannot move at light speed. The radiation field for a center-fed dipole remains in contact with the antenna until its radiation sphere expands to the dipole ends. This means that the charges move at the speed of light along the dipole’s length, because the electric field must terminate normally at the dipole’s surface.

Miller related the charge speed to an interaction between charges that occur in the same manner as the interaction of a row of falling dominoes. Deceleration of charge along the dipole arm cannot be the cause of radiation in a uniform dielectric. In fact it was shown that, except for radiation contributions from the source and ends of a dipole, some intermediate radiation also occurs along the length of the wire. Since the speed of the charge matches that of the external fields, the only acceleration of charge along the wire occurs due to reflections along the wire. The reflections can possibly be attributed to the varying characteristic wave impedance along the line.

S. A. Schelkunoff [13] commented that whether the radiation resistance is considered as continuously distributed along the wire or seen as a output impedance (transmission line model) has little effect on the current distribution, for electrically small antennas. In the case of the borehole radar antenna, the only meaningful intermediate radiation will be caused by the gradual change in characteristic impedance as the charge moves away from the source. When a short pulse transition on a dipole antenna is considered, the intermediate radiation will be more severe. Multiple modes can exist on the dipole and the wave impedance will change for each mode along the length of the antenna for a specific frequency and cause reflection.

### 3.3.2 Extracting time-dependent charge behaviour on a dipole antenna

CST™ offers a time-dependent, thin-wire electric field integral equation that was used to examine the electromagnetic phenomena, including the physics of radiation, connected with a simple wire antenna. This is an old problem that is being revisited here to shed some light on charge behaviour concerned with non-uniform lines. The magnetic and electric fields are probed close to the wire and the associated charge and current behaviour will be inferred from these.

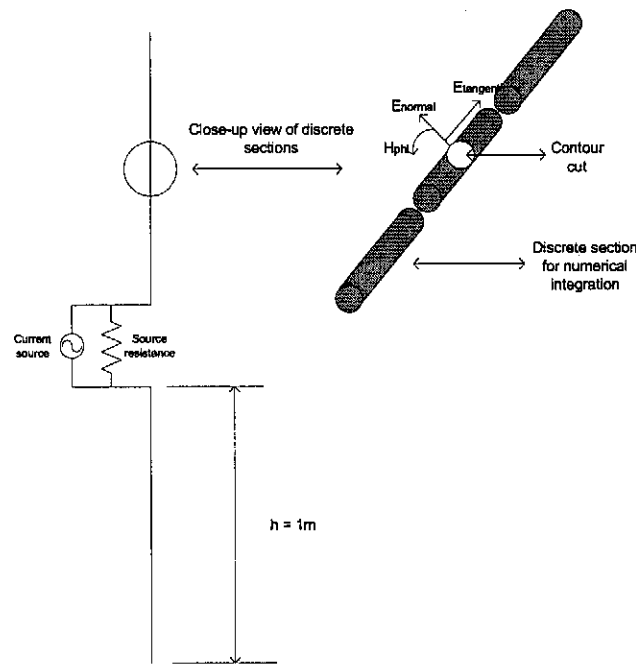


Figure 3.24 : Discrete dipole used for extracting charge density

The charge density on the dipole can be extracted by implementing Gauss' integral law,

$$\oint_S \epsilon_0 \vec{E} \cdot d\vec{a} = \int_V \rho dv \quad (3.12)$$

on the normal electric field on the surface of the wire. The conductor will be modelled as a perfect electric conductor and cannot have any tangential electric field component that will be associated with conduction losses. The integral will be obtained by dividing the wire into discrete

elements as shown in Figure 3.24. The current density can be extracted by using Ampere's integral law,

$$\oint_C \vec{H} \cdot d\vec{s} = \int_S \vec{J} \cdot d\vec{a} + \frac{d}{dt} \int_S \epsilon_0 \vec{E} \cdot d\vec{a} \quad (3.13)$$

In this example, the antenna is excited with a Gaussian impulse with a frequency content of 0-2 GHz. The source resistance is  $1 \Omega$  to resemble a voltage source. The conducting dipole is situated in air and has a total length of 2m. The antenna is symmetric and the feeding point is situated at point A (Figures 3.25 and 3.26 show the normalized charge density as a function of position and time along one arm of a differentially excited dipole.). The finite energy pulse propagates along the wire at the speed of light, set by the ambient electrical properties in which the electric field propagates. At the dipole end (point B) the pulse encounters an open circuit and reflects. Some energy clearly radiates at this point, due to the charge reflection and propagation reversal.

A slight decline of charge is visible when the pulse propagates along the wire. As there are no conduction losses, the only explanation for the phenomenon is that some energy radiates along the length of the wire, as mentioned by E. K. Miller.

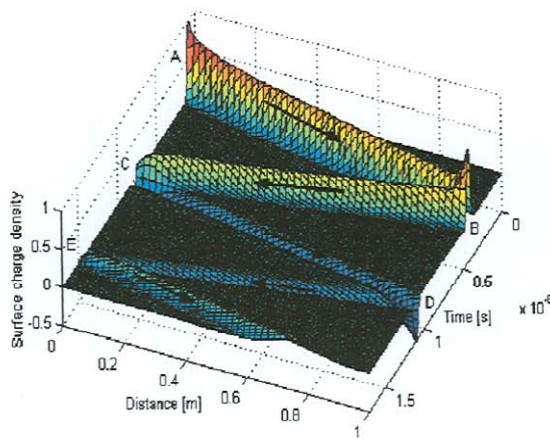


Figure 3.25 : Normalized charge density of dipole antenna in air

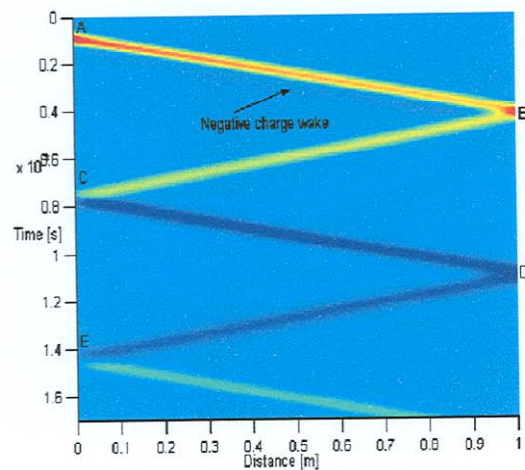


Figure 3.26 : Top view of charge spread as a function of time and distance of dipole in air

At point C, a charge minimum is visible. The voltage source causes a low impedance point and charge reversal takes place where the negative charge and positive charge pulses change dipole arms. The negative charge pulse continues with the same behaviour along the wire until it reflects at point D. This process repeats itself until all transients have decayed. Figure 3.26 shows that a negative charge wake follows the positive charge. This charge trail is due to charge extraction from the source during excitation, if the reasoning presented by E. K. Miller is followed. It could also be due to initial reflections occurring during excitation from the negative charge pulse.

Figures 3.27 and 3.28 present the charge behaviour for the same dipole insulated with polyurethane (radius = 16.5mm) and air (radius = 25.5mm) with an ambient dielectric constant of 7 to simulate the borehole environment. The same excitation condition was used as for the dipole in air, and again point A presents the excitation point and B the end of the wire. Figure 3.27 clearly shows a double positive charge ripple in time at the same position along the wire. A narrow Gaussian input pulse was used to improve the resolution of charge to make this visible. The ripple is due to reflections between the air and ambient interface. The energy in the pulse decays to nearly zero after one round trip from source to end.

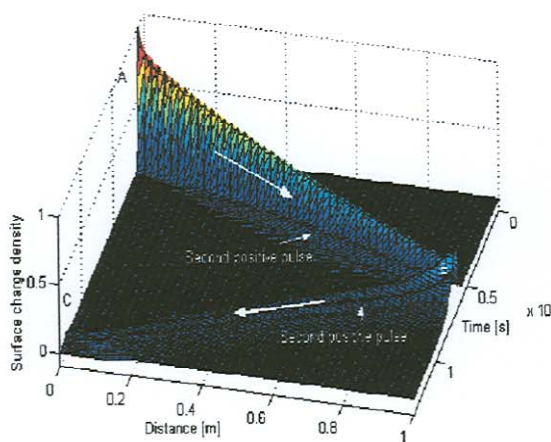


Figure 3.27 : Normalized charge density of dipole antenna in a borehole

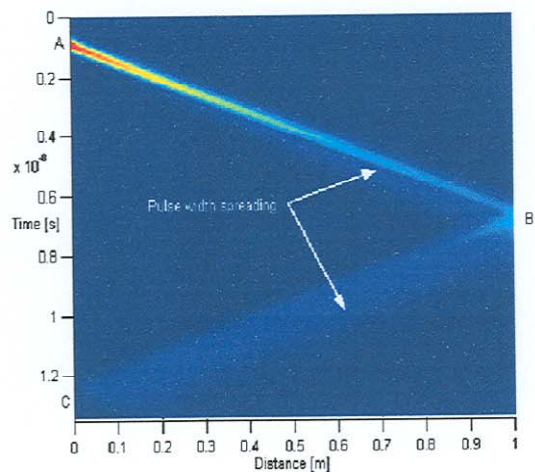


Figure 3.28 : Top view of charge spread as a function of time and distance of dipole in a borehole

The charge pulse moves faster along the wire than the propagation speed associated with an ambient rock dielectric of 7. The pulse should take 8.8ns to propagate a distance of 1m but only takes 6ns representing an effective permittivity of 3.6. This dielectric constant resembles the

value obtained for the combined mathematical value representing the insulation and air in the next chapter. The broadening of the pulse in Figure 3.28 can be due to reverberation of the electric field in the hole and due to reduction of energy in the high frequency components along the wire from intermediate radiation. The high frequency content of the pulse also gives rise to different modes and mode velocities, since the insulated hole forms an electric guide.

### **3.4 Conclusion**

A rigorous approach was taken to establish the main contributions of dipole radiation. From the time-dependent excitation it is clear that dipole radiation occurs at the sections of the dipole where charge acceleration takes place, i.e. source and ends. Some radiation probably takes place along the wire, due to varying wave impedances caused by the non-uniformity of the conductor, to form a wire radiator. For broad pulse excitation (antenna is electrically small compared to the frequency content of the excitation pulse), it is difficult to establish the contribution from the intermediate radiation due to the ringing behaviour of the dipole. Efficient pulse radiation will take place when the pulse width fits along the wire so that the end and source radiated pulses do not add destructively. This explains why dipole arms are bent in opposite directions to produce the maximum phase shift. Broadband antennas cannot be analysed by only gathering frequency domain information, because this may contain the magnitude of energy transfer but says nothing about the time during which the transfer has taken place. For electrically small antennas it will also be difficult to tell whether dispersion of the pulse has taken place by investigation of the phase of the transfer function.

It is outside the scope of this work to extract the charge density for a Wu-King resistively loaded antenna due to the difficulty of constructing a continuous resistive profile, which is necessary for the excitation used. This means that the intermediate radiation could not be investigated, as a result of the limitations of the *FD-TD* code. The code makes provision for limited conductivity materials but accurate results can only be assured with an impractically fine meshing and the correct resistive profile cannot be obtained in this manner.

## Chapter 4

# ***THEORETICAL AND NUMERICAL MODELLING OF INSULATED ANTENNAS***

### **4.1 Introduction**

The importance of understanding antennas placed in matter becomes apparent when one considers the rising need for using probes as diagnostic and communicational tools in an underground environment. Unfortunately the accurate formulation and solution of antenna theory for the simplest bare thin-wire dipole is surprisingly complicated, even when it is in air, and even more difficult when it is embedded in a dissipative or dielectric medium. This chapter concentrates on implementing a simple model (*Transmission Line Model*) to investigate insulated antennas.

Section 4.2 introduces the theoretical impedance model applied to insulated wire antennas and discusses the transmission line parameters governing the model. The versatility of the model is shown in Section 4.3, as it can be used to model both symmetrical and asymmetrical conducting and resistive wire antennas. Finally the *TLM* was compared with results obtained from a commercial electromagnetic simulation tool (*FEKO<sub>m</sub>*). Section 4.4 verifies whether it is possible to represent the insulated antenna with an equivalent antenna in a dielectric medium. The main reason for investigating the *TLM* was to determine whether the resistive profile should be adjusted for conductive surrounding mediums. The antenna did not show significant change for low values of conductivity associated with the gold mine environment. Only for impractical high values of conductivity, could a change in input impedance be established.

### **4.2 King and Smith transmission line model ( *TLM* )**

R. W. P. King and G. S. Smith [14] introduced transmission line theory as a simple approximated solution for understanding insulated antennas embedded in relatively dense mediums.

The radiation from an insulated dipole antenna can be apportioned per unit length in a manner closely paralleling losses in a coaxial line due to dissipation in the dielectric of the conductor. However the theory is not applicable to bare dipole antennas in air or embedded in a general

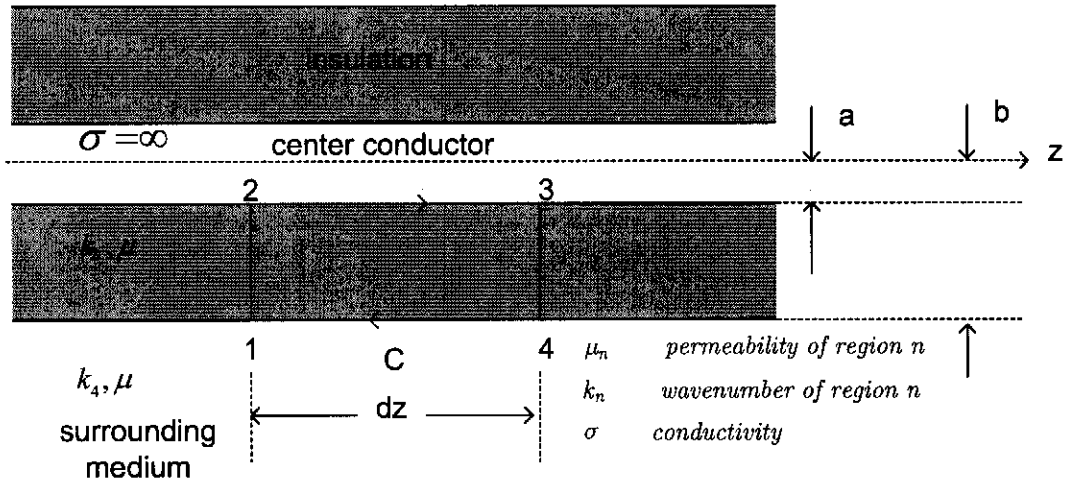


Figure 4.1 : The geometry of an infinite insulated antenna

dissipative mediums. K. C. Chen and L. K. Warnie [15] showed that, under the following conditions  $z \gg b$ ,  $|k_L|b \ll 1$  for  $|k_4| > |k_2|$ , the leading contribution in the insulation is the transmission line field distribution. It is essential to understand the origin of the additional parameters added to the known transmission line model and it is therefore advisable to proceed by deriving the simple formula as follows:

Deriving the quasistatic approximate solution, by invoking Faraday's law as:

$$\oint_C \vec{E} \cdot d\vec{s} = i\omega \int_S \vec{B} \cdot d\vec{a} \quad (4.1)$$

Integrating along path  $C$  in Figure 4.1 will yield the following:

$$\left[ \int_1^2 + \int_2^3 + \int_3^4 + \int_4^1 \right] \vec{E} \cdot d\vec{s} = i\omega \int_S \vec{B} \cdot d\vec{a} \quad (4.2)$$

When a  $TEM$  field distribution is assumed for  $a \leq \rho \leq b$ , it is possible to present equation (4.2) as:

$$\left[ \frac{d}{dz} \frac{q}{C} + E_z^{in} + E_{out} \right] dz = i\omega LI(z) dz \quad (4.3)$$

where  $C = \frac{2\pi\epsilon_2}{\ln\frac{b}{a}}$  and  $L = \frac{\mu_2 \ln\frac{b}{a}}{2\pi}$  represent the capacitance and inductance per unit length of the insulation.

For transmitting antennas,

$$E_z^{in} = -V\delta(z) \quad (4.4)$$

represents the excitation of the antenna.

The outgoing condition in the ambient medium gives

$$E_{out} = \frac{\omega\mu_4\xi_4 H_0^{(1)}(b\xi_4)H_\varphi(b,\varsigma)}{ik_4^2 H_1^{(1)}(b\xi_4)} \quad (4.5)$$

where  $\text{Im}(\xi_4) \geq 0$  and  $H_\varphi(b,\varsigma) = \frac{a}{b}H_\varphi(a,\varsigma) = \frac{I(\varsigma)}{2\pi b}$ , and  $I(\varsigma) = I$

$E_{out}$  is directly related to the internal impedance of a tubular outer conductor for which the thickness of the conductor extends to infinity and thus represents the dissipation and radiation of an outward wave in an infinite medium. The properties of the medium are closely related to that of a conductor where the penetration of the outward wave into the medium can be viewed as a skin effect. Under these conditions, the transmission line theory is very accurate and the *TEM* field distribution is a good approximation for electrically thin crosscut sections of low  $a/b$  ratios. The original problem is converted into the solution of an equivalent generalized surface problem on the insulation cylinder.

$$E_z = Z_s H_\varphi \quad (4.6)$$

For a uniform line current which extends from  $-\infty$  to  $+\infty$  along the z-axis a more conventional definition for the impedance can be deduced:

$$E_z = Z^i I = 2\pi b Z^i H_\varphi \quad (4.7)$$

and  $Z^i = \frac{Z_s}{2\pi b}$

Figure 4.2 represents the lumped element model per unit length. The model is familiar to transmission line theory and the lumped elements can be explained as follows (see also Figure 4) :

The general formula for the internal impedance of the solid metal inner conductor with radius  $a$  is

$$Z_1 = \frac{k_1 a J_0(k_1 a)}{\pi a^2 \sigma_1 2J_1(k_1 a)} \quad [\Omega/m] \quad (4.8)$$

where  $\sigma_1$  represents the conductivity of the inner conductor and  $k_1$  is the wave number associated with a good conductor. For simplicity, either a good conductor or good dielectric have been

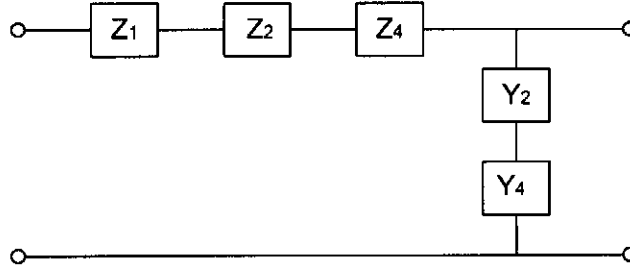


Figure 4.2 : The lumped element model for the insulated antenna based on transmission line theory

assumed for the different regions. The wave number for such regions with a time dependence  $e^{j\omega t}$  can be written as follows:

*Good conductor :*

$$k_c = \beta_c + i\alpha_c = (i\omega\mu\sigma_c)^{1/2} \quad (4.9)$$

*Good dielectric :*

$$k_d = \beta_d + i\alpha_d = \omega(\mu\varepsilon_d)^{1/2}(1 + ip_d)^{1/2} \quad (4.10)$$

where  $p_d = \frac{\sigma_d}{\omega\varepsilon_d} \ll 1$

where  $\varepsilon_c$ ,  $\varepsilon_d$  and  $\sigma_d$  are the effective values of the permittivity and the conductivity. The unit impedance and admittance associated with the insulation region are given by:

$$Z_2 = -i\omega L = -i\omega \frac{\mu_2 \ln \frac{b}{a}}{2\pi} \quad [H/m] \quad (4.11)$$

$$Y_2 = -i\omega C = -i\omega \frac{2\pi\varepsilon_2}{\ln \frac{b}{a}} \quad [F/m] \quad (4.12)$$

where  $\varepsilon_2$  and  $\mu_2$  are the effective permittivity and permeability of the insulation. In order to investigate the individual impedances of the *TLM* in Figure 4.2, the parameters were derived for a conductor radius of  $a = 1.5\text{mm}$  and an insulation radius of  $b = 10.5\text{mm}$ . Figures 4.3 and 4.4 represent the plain parameters associated with a lossless coaxial cable presented by equations (4.11) and (4.12).

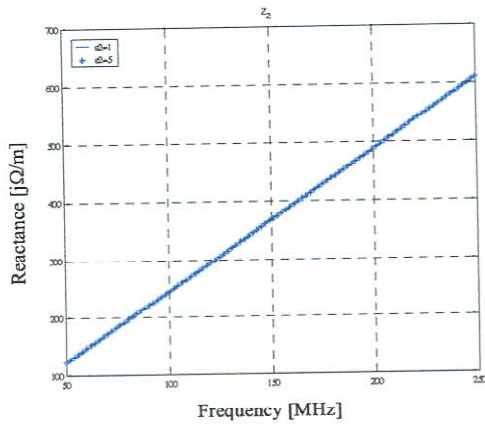


Figure 4.3 : Series reactance per meter for insulated area

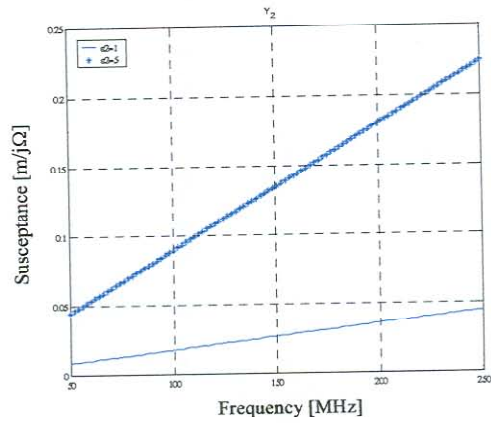


Figure 4.4 : Shunt susceptance per meter for insulated area

The series reactance ( $Z_2$ ) does not change for different dielectric insulations, but will only be affected by a magnetic medium. The shunt susceptance ( $Y_2$ ) shows an increase in capacitance when the insulation's dielectric constant increases. The increase in shunt capacitance increases the equivalent electrical length of the conductor.

The exterior impedance per unit length is given by:

$$Z_4 = \frac{-i\omega\mu_4 H_0^{(2)}(k_4 b)}{2\pi k_4 b H_1^{(2)}(k_4 b)} \tag{4.13}$$

which includes dissipation and radiation. The internal impedance associated with a tubular outer conductor is related to Bessel and Hankel functions of the first kind.

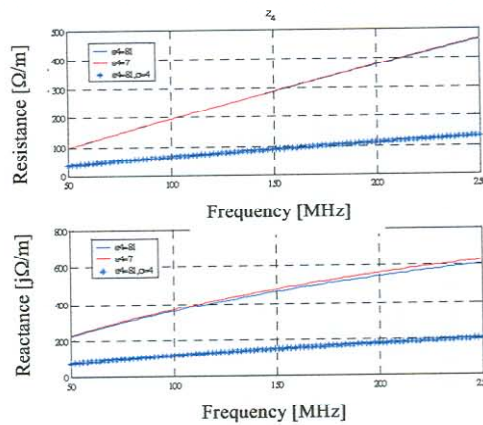


Figure 4.5 : Radiation term

To satisfy the outward wave, Hankel functions of the second kind were used. There are no predominant differences in  $Z_4$  (Figure 4.5) for ambient permittivities of 7 and 81 but it changes considerably for a conductive ambient medium of  $\sigma=4$ . The resistive part represents the radiation resistance.

The little difference between the dielectric constants 7 and 81 indicates that the coupling of the antenna into the ambient region is not affected by differences in dielectric constant. This is non-physical, as one would expect the antenna to couple differently into exterior mediums of different dielectric constants. The radiation condition governing the model is thus incomplete, which makes the model only applicable to ambient mediums with high dielectric constants, e.g. sea water. For low frequencies, small radius insulations will cause little interface reflection and the radiation characteristics of the antenna can be expected to change.

The exterior admittance was introduced by K. C. Chen and L. K. Warne [15] after examining the current model. Before explaining the function of  $Y_4$ , the wave number and characteristic impedance for the unit section described thus far is given by:

*Wave number :*

$$k_L = [-(Z_1 + Z_2 + Z_4)Y_2]^{\frac{1}{2}} \quad (4.14)$$

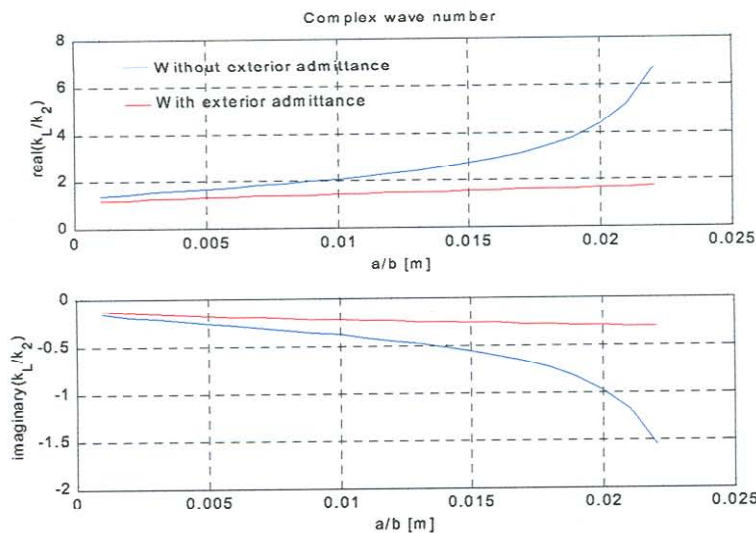


Figure 4.6 : Normalized complex wave number. ( $\sigma_2 = 0$ ,  $\epsilon_2 = 1$ ,  $\sigma_4 = 5e-3$ ,  $\epsilon_4 = 3$ )

Characteristic impedance :

$$Z_c = [(Z_1 + Z_2 + Z_4) / Y_2]^{1/2} \quad (4.15)$$

As  $b \rightarrow a$  it is expected that  $k_L \rightarrow k_4$  but instead  $k_L \rightarrow \infty$  as shown in Figure 4.6.

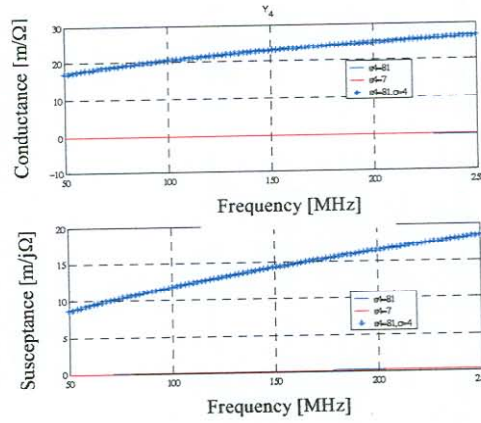


Figure 4.7 : Correction term

To remedy this deficiency in the limit as  $b \rightarrow a$ ,  $k_L \rightarrow k_4$  Chen and Warne define the exterior admittance per unit length as:

$$Y_4 = -i2\pi(i\sigma_4 + \omega\varepsilon_4) \frac{k_4 b H_1^{(2)}(k_4 b)}{H_0^{(2)}(k_4 b)} \quad (4.16)$$

where  $\varepsilon_4$  is the effective permittivity surrounding the medium. The correction term  $Y_4$  (Figure 4.7) also does not change significantly for varying ambient permittivities, except when the medium is conductive and  $Y_2$  seems to be the main contributor to impedance change for different dielectric mediums.

The complete transmission line theory wave number and characteristic impedance, that incorporates the correction factor, is given by:

Wave number :

$$k_L = [-(Z_1 + Z_2 + Z_4) \frac{Y_2 Y_4}{Y_2 + Y_4}]^{1/2} \quad (4.17)$$

Characteristic impedance :

$$Z_c = [(Z_1 + Z_2 + Z_4) \frac{Y_2 + Y_4}{Y_2 Y_4}]^{\frac{1}{2}} \quad (4.18)$$

Figure 4.6 shows the difference in the wave number with and without the exterior admittance. The centre conductor is viewed as perfect, making  $Z_1 = 0$ . The transmission line model is not applicable to bare antennas in matter and cannot be used in the limit  $b \rightarrow a$ . Only a two-layer problem consisting of the insulation and the surrounding ambient medium has been considered. In practice, this will not always be true, due to the fact that some plastic or PVC cover will shield the insulation from the ambient medium as illustrated in Figure 4.6. R. W. P. King, B. S. Tremblay and J. W. Strohbehn [16] introduced an effective wave number and permittivity for an equivalent dielectric composed of a single layer combining the electrical effect of the insulation and shield.

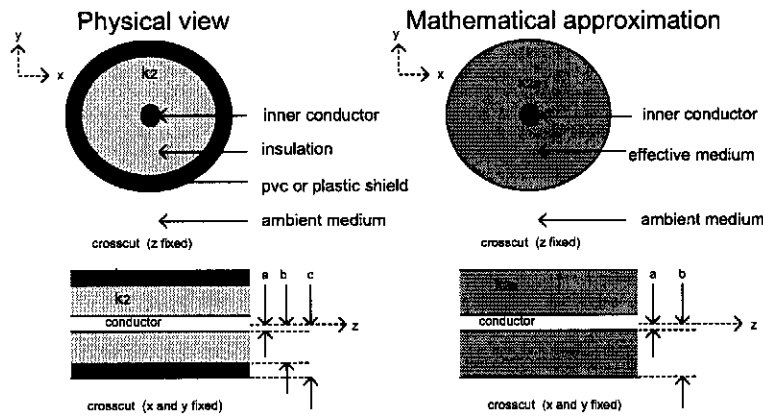


Figure 4.8 : Crosscut view of insulated antenna ( left : physical view , right : mathematical approximation )

The formulas are given as:

$$k_{2e} = k_2 \left[ \frac{\ln(c/a)}{\ln(b/a) + n_{23}^2 \ln(c/b)} \right]^{\frac{1}{2}} \quad (4.19)$$

$$\epsilon_{2e} = \epsilon_2 \left[ \frac{\ln(c/a)}{\ln(b/a) + n_{23}^2 \ln(c/b)} \right] \quad (4.20)$$

where  $n_{23}^2 = \frac{k_2^2}{k_3^2}$  and  $k_2$  and  $k_3$  are the wave numbers of regions 2 and 3. Figure 4.8 shows the physical problem, as well as the mathematical single layer approximation of the insulation plus shield.

### 4.3 Application of the complete TLM on insulated antennas

Section 4.3.1 concentrates on the practical implementation of the *TLM* to asymmetrical wire radiators of multiple sections. The solution was simplified considerably (Section 4.3.2) for symmetrical wire antennas by using *ABCD*-parameters and including lumped series resistors for resistively loaded antennas.

#### 4.3.1 Asymmetric dipole

For practical purposes, it is essential that the *TLM* be adaptable to handle radiators that are asymmetrical. The borehole radar probes will essentially be asymmetric, while the ground arm's length may vary according to the design of the electronics that it houses.

##### 4.3.1.1 Two sections

To clarify the implementation of the *TLM*, the current distribution and input impedance of the two-section asymmetric dipole shown in Figure 4.9 will be determined. The parameters are uniformly distributed over the length of each section. Thus there is a wave number ( $k_1$  and  $k_2$ ) and characteristic impedance ( $Z_{c1}$  and  $Z_{c2}$ ) associated with each section. The delta source gap is placed at  $z = 0$ , for this case. The current distribution and input impedance are derived in *Appendix C.1*. As shown by D. M. Claassen [3], the current distribution for the specific configuration in Figure 4.9 is:

$$\begin{aligned} I(z) &= B_1 \sin(k_1(h_1 + z)), -h_1 \leq z < 0, \\ I(z) &= B_2 \sin(k_2(h_2 + z)), 0 \leq z < h_2, \end{aligned} \quad (4.21)$$

$$\text{where } B_1 = \frac{-jv_o^e}{Z_{c1} \cos(k_1 h_1) + Z_{c2} \cos(k_2 h_2)} \frac{\sin(k_1 h_1)}{\sin(k_2 h_2)}$$

$$B_2 = B_1 \frac{\sin(k_1 h_1)}{\sin(k_2 h_2)}$$

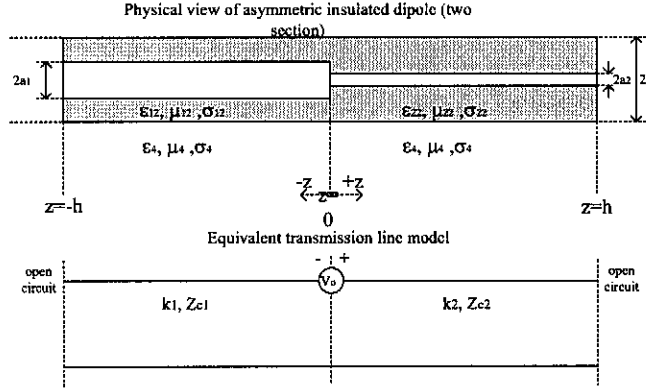


Figure 4.9 : Transmission line model : Asymmetric insulated dipole with two sections

The input impedance is thus, with  $v_0^s = 1$ ,

$$Z_{in} = 1/I(0) = \frac{1}{B_1 \sin(k_1 h_1)} = \frac{1}{B_2 \sin(k_2 h_2)} \quad (4.22)$$

#### 4.3.1.2 Multiple sections

To illustrate the flexibility of the model, Figure 4.10 also shows an asymmetric dipole consisting of different wave numbers and characteristic impedances for different sections  $i = \{1..N\}$ . Each section can represent either a resistor or a conductor of variable thickness. A series resistor can be implemented by changing  $Z_i$  to have a finite conductance representing a lumped resistor of the same length as the section. It is thus possible to load the antenna with either series uniform resistance or individual lumped resistors. The main advantage of the transmission line model is that the attenuation factor and propagation constant along the line can be extracted. If the attenuation profile along the conductor is known, it will make it possible to design the series loading to adjust to the dielectric loading of the ambient medium. The model also provides for a conducting ambient medium and will give insight into the possible loading effect, if any, on the insulated antenna. The solutions to the one-dimensional wave equation for each section using the notation in Figure 4.10 is:

*Voltage along the section :*

$$V_i(z) = jA_i Z_{oi} \sin(k_i (h_i + z)) - jB_i Z_{oi} \cos(k_i (h_i + z)) \quad (4.23)$$

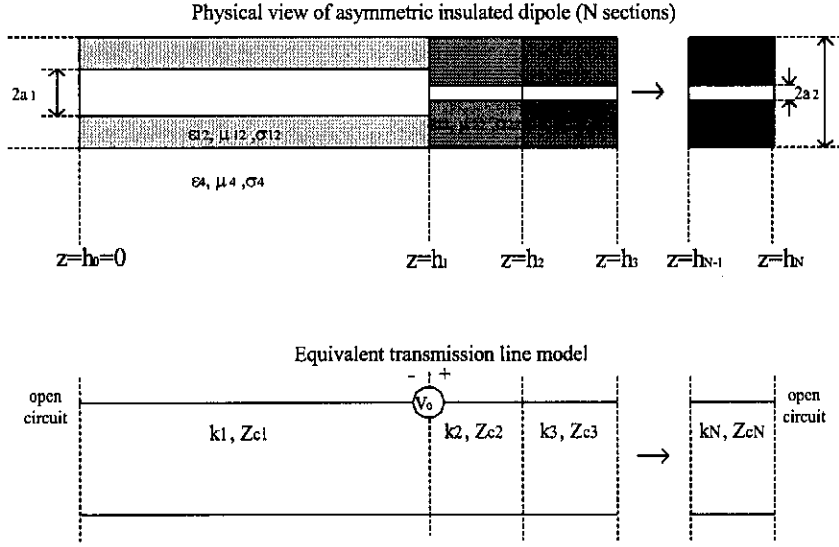


Figure 4.10 : Transmission line model : Asymmetric insulated dipole with N sections

*Current along the section :*

$$I_i(z) = A_i \cos(k_i(h_i + z)) + B_i \sin(k_i(h_i + z)) \quad (4.24)$$

where  $h_{i-1} < z < h_i, i = \{1..N\}$

The boundary conditions linking the sections are gives as:

*Voltage continuity between sections :*

$$V_{i+1}(h_i^+) = V_i(h_i^-), \quad z = h_i, i = \{2..N-2\} \quad (4.25)$$

*Current continuity between sections :*

$$I_{i+1}(h_i^+) = I_i(h_i^-), \quad z = h_i, i = \{2..N-2\} \quad (4.26)$$

$z = h_0 = 0$

:

$$I_0(0) = 0 \quad (4.27)$$

$z = h_N$

:

$$I_N(h_N) = 0 \quad (4.28)$$

*Over the voltage gap*

:

$$V_{v+1}(h_v^+) - V_v(h_v^-) = v_v^e, \quad z = h_v, v = \{2..N-2\} \quad (4.29)$$

where the source is situated between  $\nu$  and  $\nu + 1$ , there will be  $2N-1$  unknowns for N sections.

The unknowns can be solved by means of matrix manipulation in the form  $\bar{U} = \bar{M}^{-1}\bar{S}$ .  $\bar{U}$  is the vector of unknowns,  $\bar{S}$  is the source vector, and  $\bar{M}$  is the boundary condition matrix.

### 4.3.2 Symmetric dipole

To reduce the complexity of the boundary condition when using multiple sections, it may be more convenient to use the *ABCD* parameters of a two-port network. The *T matrix* is an impedance matrix and cannot account for a source gap. Thus the *ABCD* parameters will only be implemented for a symmetrical loaded or unloaded dipole. It is known that a symmetrical dipole can be seen as a monopole plus its image, as shown in Figure 4.11. The source voltage of the monopole, must be halved for electrical equivalence between the dipole and monopole. The *T matrix* of one section

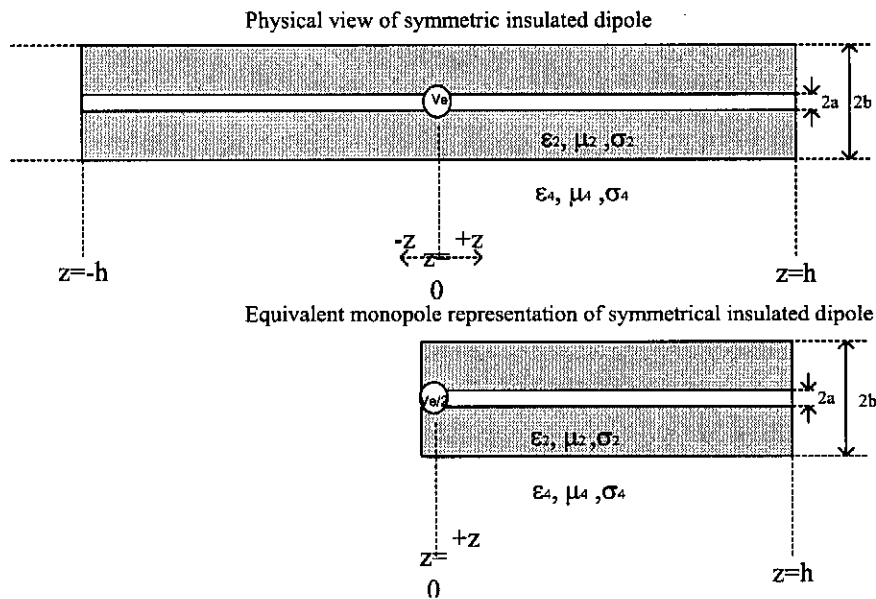


Figure 4.11 : Physical view of representing a dipole as an equivalent monopole

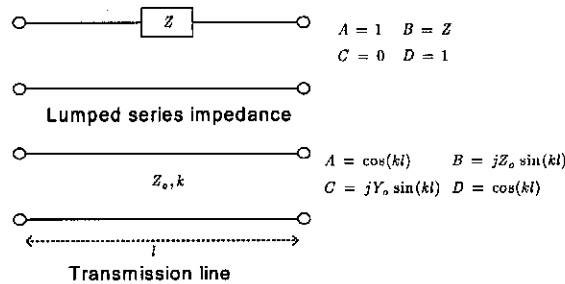


Figure 4.12 : ABCD impedance representation of a lumped series impedance and transmission line

can be multiplied by another section to find the combined effect, and will incorporate the boundary conditions automatically. Figure 4.12 shows the *ABCD*-parameters of a transmission line with a specific wave number and characteristic impedance and also for a lumped series impedance. *Appendix C.2* explains how multiple sections can be joined and how to extract the input impedance. The *T matrix* gives the freedom of incorporating lumped series impedances to load the dipole non-uniformly as is required for the Wu-King resistive profile.

#### **4.4 Comparison between FEKO (MoM) and TLM**

Two antennas consisting of an ordinary dipole (Section 4.4.1) and a 100% Wu-King antenna (Section 4.4.2) were implemented to illustrate the margin of error introduced by the transmission line model when compared to commercially available simulation tools.

##### **4.4.1 Insulated conducting dipole antenna**

The parameters (subscripts of Figures 4.13, 4.14) of the antenna are based on Figure 4.11. Due to the significant differences between the wave number of the insulation (air) and the ambient medium (sea water) in Figure 4.13, close resemblance was found between the *TLM* and *MoM*.

Surprisingly, Figure 4.14 shows that the *TLM* can be accurate for ambient permittivities of as low as 7, and prove to be an effective antenna model for the gold mine environment where dielectric constants might vary between 6-9. This shows that the *TEM* wave approximation for electrically small cross-section insulated antennas holds true. The *TLM* gives physical insight into the complex nature of antennas in matter and aids the understanding in terms of physical impedance parameters. The slight difference between the *TLM* and *MoM* may be due to the fact that the *TLM* does not incorporate any stray capacitance at the open ends. The stray capacitance should increase when the *a/b* ratio and ambient permittivity decrease and cause the antenna to look electrically shorter. The stray capacitance effect is very slight and can be observed in Figure 4.14 for an ambient permittivity of 7. The resonant frequency of the *TLM* antenna is lower than for the *MoM* modelled antenna. As discussed in Section 4.3, the difference between the *TLM* and *MoM* can be due to a deficiency in the radiation condition for the *TLM*.

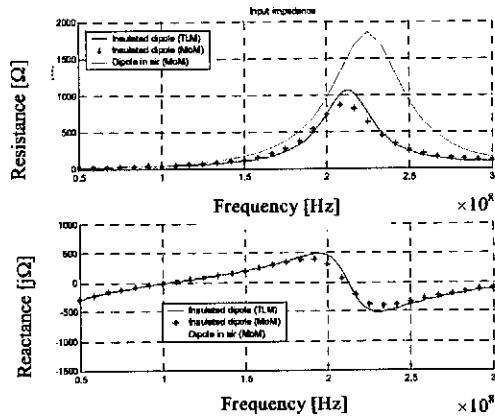


Figure 4.13 : Input impedance of an insulated dipole in sea-water, and a dipole in air ( $h = 0.6\text{m}$ ,  $a = 1.5\text{mm}$ ,  $b = 10.5\text{mm}$ ,  $\epsilon_2 = 1$ ,  $\mu_2 = 1$ ,  $\sigma_2 = 0$ ,  $\epsilon_4 = 81$ ,  $\mu_4 = 1$ ,  $\sigma_4 = 4$ )

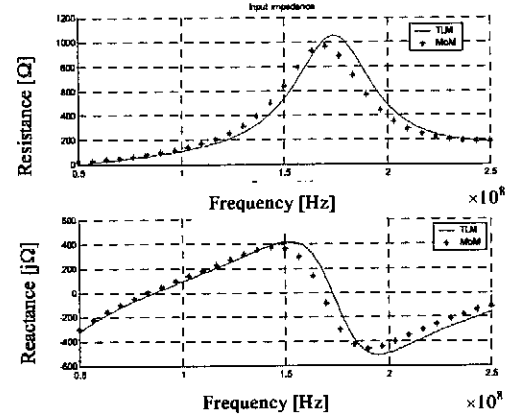


Figure 4.14 : Input impedance of insulated dipole, ( $h = 0.6\text{m}$ ,  $a = 1.5\text{mm}$ ,  $b = 10.5\text{mm}$ ,  $\epsilon_2 = 1$ ,  $\mu_2 = 1$ ,  $\sigma_2 = 0$ ,  $\epsilon_4 = 7$ ,  $\mu_4 = 1$ ,  $\sigma_4 = 0$ )

#### 4.4.2 Insulated Wu-King antenna

The Wu-King profile was designed for air ( $\epsilon_r = 1$ ) and incorporated 9 resistors along each arm of the antenna. The total length of the antenna was 2m and the design frequency was chosen to be 100 MHz.

Resistor position (mm)	55	166	278	389	500	611	722	833	944
Resistor value ( $\Omega$ )	38	83	95	111	133	167	224	340	733

Table 4.1 : 100% Wu-King resistor values along a 1m length of dipole arm

The *T matrix* method was used to include discrete resistors at the specified points shown in Table 4.1. Figures 4.15 and 4.16 show that the *TLM* and *MoM* simulations compare well for loaded antennas. The results are encouraging because the *TLM* enables an understanding of the loading effect generated by certain ambient dielectrics, as well as for a lossy ambient medium.

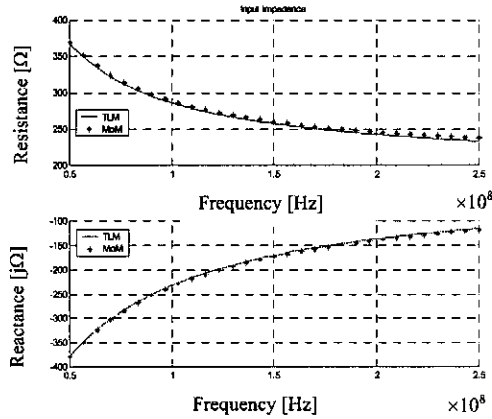


Figure 4.15 : Input impedance of insulated WK-antenna in sea-water. (  $h = 1\text{ m}$ ,  $a = 1.5\text{ mm}$ ,  $b = 10.5\text{ mm}$ ,  $\epsilon_2 = 1$ ,  $\mu_2 = 1$ ,  $\sigma_2 = 0$ ,  $\epsilon_4 = 81$ ,  $\mu_4 = 1$ ,  $\sigma_4 = 4$  )

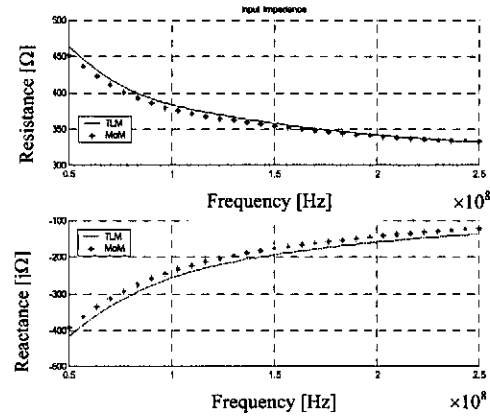


Figure 4.16 : Input impedance of insulated WK-antenna (  $h = 0.6\text{ m}$ ,  $a = 1.5\text{ mm}$ ,  $b = 10.5\text{ mm}$ ,  $\epsilon_2 = 1$ ,  $\mu_2 = 1$ ,  $\sigma_2 = 0$ ,  $\epsilon_4 = 7$ ,  $\mu_4 = 1$ ,  $\sigma_4 = 0$  )

#### 4.5 Comparing the insulated antenna with a bare antenna equivalent in a dielectric medium

Because of the physical limitations on the antenna, dielectric loading seems preferable to resistive loading for improving the input impedance and efficiency of the antenna. The only variable besides the length that can be manipulated to adjust the antenna characteristics is the electrical properties of the insulation.

In practice, the antenna will be surrounded by air in the borehole. Using equation (4.20), the influence of the layer of air can be approximated to determine whether insulating the antenna will have a significant loading effect. The dielectric loading will have the best results where the electrical properties of the insulated area and ambient medium match. Figure 4.8 can be used as reference, where  $81 \geq \epsilon_2 \geq 1$ ,  $\epsilon_3 = 1$ . The borehole with the smallest diameter that will be used for exploration is represented in Figure 4.17 (EXT with core diameter = 37.7 mm).

This should show the situation in which the air have the lowest influence. Figure 4.17 shows that the layer of air reduces the effective permittivity of the insulated area. The *TLM* is described with a specific characteristic impedance and wave number.

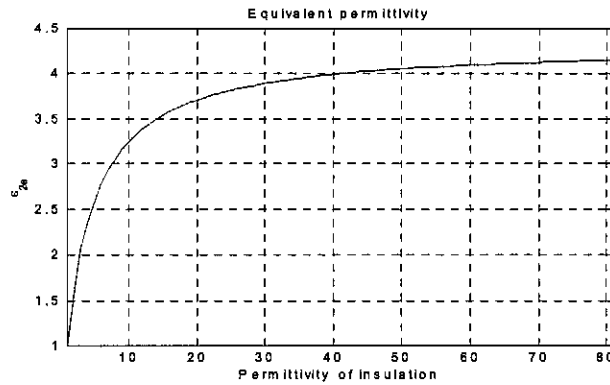


Figure 4.17 : Effective permittivity of mathematical approximated borehole. (a = 1.5 mm, b = 10.5 mm, 18.85mm)

It will thus be possible to extract a relative permittivity from the wave number describing the combined effect of the insulation and surrounding medium. The antenna can be seen as a bare antenna in matter with the same electrical properties as the permittivity extracted from the wave number. The Wu-King resistive profile can be adjusted according to the amount of dielectric loading imposed by the insulation and exterior medium. Adjusting the Wu-King profile for bare antennas in non-conducting mediums is known.

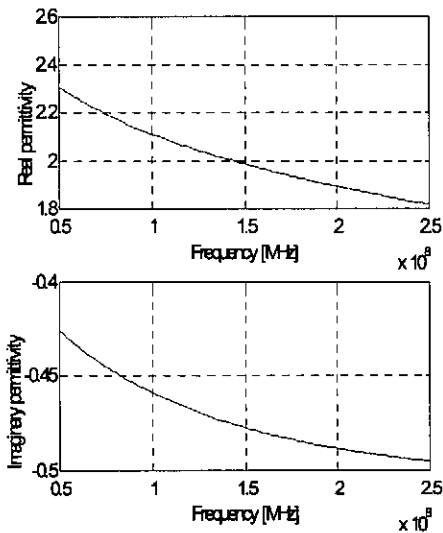


Figure 4.18 : Permittivity extracted from the wave number. ( $\epsilon_1=7, \epsilon_2=1, b = 10.5 \text{ mm}, a = 1.5 \text{ mm}$ )

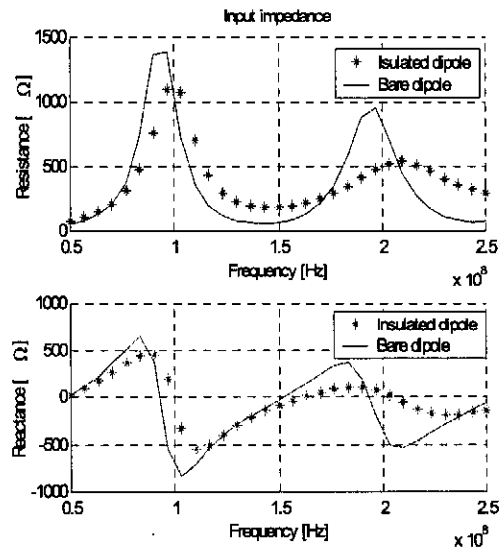


Figure 4.19 : Comparison between bare dipole in dielectric constant of 2.1 and insulated antenna

The method seems attractive for handling the resistive profile for insulated Wu-King antennas but this does not necessarily mean that the assumption is correct. Figure 4.18 shows the relative permittivity extracted from the wave number. The permittivities vary with frequency due to the Hankel functions in the radiation term.

Figure 4.19 gives the input impedance for a bare antenna (2m dipole) where the relative permittivity was taken as 2.1 @100 Mhz. The capacitive input reactance is dominated by the permittivity of the surrounding mediums. The input impedance of the insulated antenna does not seem to compare well at the higher frequencies with the equivalent bare antenna model. The resonance frequencies of the two models are quite close and it seems that the model works for low frequencies (i.e. below first resonance).

## **4.6 Conclusion**

The *TLM* initially looked attractive because it defines the insulated antenna in terms of parameters known to engineers, even though the model is not applicable to bare antennas and electrically long wire antennas. For the borehole environment, the model is a reasonably accurate simulation tool that can handle not only resistively loaded antennas but also asymmetric antennas.

The speed at which the simulations can be simulated above that of an expensive electromagnetic code such as FEKO™ (if dielectric cylindrical surfaces are used for the borehole) justifies the usefulness of the model. The *TLM* also provides a means of understanding the mechanisms that influence the antennas in the borehole. The chapter has revealed that the air insulation in the borehole is the dominant layer when the antenna is situated in the centre of a borehole.

## Chapter 5

### MODELLING OF RADAR PROBES

#### 5.1 Introduction

This chapter deals with the electromagnetic numerical simulations of the current radar probes to test their applicability to pulsed radar applications. The antennas will be investigated in both the frequency and time domain to determine the input impedance and far-field and radiation characteristics for a given input transient of the antennas.

The wire antennas adapted for the following sections had two equal length arms of 1 meter with a radius of 1.5 mm in *FEKO™* and infinitely thin in *CST™*. This length was chosen as a practical value for the probes to fit in a standard mine cage. The three configurations (Figure 5.1) that were investigated were a conducting and a resistive dipole and a combination of both that will be called a asymmetrical dipole as introduced by D. M. Claassen [3]. A differential source model is used in all cases.

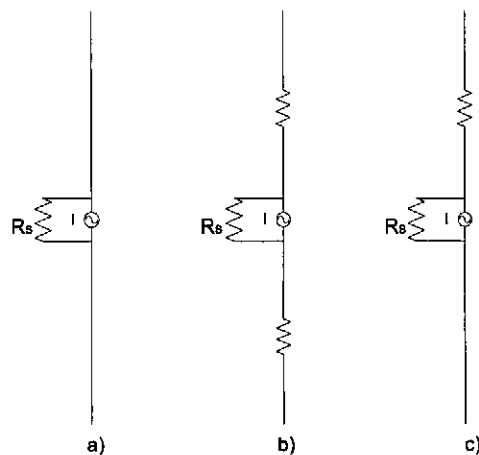


Figure 5.1 : (a) Conducting, (b) Resistive and (c) Asymmetric dipole

## 5.2 Conducting dipole

In this section, the common dipole is investigated to show that the antenna is not suited for transmitting or receiving finite period signals. Firstly, a frequency domain study is conducted of a dipole in air (Section 5.2.1) and in a mine environment (Section 5.2.3) and, secondly, the radiation properties for a Gaussian input signal are given in Section 5.2.4. Finally, the pulse receiving ability of the antenna for a given electric field illumination is studied in section 5.2.5.

### 5.2.1 Conducting dipole in air

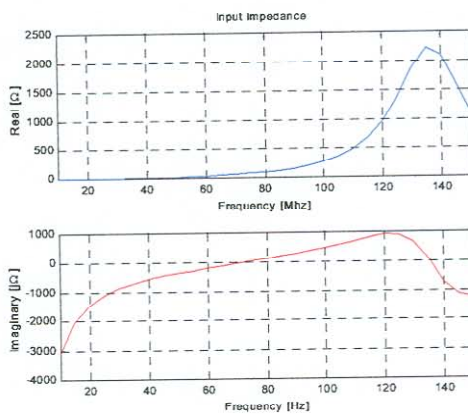


Figure 5.2 : Input impedance of conducting dipole

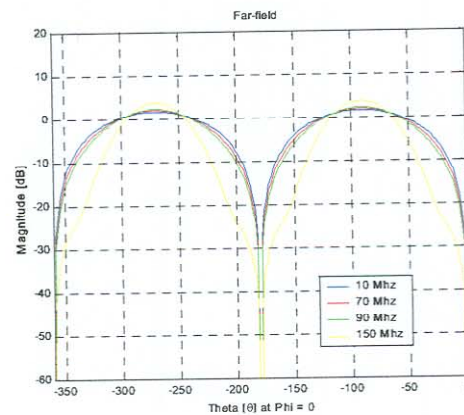


Figure 5.3 : Far-field gain of conducting dipole

The conducting dipole (for the geometry under consideration) resonates at 72 MHz (Figure 5.2), and the gain of the far-field is given by

$$Gain(\theta, \phi) = e_r D(\theta, \phi) \quad (5.1)$$

where  $e_r = \frac{\text{Radiated power}}{\text{Total input power}}$

The antenna radiates 100% efficiently and the gain is constant over frequency (Figure 5.3) except at 150 MHz. As expected, the gain peaks at broadside ( $\theta = 90^\circ$ ) with a maximum of around 2 dB. The pattern starts to deteriorate at the anti-resonance, due to the fact that the wavelength of the currents at this frequency are more than one multiple of a quarter wavelength compared to the dimension of the dipole arm. This antenna cannot be used for broadband applications as the

antenna's input impedance varies considerably. This makes it difficult to match to any source, and its periodic nature encourages it to ring, which diminishes the resolution of the system.

### 5.2.2 Insulated dipole in a mine environment

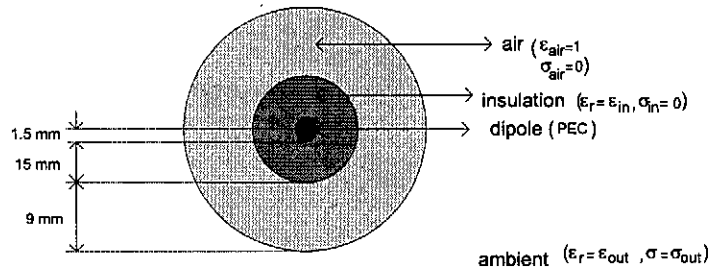


Figure 5.4 : Cross-sectional view of insulated dipole in an AXT borehole (dipole situated in the centre of the hole)

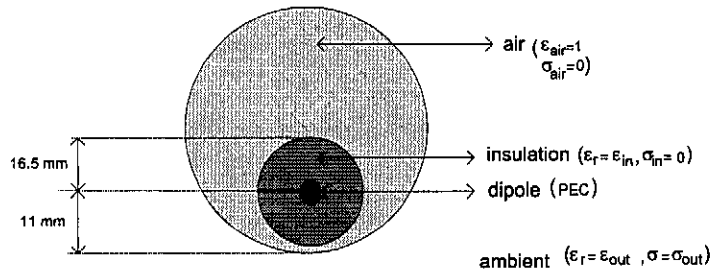


Figure 5.5 : Cross-sectional view of insulated dipole in an AXT borehole (dipole situated off-centre)

Using the transmission line model (*TLM*) only provides efficient solutions for a insulated wire antenna situated in the centre of a borehole of small cross-sectional dimensions (Figure 5.3), and is also not applicable to ambient mediums with low dielectric constants. In practice, the radar probe will lie off-centre in the borehole (Figure 5.4) and *FEKO<sub>™</sub>* is able to simulate the wire antennas situated either in the centre or off-centre in the borehole as verified in *Chapter 2*.

Dielectric cylinders were used for both the insulation and borehole boundaries. The investigation started by changing the insulation dielectric constant for a given ambient permittivity of 7 (common for rock). Physically, the ambient parameters are set and the only parameter that can be changed is the insulation material of the antenna, in order to achieve dielectric loading and to

improve coupling into the rock. The input reactance (Figure 5.7) shows that the first resonance can be reduced by approximately 7 MHz with different insulations. There is a square root law governing the wavelength with changing dielectric constants and the resonance frequency can be related to the same function.

Due to the square root law, practical dielectric constants for the insulation higher than 10 will add little to the reduction of the input capacitance. The anti-resonance peaks can be seen in the input resistance (Figures 5.6) where the second anti-resonant peak (above 100 MHz) is smaller than the first. The input impedance (Figures 5.8 and 5.9) for a dipole situated off-centre does not differ

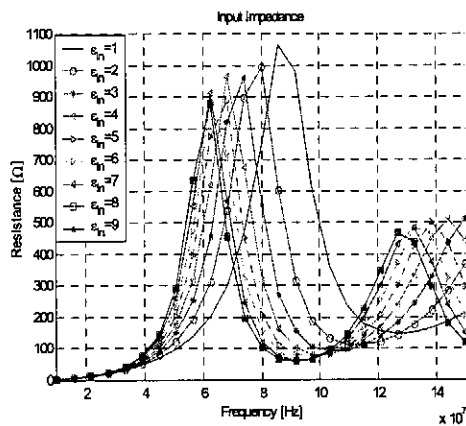


Figure 5.6 : Input resistance of centre insulated conducting dipole ( $\epsilon_{in} = 1-9$ ,  $\sigma_{in} = 0$ ,  $\epsilon_{out} = 7$ ,  $\sigma_{out} = 0$ )

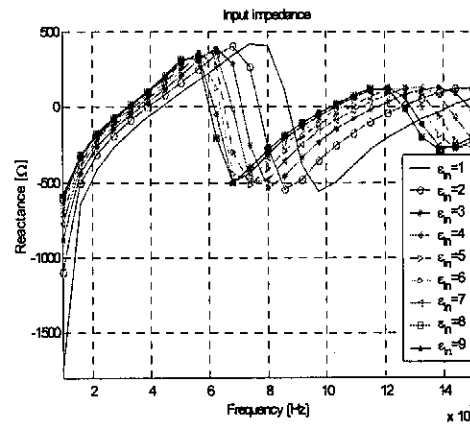


Figure 5.7 : Input reactance of centre insulated conducting dipole ( $\epsilon_{in} = 1-9$ ,  $\sigma_{in} = 0$ ,  $\epsilon_{out} = 7$ ,  $\sigma_{out} = 0$ )

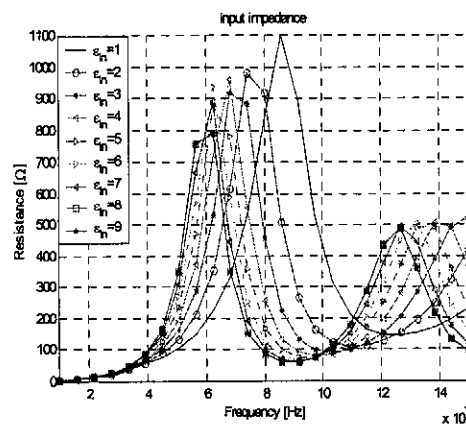


Figure 5.8 : Input resistance of off-centre insulated conducting dipole ( $\epsilon_{in} = 1-9$ ,  $\sigma_{in} = 0$ ,  $\epsilon_{out} = 7$ ,  $\sigma_{out} = 0$ )

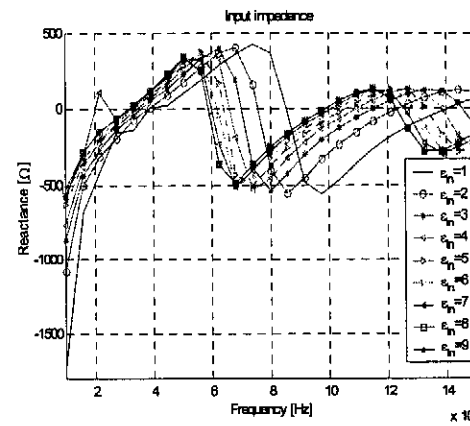


Figure 5.9 : Input reactance of off-centre insulated conducting dipole ( $\epsilon_{in} = 1-9$ ,  $\sigma_{in} = 0$ ,  $\epsilon_{out} = 7$ ,  $\sigma_{out} = 0$ )

substantially from the results obtained for the centre dipole. The resonance is below 40 MHz for air as insulation, where it was just above 40 MHz for the centre dipole. The small effect that the positioning of the dipole has in the borehole is predictable, as the cross-sectional diameter of the borehole is electrically small compared to the wavelength. A strange peak in the input impedance (Figure 5.9) is seen for (off-centre dipole)  $\epsilon_{in} = 7$ . The source is unknown but thought to be a computational error or an error caused by not having enough dielectric triangles at the boundary where the insulation nearly touches the borehole.

The gain is calculated for the theta component at  $\phi = 0^\circ$  (Figure 5.10). At the first resonance, the gain is 2-3 dB<sub>i</sub>, as expected. Near the first anti-resonance, the gain increases due to the directivity increase of the physical structure. After the first anti-resonance, the gain decreases steadily with a minimum at the second anti-resonance where the pattern will display multiple lobes off broadside, due to the current distribution on the wire.

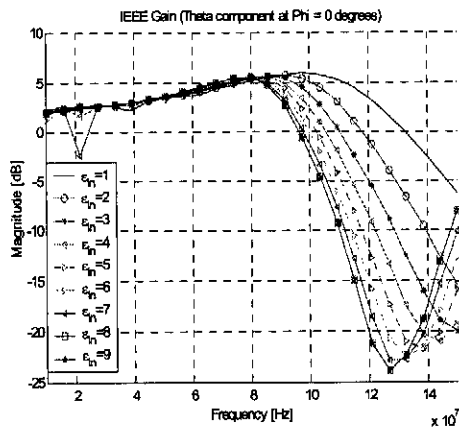


Figure 5.10 : Far-field gain of off-centre dipole ( $\theta$  component at  $\phi = 0^\circ$ )

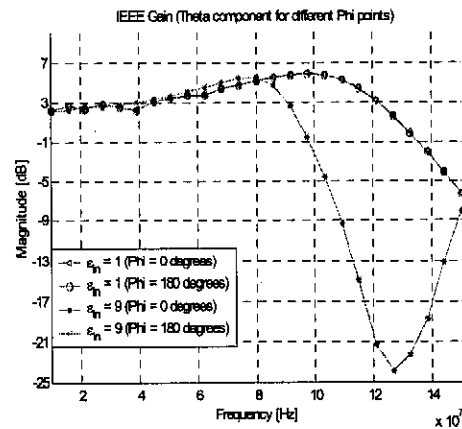


Figure 5.11 : Far-field gain of off-centre dipole for different insulation permittivities and  $\phi$  angles

Figure 5.11 shows the broadside gain for  $\phi = 0^\circ$ , and  $180^\circ$  and for different insulation permittivities. There is no significant pattern deformation at broadside if the antenna is situated off-centre in the borehole.

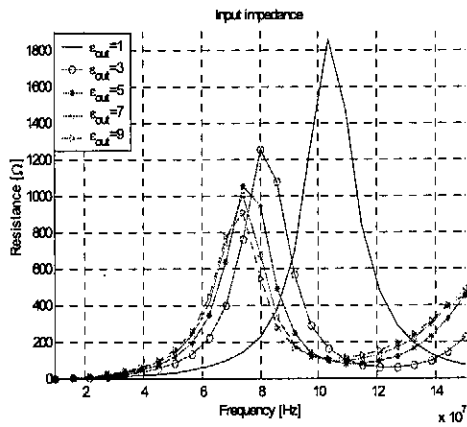


Figure 5.12 : Input resistance of centre-insulated conducting dipole ( $\epsilon_{in} = 3.7$ ,  $\sigma_{in} = 0$ ,  $\epsilon_{out} = 1;3;5;7;9$ ,  $\sigma_{out} = 0$ )

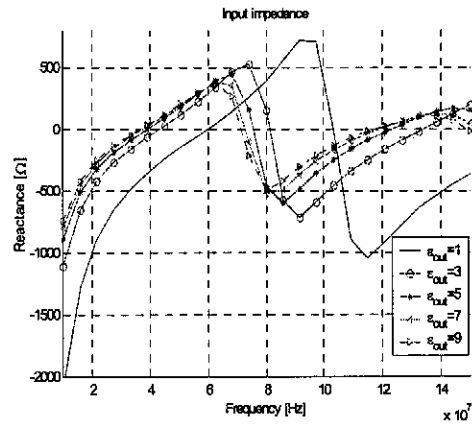


Figure 5.13 : Input reactance of centre-insulated conducting dipole ( $\epsilon_{in} = 3.7$ ,  $\sigma_{in} = 0$ ,  $\epsilon_{out} = 1;3;5;7;9$ ,  $\sigma_{out} = 0$ )

This shows, in conjunction with the input impedance, that the probe can be simulated as being in the centre of the borehole if phi dependence of the pattern is not needed.

Insulated antennas can be used for diagnostic purposes due to their insensitivity to the ambient mediums of different electrical properties. Figures 5.12 and 5.13 give the input resistance and reactance where the insulation dielectric constant is kept constant at 3.7 (polyurethane) and the ambient dielectric constant is varied. For the case where the ambient permittivity is higher than the insulation, the input impedance does not vary much, except where the dielectric constant is low, as with air. The highest loss factor associated with gold mine rock samples was measured by M. Rütshlin [17]. A loss factor of 0.0679 at 29.1 MHz was added to an ambient dielectric constant of  $\epsilon_{out} = 7$  for a polyurethane insulation and the input impedance were compared with the results obtained without the loss factor (Figures 5.14, 5.15).

The results show that the low conductivity adds no significant changes to the input impedance of the antenna. Higher loss factors may change the input impedance due to conduction currents flowing in the ambient medium but there is no practical use in surveying high loss mediums due to the strong attenuation of the signal.

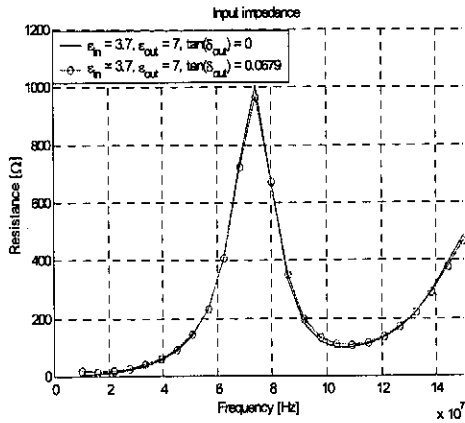


Figure 5.14 : Input resistance of conducting insulated antenna with and without an ambient loss factor

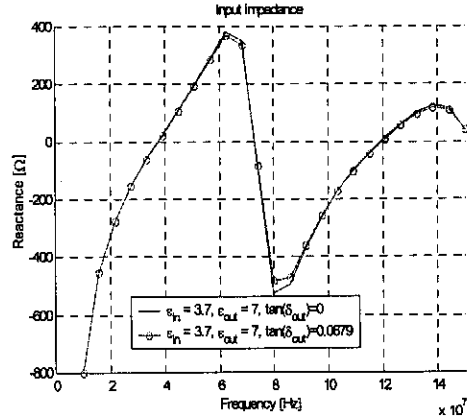


Figure 5.15 : Input reactance of conducting insulated antenna with and without an ambient loss factor

### 5.2.3 Pulse-transmitting characteristics of conducting dipole

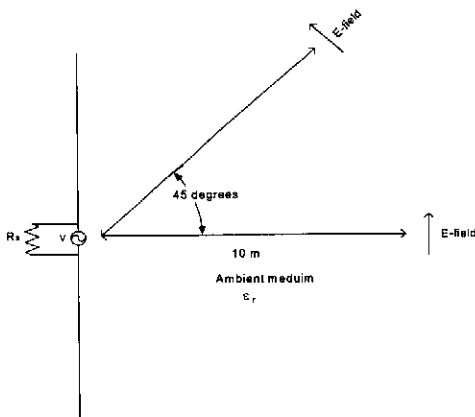


Figure 5.16 : Simulation geometry for pulse-transmitting investigations

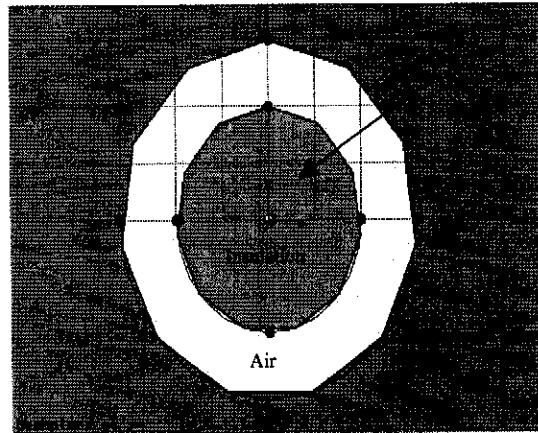


Figure 5.17 : Cross-sectional view of AXT borehole and insulated antenna in *CST* with the field cells (refer to Figure 5.4 for the dimensions).

Frequency techniques can be used to predict the antenna bandwidth, and whether it is dispersive. With difficulty and frequency, windowing the radiation can be investigated as a function of time, using a *Fourier Transform* as a time-based code. *CST* can be used directly to view the electric field at some position from the antenna as a function of time.

A Gaussian pulse with a frequency content of 0-100 MHz (frequency band of interest) was used as input to a voltage source ( $R_s = 1 \Omega$ ) in order to simulate the low output impedance switching FET of the current radar. It is assumed that the FET stays open until the transient on the antenna is fully attenuated.

As discussed in *Chapter 3*, the radiation characteristics for a low impedance or high impedance source resistance differ, which causes the natural frequency of the electric field transient to change. The electric field was extracted at broadside and at a  $45^\circ$  angle from broadside, 10m away from the source position (Figure 5.16). The simulation was done for a dipole in air as well as for an AXT borehole.

The number of field cells in the borehole (Figure 5.17) is within the number of cells associated with the wavelength, given the surrounding dielectric constant. Increasing the number of cells in the borehole will produce a computer-intensive geometry if the electric field probe is situated 10m from the source point in an ambient dielectric constant of  $\epsilon_r = 7$ .

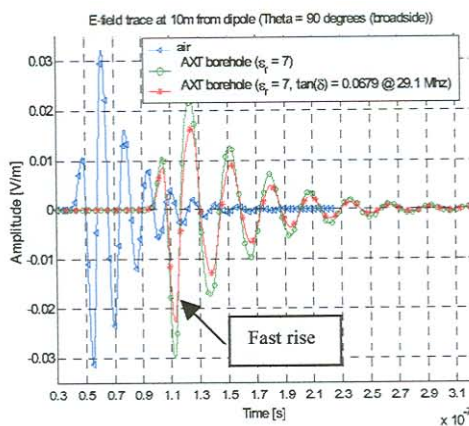


Figure 5.18 : Broadside trace of electric field for different surroundings

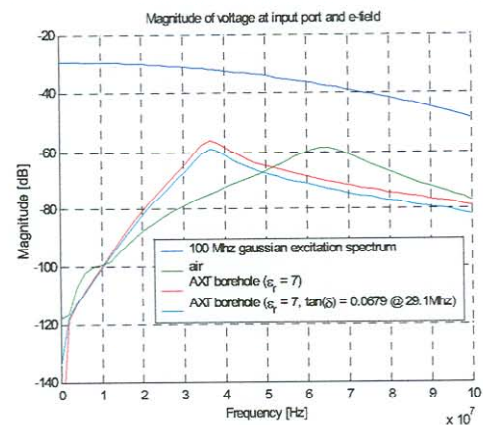


Figure 5.19 : Magnitude of broadside electric field trace for different surroundings

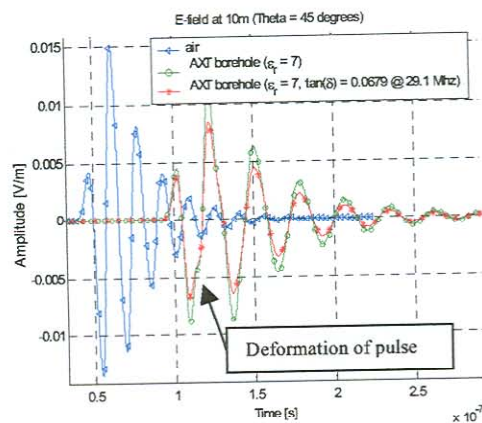


Figure 5.20 : Electric field at  $\theta = 45^\circ$  for different surroundings

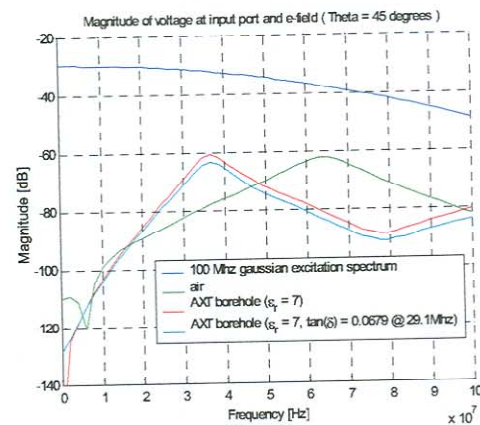


Figure 5.21 : Magnitude of electric field at  $\theta = 45^\circ$  for different surroundings

The electric field (Figures 5.18, 5.20) portrays the typical ringing behaviour associated with an electrically small resonating antenna. A few dB's loss (Figures 5.19 and 5.21) is introduced when the loss factor is added. There is no change in the period between the AXT borehole simulation with and without the loss factor. The loss factor is defined at a single frequency point and there should be no dispersion or gradual stretching in the period, as shown in the time traces.

The frequency of maximum magnitude accounts for the natural frequency of the electric field trace. The natural frequency for a voltage source is lower than for a current source, as discussed in *Chapter 3*. There is a significant decrease in natural frequency for  $\epsilon_r = 7$ , compared with air. The wave impedance is higher for  $\epsilon_r = 7$  than for  $\epsilon_r = 1$ , the electric field is attenuated more and the electromagnetic wave travels at a slower speed, as shown in the time traces. The fast rise in the first two peaks (Figure 5.18) of the time trace in the AXT borehole is due to the high amount of high frequency information that the pulse carries, compared to the natural frequency. This rise is not as noticeable for the dipole situated in air, because the natural frequency is high. The second peak in the first section of the time trace of the electric field probed at  $\theta = 45^\circ$  (Figure 5.20) is deformed.

5.2.4 Pulse-receiving characteristics of conducting dipole

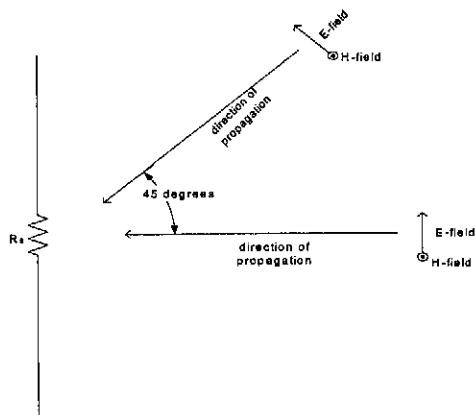


Figure 5.22 : Simulation configuration of plane wave incidence on a dipole antenna

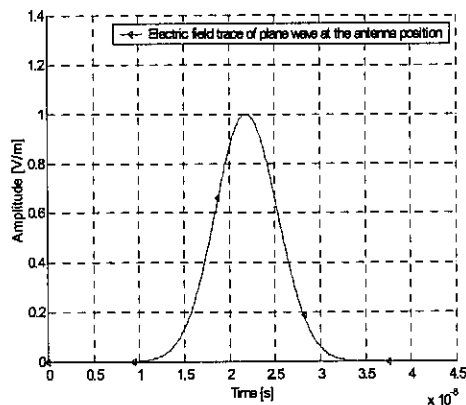


Figure 5.23 : Electric field time trace probed at antenna location

In order to establish the transient characteristics at the source resistance for various dipole configurations, the antenna was situated in air and illuminated with a plane wave that had a Gaussian transient with a frequency content of 0-100 MHz (Figures 5.22). Both a plane wave with a  $0^\circ$  and  $45^\circ$  offset from broadside ( $\theta = 90^\circ$ ) were simulated. Figure 5.23 shows the electric field probed tangentially to the orientation of the dipole arms for a broadside incident plane wave.

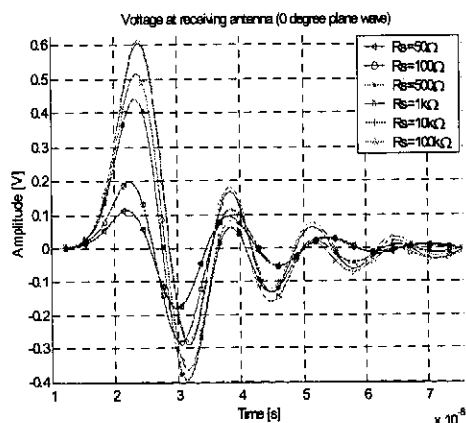


Figure 5.24 : Voltage transient at source for conducting dipole ( $0^\circ$  plane wave incidence)

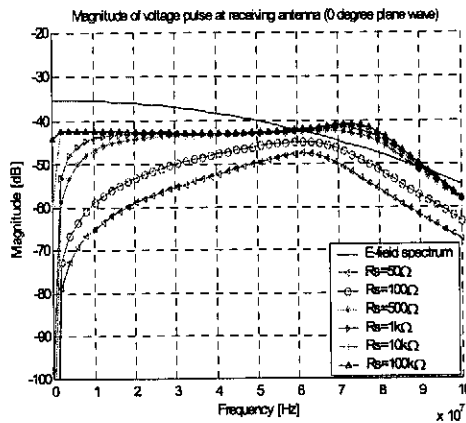


Figure 5.25 : Frequency spectrum of voltage transient at source for conducting dipole ( $0^\circ$  plane wave incidence)

An antenna has a multi-dimensional transfer function consisting of the various angles of illuminations. For electrically small resonating antennas this transfer function is not so sensitive to dimensional variations. The natural frequency differs for different source resistances (Figures 5.24, 5.25). For low source resistances, the natural frequency is lower than for higher source resistances. This phenomena was visible in the transmitting characteristics for a current and voltage source, due to the change in radiation mechanisms. The higher the source resistance the higher the low frequency information of the pulse and, because the natural frequency shifts higher for a current source, the rise of the first peak in the transient is faster. There is a reduction in the voltage (Figure 5.26, 5.27) magnitude for a  $45^\circ$  incident plane wave.

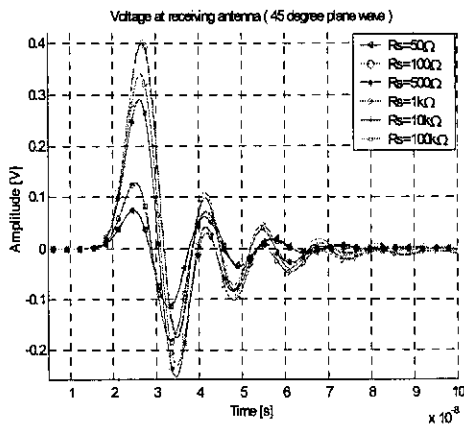


Figure 5.26 : Voltage transient at source for conducting dipole ( $45^\circ$  plane wave incidence)

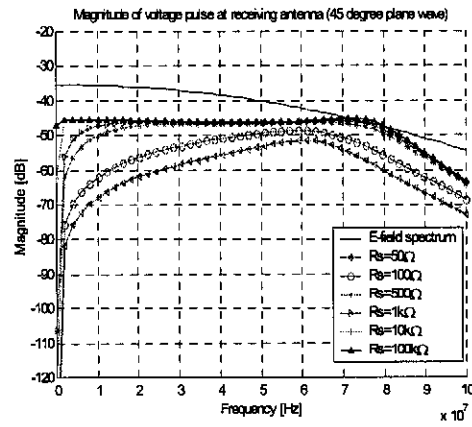


Figure 5.27 : Frequency spectrum of voltage transient at source for conducting dipole ( $45^\circ$  plane wave incidence)

Receiving a pulse from a current source seems attractive due to the flatter frequency response. A conducting dipole is not suitable for a pulse-receiving antenna due to the amount of ringing that occurs on the antenna. The high source impedance can only be realized with an active component. For higher receiving resistances, the natural frequency contains more energy that is spread over a longer period of time, which is visible in the ringing time transients.

### 5.3 Resistively loaded dipole antenna

From the frequency analysis of a resistively loaded antenna in air (Section 5.3.1), it is apparent that the antenna's dimensions are too small for the associated frequency spectrum to present the stable input impedance of a travelling wave antenna. The input impedance is influenced in the mine environment (Section 5.3.2). The main contribution of the resistive antenna is its ability to damp the oscillatory radiation behaviour (Section 5.3.3) observed for the conducting dipole in Section 5.2. The pulse-receiving capabilities also show great improvement for high source impedances (Section 5.3.4) which result in a more practical antenna for transient analysis.

#### 5.3.1 Resistively loaded dipole in air

A 100% Wu-King resistance profile (Table 5.1) was used. The design frequency was taken at the resonance frequency (75 MHz) of a conducting dipole of the same length.

Resistor position (mm)	55	167	278	389	500	611	722	833	944
Resistor value ( $\Omega$ )	38	83	95	111	133	167	224	340	733

Table 5.1 : Resistor values representing a Wu-King profile with  $f_{\text{design}}=75\text{MHz}$

The resistance of the input impedance (Figure 5.28) are more stable over frequency, making it more suitable for broadband applications. The far-field radiation pattern (Figure 5.29) shows a visible drop of at least 10 dB, compared to the conducting dipole. This loss can be attributed to the inability of the antenna to radiate efficiently due to resistive losses. Whether the antenna is at all suitable for a frequency pulse of 10-100 MHz is questionable. The antenna is still capacitive at the lower frequencies and the reactance seems to stabilise only for frequencies higher than the first resonance if it were to be a conducting dipole.

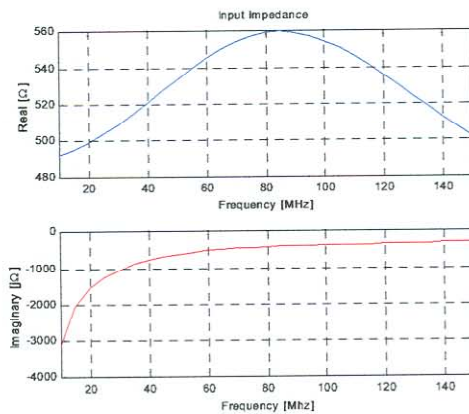


Figure 5.28 : Input impedance of 100% Wu-King antenna

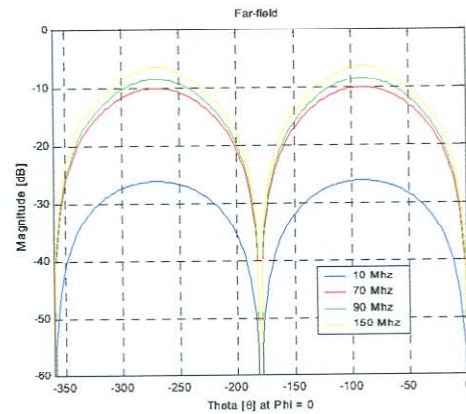


Figure 5.29 : Far-field gain of 100% Wu-King antenna

The most important attribute of the resistively loaded antenna is that there is no deformation in the radiation pattern with frequency. In essence the transfer function of the antenna over  $\theta$  stays the same, except for the attenuation in gain at various frequencies.

### 5.3.2 Insulated resistively loaded dipole in mine environment

The resistively loaded antenna has been simulated in the same AXT borehole and the dielectric constants of, firstly, the insulation and secondly, the ambient is varied (as shown in Section 5.2.2). The input impedance of the 100% Wu-King antenna follows the same square root variation in both the resistance and reactance, for different insulation dielectric constants (Figures 5.30 and 5.31). Due to the electrically small radius of the insulation, it is surprising to see that the resistively loaded dipole impedance becoming more stable for high insulation permittivities. The input impedance (Figures 5.32 and 5.33) of the resistively loaded antenna does not differ much from ambient permittivity variation, except for  $\epsilon_{out} = 1$ . As for the conducting dipole, the resistive insulated dipole's impedance is not visibly affected when the ambient medium has some conductivity (Figures 5.34 and 5.35).

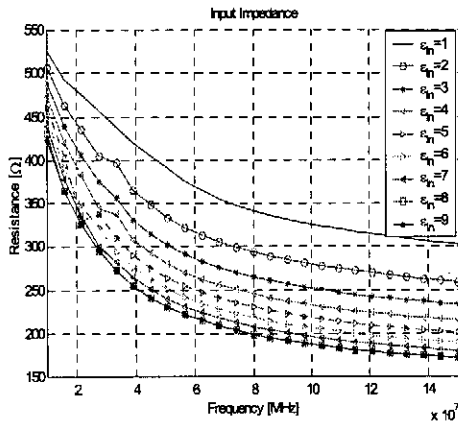


Figure 5.30 : Input resistance of centre-insulated resistive dipole ( $\epsilon_{in} = 1-9, \sigma_{in} = 0, \epsilon_{out} = 7, \sigma_{out} = 0$ )

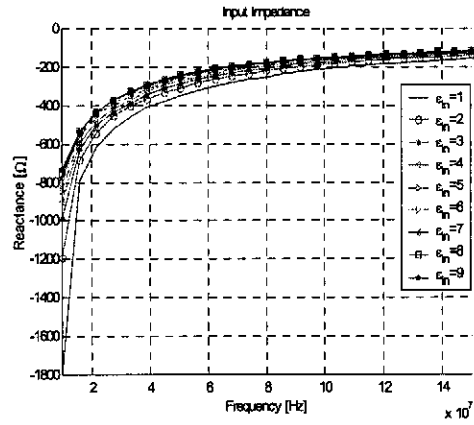


Figure 5.31 : Input reactance of centre-insulated resistive dipole ( $\epsilon_{in} = 1-9, \sigma_{in} = 0, \epsilon_{out} = 7, \sigma_{out} = 0$ )

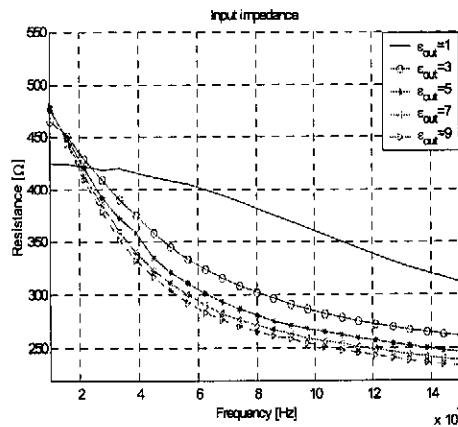


Figure 5.32 : Input resistance of centre-insulated resistive dipole ( $\epsilon_{in} = 3.7, \sigma_{in} = 0, \epsilon_{out} = 1;3;5;7;9, \sigma_{out} = 0$ )

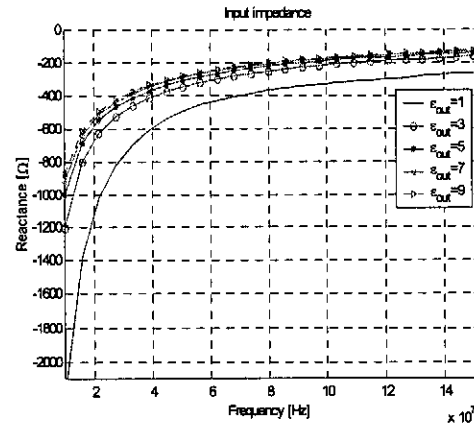


Figure 5.33 : Input reactance of centre-insulated resistive dipole ( $\epsilon_{in} = 3.7, \sigma_{in} = 0, \epsilon_{out} = 1;3;5;7;9, \sigma_{out} = 0$ )

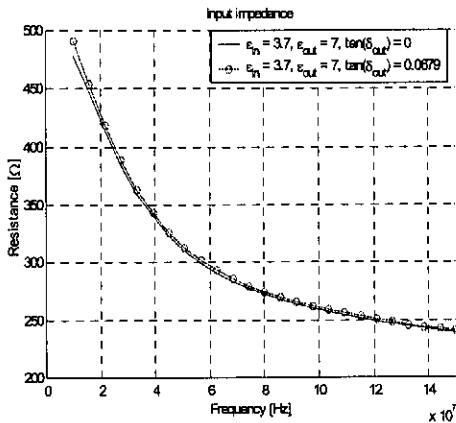


Figure 5.34 : Input resistance of resistive insulated antenna with and without an ambient loss factor

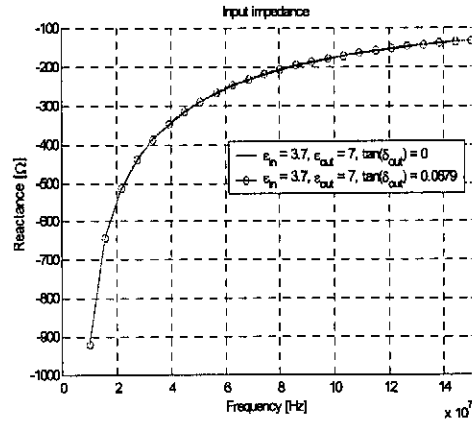


Figure 5.35 : Input reactance of resistive insulated antenna with and without an ambient loss factor

### 5.3.3 Pulse-transmitting characteristics of resistive dipole

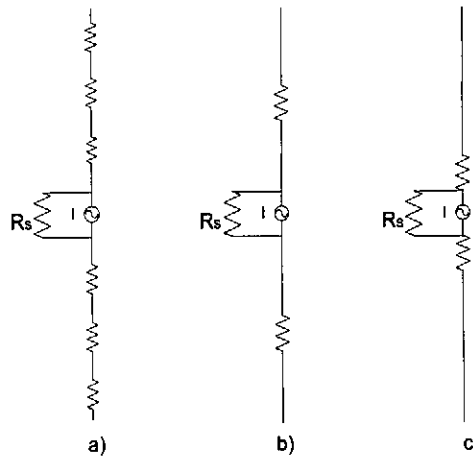


Figure 5.36 : a) Continuous loading b) centre loading and c) source loading

Three configurations (Figure 5.36 (a)-(b)) governing a resistive profile were investigated in order to produce a damped radiated transient. The conventional continuous Wu-King resistive profile loading was compared with two single resistor loadings, one at the centre of the dipole arm and the other near the source. Single resistor loading was considered because the antenna was electrically small and could not carry a travelling wave along its arms. It was proposed that only a single resistor could be used to damp the ringing on the antenna. Capacitive loading was not

considered because it causes degradation of the transmitted pulse, due to radiation associated with each capacitor or high impedance point, as shown by G. Smith and P. Montoya [18].

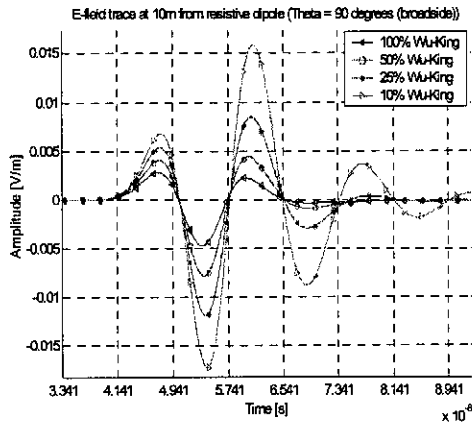


Figure 5.37 : Broadside trace of electric field for different percentage Wu-King loadings

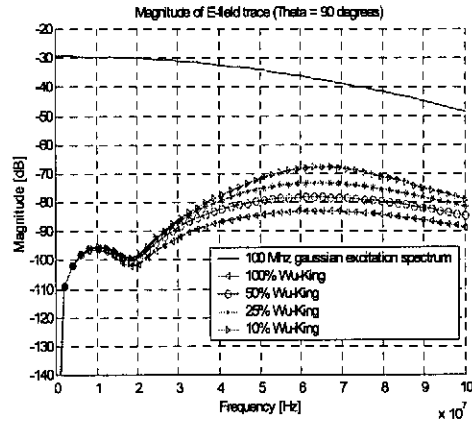


Figure 5.38 : Magnitude of the broadside electric field for different percentage Wu-King loadings

For the conducting dipole, the transmit transient of the resistive dipoles were excited with a Gaussian input pulse with a frequency content of 0-100 MHz ( $R_s = 1\Omega$ ). The electric field was

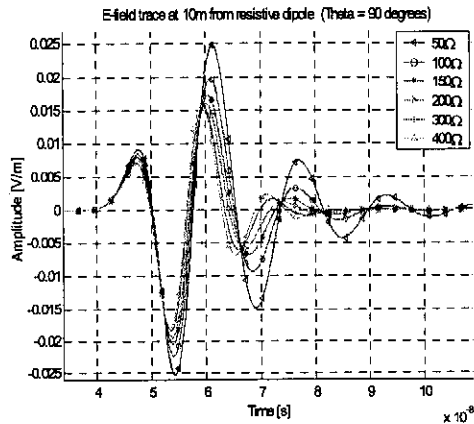


Figure 5.39 : Broadside electric field trace for different centre loadings

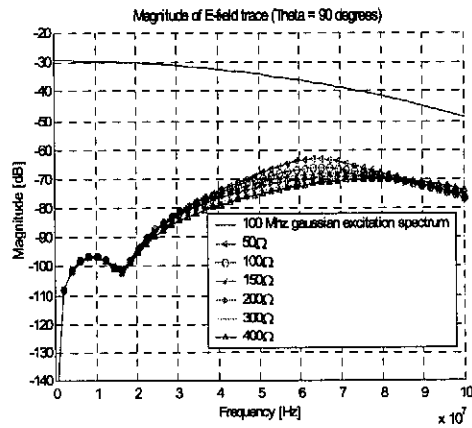


Figure 5.40 : Magnitude of broadside electric field trace for different centre loadings

probed broadside at a distance of 10m. Different percentage Wu-King loadings (Figures 5.37, 5.38) were used to see the influence that the reduction in loading has on the damping of the

transmitted field. The 100% and 50% Wu-King loadings did not have a significant ringing tail but transmitted little power and there was no predominant peak. The 10% and 25% Wu-King loadings reduce the resolution of the pulse due to their under-damped behaviour but transmitted nearly 10 dB (electric field strength) more at the high frequencies. The natural frequency remained constant at 100 MHz except for the 10 % loading where a slight rise was visible between 60 and 70 MHz in the frequency spectrum but it was not dominant.

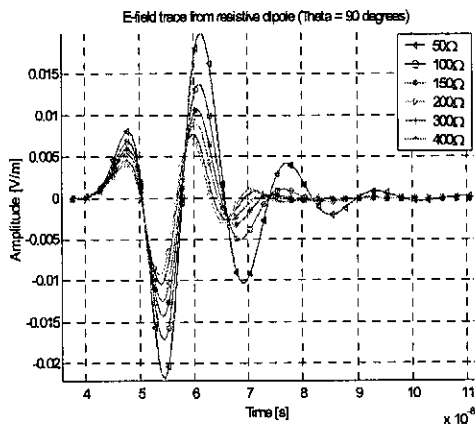


Figure 5.41 : Broadside electric field trace for different source loadings

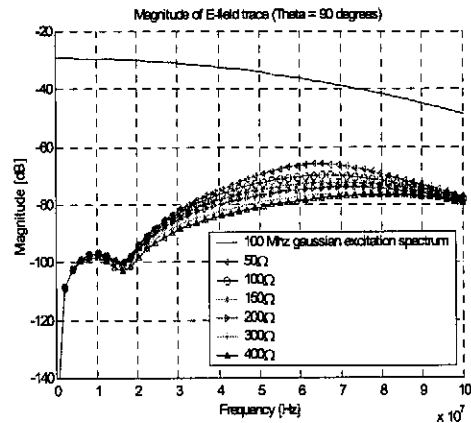


Figure 5.42 : Magnitude of broadside electric field trace for different source loadings

The source- and centre-loaded antennas were tested for various resistor values. The amplitude of the first peak for the centre-loaded antenna (Figure 5.39) primarily was the same for any resistor value. This was not the case for the source-loaded antenna (Figure 5.41). Some radiation may take place at the resistor positions due to charge reflection which causes changes in the radiation mechanism governing the tree topologies, as seen for a dipole excited by a voltage or current source. It is difficult to differentiate the severity of the reflections from the radiated transient. It is suggested that there may be a change in the radiation mechanism when resistors are introduced which is evident in the changing natural frequency of the magnitude plots for centre and source loading (Figures 5.40, 5.42).

### 5.3.4 Pulse-receiving characteristics of a resistive dipole

The continuous Wu-King resistively loaded antenna was illuminated at broadside and at  $45^\circ$  off broadside by a plane wave (electric field normal is perpendicular to direction of propagation). The Wu-King antenna, terminated with a conventional  $50\ \Omega$  source load, does not provide sufficient bandwidth for reception of electromagnetic transients. One possible way of increasing the bandwidth is by increasing the distributed resistances at the expense of sensitivity. As mentioned before, the antenna is too small electrically and increasing the distributed resistances will only cause the efficiency to decrease.

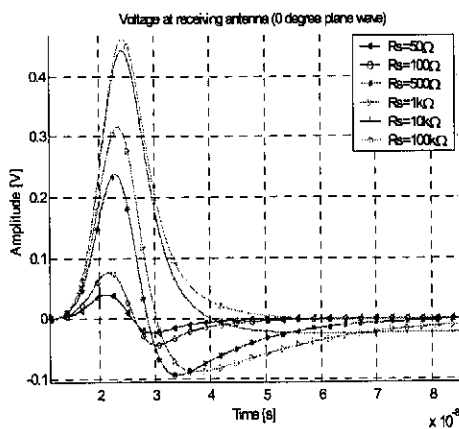


Figure 5.43 : Voltage transient at source for 100% Wu-King dipole ( $0^\circ$  plane wave incidence)

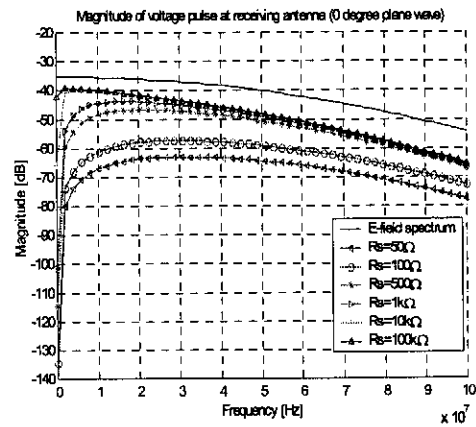


Figure 5.44 : Frequency spectrum of voltage transient at source for 100% Wu-King dipole ( $0^\circ$  plane wave incidence)

Increasing the source resistance increases the low frequency magnitude of the voltage transient for both the 100% and 50% Wu-King antennas (Figures 5.43-5.46). An increase in source resistance causes the under-shoot of the received voltage transient to decrease while the pulse peak lags the peak of the input electric field shown in Figure 5.23. The 50% Wu-King antenna provides better sensitivity with a relatively flat transfer. The pulse-receiving characteristics of

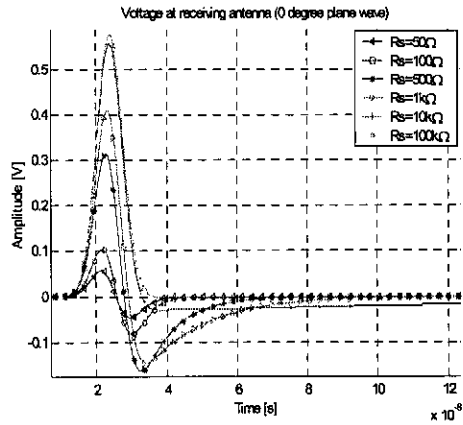


Figure 5.45 : Voltage transient at source for 50% Wu-King dipole ( $0^\circ$  plane wave incidence)

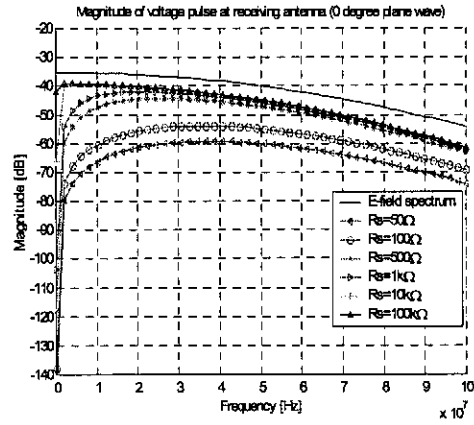


Figure 5.46 : Frequency spectrum of voltage transient at source for 50% Wu-King dipole ( $0^\circ$  plane wave incidence)

a resistively loaded dipole with a high impedance source resistance were investigated by K. P. Esselle and S. S. Stuchly [19] using a *FD-TD* based code. The high frequency limit decreases for a  $45^\circ$  incident plane wave on a 100% Wu-King dipole (Figures 5.47, 5.48). The voltage peak lags more than for plane wave incidence.

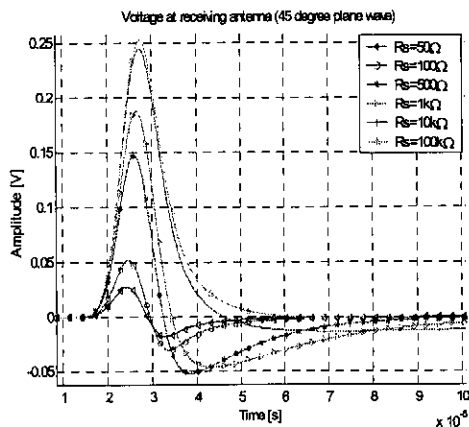


Figure 5.47 : Voltage transient at source for 100% Wu-King dipole ( $45^\circ$  plane wave incidence)

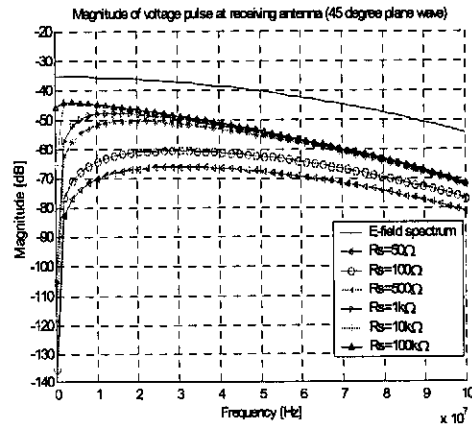


Figure 5.48 : Frequency spectrum of voltage transient at source for 100% Wu-King dipole ( $45^\circ$  plane wave incidence)

Results for a 50% Wu-King loading with a  $45^\circ$  degree incident plane wave and 25% Wu-King loading are given in *Appendix D1*.

## 5.4 Asymmetric dipole antenna

The asymmetric resistive antenna proved to be useful for incorporating the transmit and receive electronics in the conducting arm. Simulations in air (Section 5.4.1) and in the mine environment (Section 5.4.2) show that the antenna displays a resonance frequency and asymmetry in the far-field pattern. The antenna is electrically small and the asymmetry does not cause extensive degradation of the radiated pulse (Section 5.4.3) at different theta angles. Higher receive sensitivity is achieved than with the symmetrically loaded antenna (Section 5.4.3).

### 5.4.1 Asymmetric resistively loaded dipole in air

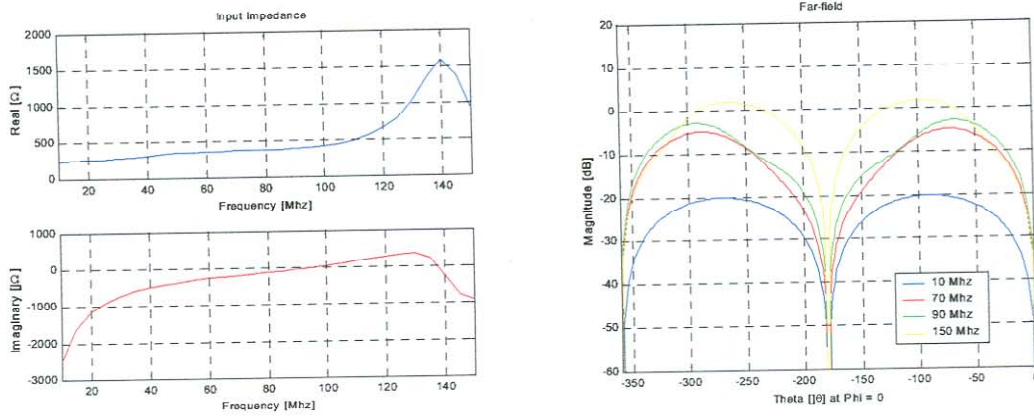


Figure 5.49 : Input impedance of asymmetric dipole      Figure 5.50 : Far-field gain of asymmetric dipole

The asymmetric dipole considered here consists of a 1m conducting arm and a 1m resistive (100% Wu-King) arm. This configuration was introduced by D. M. Claassen [3] and is currently in use as a radar probe. The conducting arm houses the electronics and batteries of the radar and it is thus not practical to implement any resistive loading on this arm.

The antenna resonates at 100 MHz. The resonance in the frequency band of interest is not desirable because it will add ringing. The resistive arm of Claassen's design was shortened to shift the resonance above 100 MHz. The input reactance (Figure 5.49) as expected is still capacitive at the low frequencies. The radiation pattern (Figure 5.50) shows that the gain is higher, compared to the 100% Wu-King dipole. The antenna's resistive arm contributes to the reduction in efficiency but is not as severe as when both arms are loaded.

At 10 MHz the antenna is electrically short and the radiation pattern is symmetrical, but for frequencies of 70 and 90 MHz the pattern squints towards the conducting arm, as the resistive arm starts to support a travelling wave. The antenna can be compared to a single travelling wave element (*Chapter 3*).

The resistive arm partially absorbs the end reflection at these frequencies and the main sources of radiation are at the source and at the conducting arm's open end. At 150 MHz, the pattern squints towards the ground arm. A reason for the squint reversal may be that the 150 MHz component does not travel far up the resistive arm before being absorbed and the end reflection of the ground arm therefore dominates. The radiation pattern seems to be dominated by the ground arm in the desired frequency band and the antenna only starts to support the travelling wave behaviour above 100 MHz.

#### 5.4.2 Insulated asymmetric dipole in a mine environment

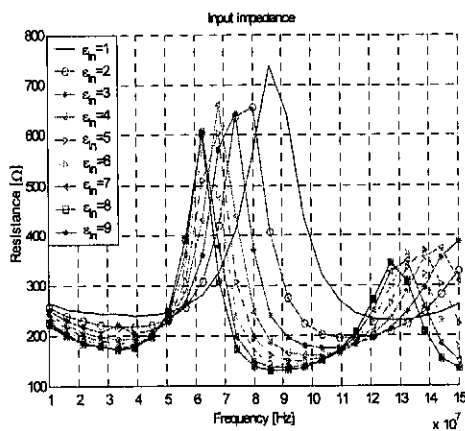


Figure 5.51 : Input resistance of centre insulated asymmetric dipole ( $\epsilon_{in} = 1-9$ ,  $\sigma_{in} = 0$ ,  $\epsilon_{out} = 7$ ,  $\sigma_{out} = 0$ )

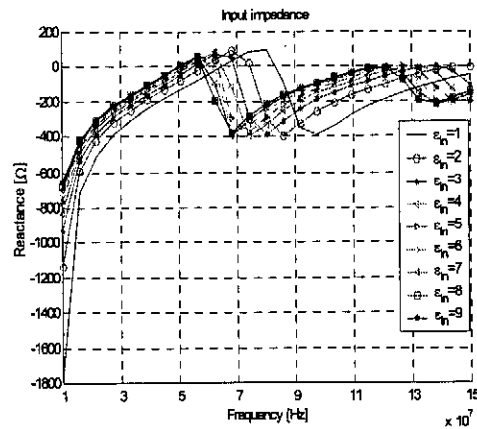


Figure 5.52 : Input reactance of centre insulated asymmetric dipole ( $\epsilon_{in} = 1-9$ ,  $\sigma_{in} = 0$ ,  $\epsilon_{out} = 7$ ,  $\sigma_{out} = 0$ )

Figures 5.51 and 5.52 show the input impedance variation over frequency for different insulation dielectric constants, as was done in Section 5.2.2. The resonance frequency remains above 50 MHz while the resistance is higher than for the conducting dipole at frequencies below the first

resonance, due to the resistive arm. The impedance, however, is unstable over the frequency spectrum and maximum power transfer will not be possible.

Appendix D2 presents the input impedance for different ambient electrical properties for polyurethane insulation. Figures 5.53-5.55 represent the far-field gain over frequency of the asymmetric dipole at  $\theta = 44^\circ$ ,  $90^\circ$  and  $134^\circ$  for the previous conditions where the impedance is given by Figures 5.51 and 5.62. The antenna displays an asymmetric radiation pattern at different  $\theta$  angles, as expected from the results obtained in the previous section where the antenna is situated in air.

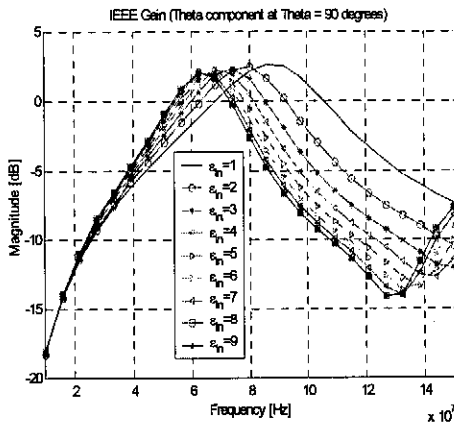


Figure 5.53 : Far-field gain of asymmetric dipole (Theta component at  $\theta = 0^\circ$ )

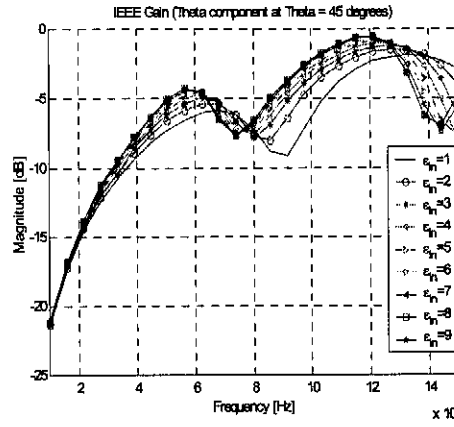


Figure 5.54 : Far-field gain of asymmetric dipole (Theta component at  $\theta = 44^\circ$ )

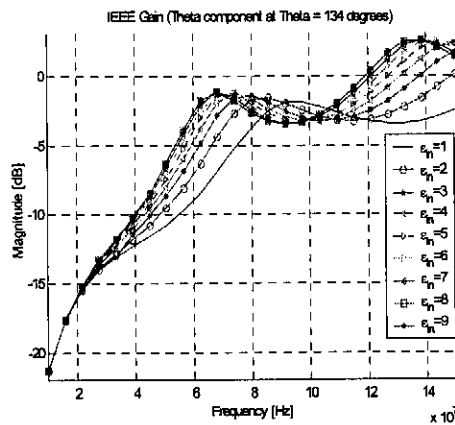


Figure 5.55 : Far-field gain of asymmetric dipole (Theta component at  $\theta = 134^\circ$ )

The broadside gain gradually increases over frequency and peaks at the anti-resonance frequency. Below 60 MHz, the beam squints towards the resistive arm and bends over towards the ground arm between 60 and 80 MHz. For higher insulation permittivities the radiation pattern decreases at  $\theta = 44^\circ$  for frequencies above 140 MHz and peaks again for  $\theta = 134^\circ$ . This behaviour is attributed to a stronger multiple beam in the  $\theta = 134^\circ$ , because the broadside gain has a minimum.

### 5.4.3 Pulse-transmitting characteristics of the asymmetric dipole

This section includes results for time-dependent electric field traces at 10m in air for  $\theta = 45^\circ$ ,  $90^\circ$  and  $135^\circ$ . Different percentage resistor values for the Wu-King were used, with the antenna excited by a voltage source ( $R_s = 1 \Omega$ ) with the same frequency content as in sections 5.3.3.

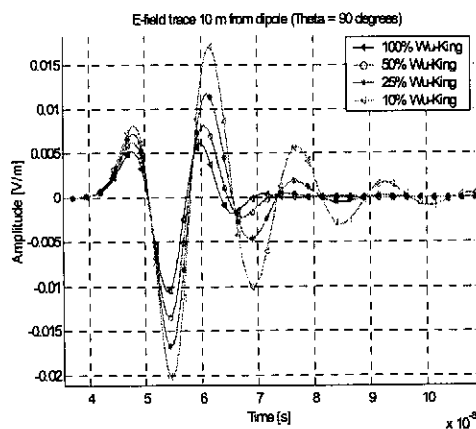


Figure 5.56 : Broadside trace of electric field for different percentage Wu-King loadings for the asymmetric dipole ( $\theta = 0^\circ$ )

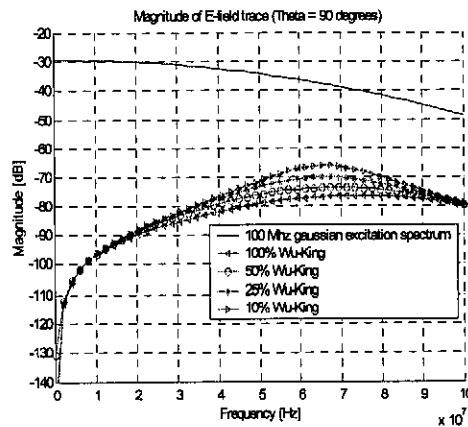


Figure 5.57 : Magnitude of the broadside electric field for different percentage Wu-King loadings for the asymmetric dipole ( $\theta = 0^\circ$ )

From the far-field pattern (Figure 5.50) it is clear that the beam is dominantly squinted towards the resistive arm in the frequency band 10-100 MHz. The broadside (Figures 5.56, 5.57) trace do not display the same natural frequency for different percentage Wu-King loadings as seen for the symmetrically-loaded Wu-King antenna. The maximum for the electric field time trace is slightly higher, and the 100% Wu-King loading displays a dominant peak in the time trace that was not present for the symmetrically loaded antenna with the same loading. The electric field is slightly higher for  $\theta = 45^\circ$  than for  $\theta = 135^\circ$  (Figures 5.58-5.61).

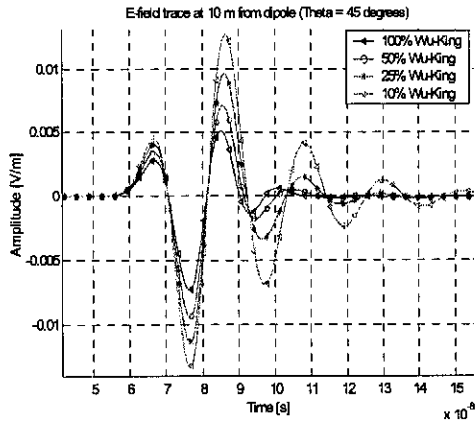


Figure 5.58 : Broadside trace of electric field for different percentage Wu-King loadings for the asymmetric dipole ( $\theta = 45^\circ$ )

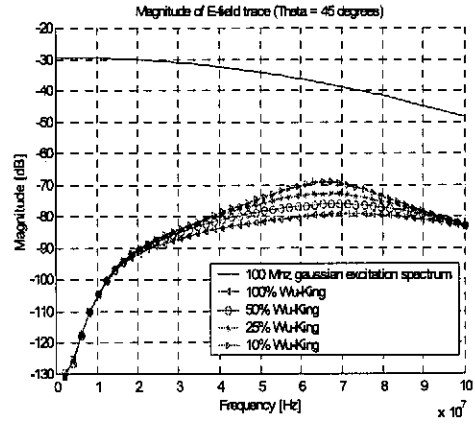


Figure 5.59 : Magnitude of the broadside electric field for different percentage Wu-King loadings for the asymmetric dipole ( $\theta = 45^\circ$ )

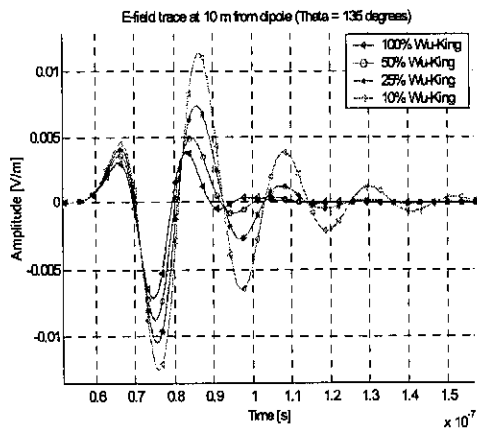


Figure 5.60 : Broadside trace of electric field for different percentage Wu-King loadings for the asymmetric dipole ( $\theta = 135^\circ$ )

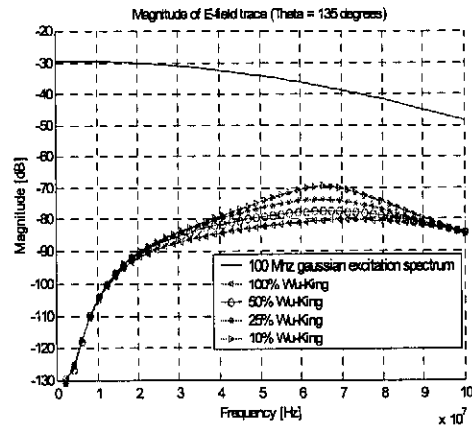


Figure 5.61 : Magnitude of the broadside electric field for different percentage Wu-King loadings for the asymmetric dipole ( $\theta = 135^\circ$ )

### 5.4.4 Pulse-receiving characteristics of asymmetric dipole

One addition to the previous investigations is a  $-45^\circ$  plane wave off-broadside to investigate the difference, if any, in the reception properties of the antenna due to the asymmetry in the far-field (refer to section 5.3.4 and 5.4.4 for the simulation specifics and geometrical setup).

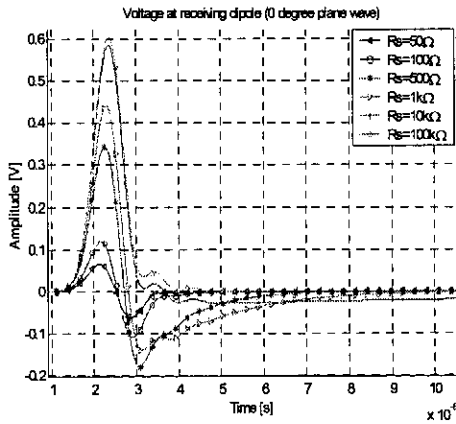


Figure 5.62 : Voltage transient at source for 100% Wu-King asymmetric antenna ( 0° plane wave incidence )

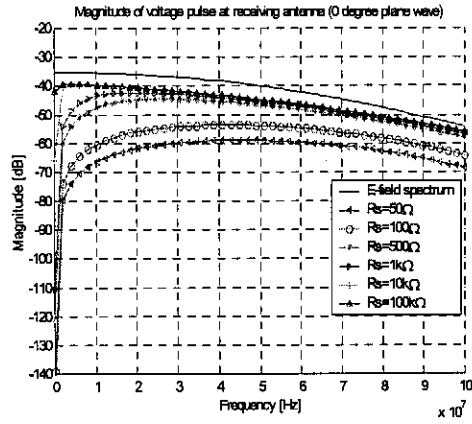


Figure 5.63 : Frequency spectrum of voltage transient at source for 100% Wu-King asymmetric dipole ( 0° plane wave incidence )

The asymmetric antenna has a surprisingly flat frequency (Figure 5.63) response to 0° plane waves, with adequate damping shown in the time trace of the voltage (Figure 5.62). The antenna has better low frequency sensitivity than the conducting dipole and better high frequency performance than the symmetrically loaded antenna for high source resistances (10-100 kΩ).

The peak does not deviate as much as for the symmetrical loaded dipole, which can be attributed

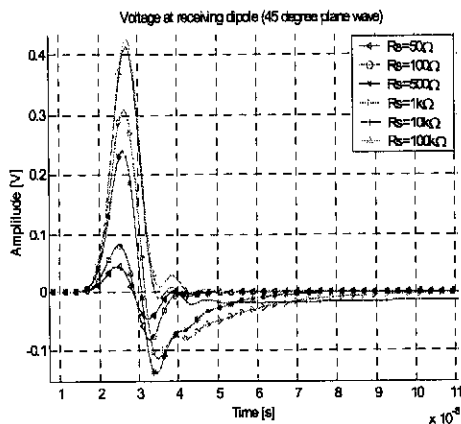


Figure 5.64 : Voltage transient at source for 100% Wu-King asymmetric antenna. ( 45° plane wave incidence )

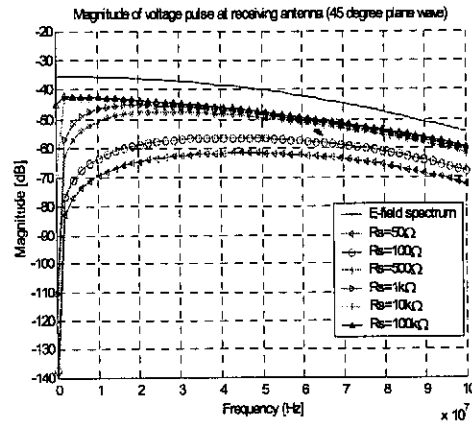


Figure 5.65 : Frequency spectrum of voltage transient at source for 100% Wu-King asymmetric dipole. ( 45° plane wave incidence )

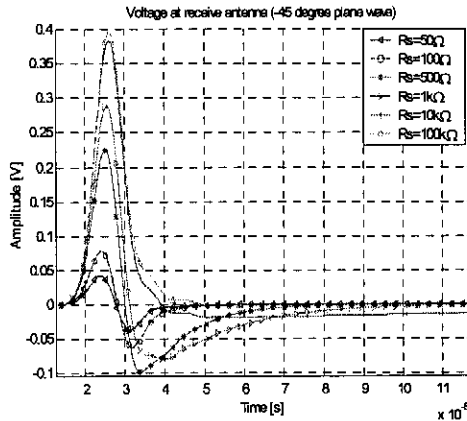


Figure 5.66 : Voltage transient at source for 100% Wu-King asymmetric antenna (  $-45^\circ$  plane wave incidence )

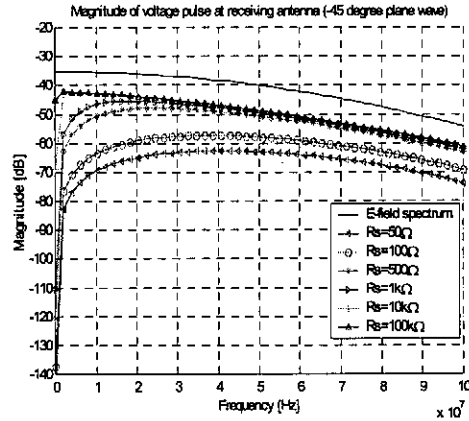


Figure 5.67 : Frequency spectrum of voltage transient at source for 100% Wu-King asymmetric dipole (  $-45^\circ$  plane wave incidence )

to its better high frequency reception or different time constants associated with a lower input resistance above the symmetrical loaded dipole. There is a total reduction in the frequency spectrum for a  $45^\circ$  plane wave (Figures 5.64, 5.65) and the main peak deviates more. An unexplained ripple is visible in the voltage traces for a  $0^\circ$  and  $45^\circ$  plane wave but smoothes out for a  $-45^\circ$  plane wave (Figures 5.66, 5.67). The ripple may represent late time ringing on the conductive arm. Results for a 50% Wu-King loaded antenna with a  $\pm 45^\circ$  degree incident plane wave and 25% Wu-King loading is given in *Appendix D3*.

## 5.5 Coupling between aligned transmitter and receiver

The coupling of a Gaussian input pulse (frequency spectrum of 0-100 MHz) was simulated for four different configurations (Figure 5.68) of transmitter and receiver units in a borehole. The current radar system represents the alignment shown by Figure 5.68 (b). The time domain coupling will yield a better understanding of the physical magnitude of a real voltage signal at the receiver. This may illustrate whether the receiver electronics can be damaged or saturated if the transmitter is more closely situated. The simulations were performed firstly for a dipole transmit and receive antenna with the same dimensions as in Section 5.2 and, secondly, for an asymmetric dipole with a continuous 100% Wu-King loading, as used in Section 5.4. The antennas were

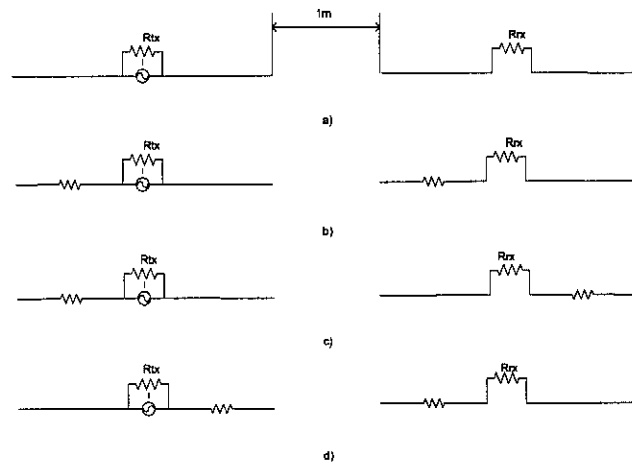


Figure 5.68 : Different aligned transmitter and receiver orientations in a borehole

situated in air with a source resistance of  $R_{tx} = 1\Omega$  and were 1m apart. It was believed that the resistively loaded arms facing each other would cause less coupling due to the absorbing resistance. Figures 5.69-5.72 show that the coupling is the highest for two dipoles, and when the conducting arms face each other for the asymmetric antenna.

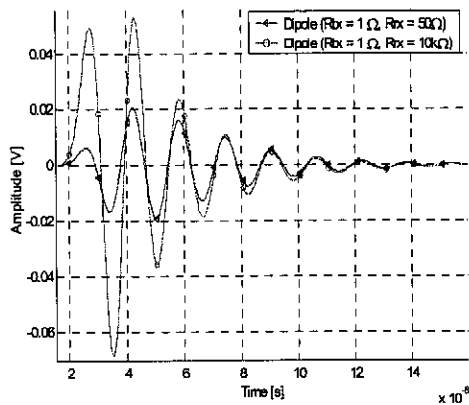


Figure 5.69 : Voltage at receiver for setup shown in Figure 5.68 (a)

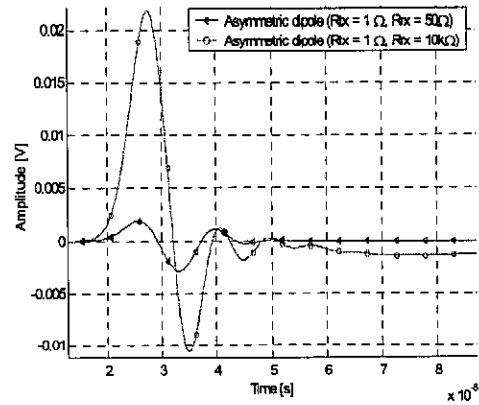


Figure 5.70 : Voltage at receiver for setup shown in Figure 5.68 (b)

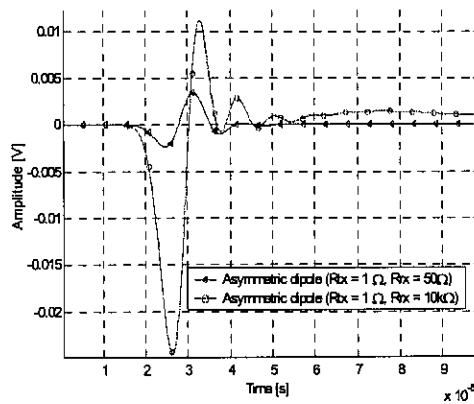


Figure 5.71 : Voltage at receiver for setup shown in Figure 5.68 (c)

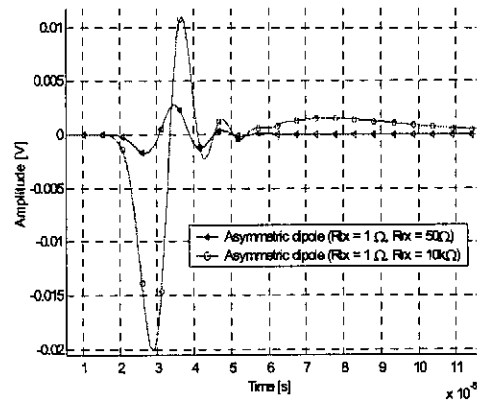


Figure 5.72 : Voltage at receiver for setup shown in Figure 5.68 (a)

There, however is no severe reduction in coupling for the configurations of Figure 5.67 (b) and (d). The voltage coupling is higher for a high source resistance as seen from the pulse-receiving characteristics of the asymmetrical antenna in Section 5.4.4. If a high impedance receiver is used, the front-end electronics may need some protection from the direct pulse.

## 5.6 Conclusion

As expected the narrow bandwidth of a conducting dipole is inadequate for pulsed radar applications. The symmetric resistively loaded antenna reduced the ringing on the antenna at the cost of efficiency. The length chosen for all the antennas simulated is shown them to be too short to ensure full power transfer over the band for the specific frequency band.

The asymmetric resistively loaded antenna caused asymmetry in the radiation pattern, but seems to be the most practical solution due to the housing of the electronics. The resistively loaded antennas showed an improvement in transient receiving sensitivity when terminated with a high impedance. In essence, a pulse radar system should be designed for a flat transfer when the transfer functions of the transmit and receive electronics is unknown. Electrically small wire antennas provide little variation in their radiation pattern for different theta values.